ABSTRACT

Title of Dissertation: EXPERIMENTAL STUDY OF LONGITUDINAL
                             ENERGY SPREAD IN SPACE-CHARGE-
                             DOMINATED BEAMS

                             Yupeng Cui, Doctor of Philosophy, 2004

Dissertation Directed By: Professor Patrick O'Shea
                             Professor Emeritus Martin Reiser
                             Dr. Yun Zou
                             Department of Electrical and Computer Engineering

A compact high-resolution variable-focusing retarding field energy analyzer has been developed to measure the energy spread of space-charge-dominated electron beams. A cylindrical focusing electrode is used to overcome the beam expansion inside the device due to space-charge forces, beam emittance, etc. The focusing voltage is independently adjustable to provide proper focusing strength. Single particle simulation and theoretical error analysis using beam envelopes show that this energy analyzer can get very high resolution for low-energy beams, which was found to be in good agreement with experimental results. The measured beam energy spectrum is both temporally and spatially resolved. In addition, a computer-controlled automatic system is developed to provide real-time data acquisition and processing. The measurements of the beam energy spread are compared with the theoretical predictions.

It is believed that coupling between the transverse and longitudinal directions via Coulomb collisions will cause an increase of the beam longitudinal energy spread. At the University of Maryland, experiments have been carried out to study the energy evolution in such intense beams with a high-resolution retarding field energy analyzer. The temporal beam energy profile along the beam pulse has been characterized at the distance of 25 cm from the anode of a gridded thermionic electron gun. The mean energy of the pulsed beams including the head and tail is reported here. The measured rms energy spread is in good agreement with the predictions of the intrabeam scattering theory.

In order to study the scaling of the beam energy spread, a two-meter long linear solenoid focusing system has been set up and beam energy spread is measured after the beam passes through the long transport line. Again, the beam energy spread is measured under different beam conditions (energy, current, and density). The experimental results here are in remarkable agreement with the lower limit of the beam energy spread set by the intra beam scattering theory at the lower beam current density. Under some controlled conditions, energy spread larger than the predictions of the intra beam scattering theory are also observed.

EXPERIMENTAL STUDY OF LONGITUDINAL ENERGY SPREAD IN SPACE-CHARGE-DOMINATED BEAMS

By

Yupeng Cui

Dissertation submitted to the Faculty of the Graduate School of the
University of Maryland, College Park, in partial fulfillment
of the requirements for the degree of
Doctor of Philosophy
2004

Advisory Committee:
        Professor Patrick O'Shea, Chair / Advisor
        Professor Emeritus Martin Reiser / Co-Advisor
        Professor Gottlieb Oehrlein
        Professor Jon Orloff
        Professor Wesley Lawson
        Doctor   Yun Zou

Dedication

To my parents

Acknowledgements

My advisor, Professor Packick O'Shea, guided me to achieve the success on my dissertation. I would express my appreciation to him for his professional advice and guidance whenever I had any problems. His enthusiasm and encouragement have greatly motivated me to finish my Ph.D work. I also thank his generosity for providing funding support for my research. I would like to express my thanks to Professor Martin Reiser for the theoretical guidance and discussions. His deep insight and experience in beam physics always told me the right directions to go. I would like to thank Dr. Yun Zou, Research Scientist in the UMER lab, for his tremendous helps in both theoretical and experimental parts of my dissertation. I am grateful to Dr. Rami Kishek, the manager of the UMER project, Dr. Irving Haber, Visiting Scientist in the UMER project, for their help on my simulation work. I am thankful to Dr. Santiago Bernal for his valuable suggestions in my experiments. I am also thankful to Victor Yun, the former mechanical engineer, and Mark Walter for their mechanical support. I am thankful to Mr. Bryan Quinn, the electrical engineer in the UMER lab, for his valuable suggestions and support on electrical problems.

I would also like to thank Dr. David Kehne, former graduate student in our lab, Dr. Terry Godlove for their helpful advice, and my colleagues Hui Li, Jon Newman, and John Harris for valuable discussion. My Ph.D dissertation work would not have been successful without the contributions from many other people not mentioned by name here.

I am also grateful to Prof. Gottlieb Oehrlein, Prof. Jon Orloff, and Prof. Wesley Lawson for serving on the advisory committee.

Table of Contents

List of Tables

List of Figures

Chapter 1 : Introduction

1.1 Historical background and motivation

The application and development of charged particle devices can be traced back to the 1920's, when charged particle dynamics, especially in the field of electron optics, experienced a fast development stimulated by strong industrial needs, such as electron microscopes, cathode ray tubes and television, military requirements, such as radar microwave source, and high energy accelerators [1]. In recent years, the demand for high quality intense beams with applications for heavy-ion fusion (HIF) [2], high-current linacs and free electron lasers [3], etc., research on high intensity beam became an important and urgent task. The physics in space-charge-dominated beams is relatively new and much more complex than in low intensity beams since the particle distribution influences the net focusing force on the particles and may lead to nonlinear collective effects that are observed in low-intensity beams. At the University of Maryland, theoretical and experimental studies on transverse and longitudinal beam dynamics have been carried out for over two decades to study space-charge-dominated beams [1,4]. Many graduate students have conducted pioneering research work, such as the beam merging experiments of five beamlets [5], beam longitudinal dynamics in parabolic and rectangular beam bunches [6], longitudinal space-charge waves and resistive-wall instability in space-charge-dominated electron beams [7,8]. Even though significant progress has been made in

1

the past years, many interesting topics still require new experimental and theoretical research. The evolution of the longitudinal energy spread is one example.

Understanding the physics of the beam energy spread in high-quality intense beams is very important in the applications of advanced particle accelerators for heavy-ion inertial fusion, high-energy colliders, and free-electron lasers. If the energy spread or the longitudinal temperature of the beam is too large, the chromatic aberrations in the beam optics will degrade the beam quality and cause difficulty in beam handling and focusing on the target. One of the mechanisms causing growth of energy spread is the energy transfer from the transverse direction into the longitudinal direction via Coulomb collisions or collective space-charge effects. This happens in a system with temperature anisotropy, such as a beam accelerated in the longitudinal direction. In such a system, the longitudinal temperature of the beam is decreased during acceleration, while the temperature in the transverse direction is kept roughly the same as in the cathode. Multiple Coulomb collisions and instabilities will try to equilibrate this anisotropic state, causing an increase in the longitudinal beam energy spread or temperature. Many theoretical studies have been made on the description of this energy equipartitioning due to small angle Coulomb collisions [1,9,10]. Recent simulation results also show that, under certain conditions, instabilities might develop to expedite this energy equipartitioning due to collective space-charge effects [11]. However, there are so far only a few experimental measurements of this energy-equipartitioning process [12,13,14].

The first experimental observation of enhanced energy spread in a low current electron beam (beam current is on the order of μA) was reported by Boersch in 1954

[12] and since then this phenomenon has been known as the Boersch effect. This energy spread broadening is believed to be due to Coulomb collisions happening at the beam waist. Hyatt, in 1987, reported an experimental measurement of the anisotropic temperature relaxation in a stationary, magnetically confined electron plasma, where he found good agreement between the experimental results and the small-momentum-transfer collision theory [13]. But so far there was no direct experiment on studying the temperature equipartitioning process in a space-charge-dominated electron beam.

The energy equipartitioning due to the Coulomb collisions is a relatively long relaxation process. The energy transfer from the transverse direction into the longitudinal direction via intra-beam scattering is a slow process, with a relaxation time usually much longer than the lifetime of a beam in a linear accelerator, for instance. However, even though it takes a long time to reach equipartitioning, the growth of energy spread is very steep in the beginning near the electron gun or ion source. With the aid of the high-resolution energy analyzer, this growth of energy spread is measurable even within a relatively short distance. In this dissertation, we report experiments conducted at the University of Maryland Electron Ring (UMER) lab [4] to study the energy spread evolution in a space-charge-dominated electron beam. The experimental results are in very good agreement with the theoretical lower limit imposed by Coulomb scattering from the transverse to the longitudinal direction (Boersch effect) and the longitudinal-longitudinal Coulomb interaction in an accelerated beam.

1.2 Basic Beam Terminologies and Parameters

1.2.1 K-V (Kapchinsky-Vladimirsky) Distribution

The K-V model is a very important tool to study the space-charge effects on the transverse beam dynamics. It has been widely used in accelerator theory and design since published in 1959. In this model, the space-charge force is linear and the beam phase space area remains constant. For the forces to be linear in the transverse direction, the condition for paraxial motion must be satisfied and the changes in the beam size must occur slowly so that the longitudinal forces are negligible.

Under this condition, the beam envelope in an axisymmetric focusing transport channel is described by the equation

$$R'' + \kappa_0 R - \frac{K}{R} - \frac{\varepsilon^2}{R^3} = 0 \ , \qquad (1.1)$$

where R is beam radius, z is the axial distance, ε the transverse emittance. K is the generalized beam perveance defined by

$$K = \frac{I}{I_0} \frac{2}{(\beta\gamma)^3} \ . \qquad (1.2)$$

Here, β and γ are the relativistic velocity and energy factors, respectively. I is the beam current and I_0 is the characteristic current given by the relation

$$I_0 = \frac{4\pi\varepsilon_0 mc^3}{q} \ , \qquad (1.3)$$

where q is the particle charge, m is the particle mass and c is the speed of light. For electron beams, I_0 is about 17 KA.

In Equation (1.1), κ_0 is the external focusing strength defined by

$$\kappa_0 = \left(\frac{qB_z(z)}{2mc\beta\gamma}\right)^2. \tag{1.4}$$

$B_z(z)$ is the axial magnetic field.

The envelope of charged particle beams tends to increase because of space-charge effect by $\dfrac{K}{R}$ and the emittance effect by $\dfrac{\varepsilon^2}{R^3}$. If the condition $\dfrac{K}{R} > \dfrac{\varepsilon^2}{R^3}$ is satisfied, the beam is transversely space-charge-dominated. By contrast, if the condition $\dfrac{K}{R} < \dfrac{\varepsilon^2}{R^3}$ is satisfied, the beam is emittance dominated.

1.2.2 Definition of Beam Energy Spread

In a beam with equilibrium state, the particle velocity in the longitudinal direction follows the standard Maxwellian distribution, which is given by

$$f(v) = f_0 \exp\left(-\frac{m(v-v_0)^2}{2k_B T_{//}}\right). \tag{1.5}$$

Here, k_B is the Boltzmann's constant and $T_{//}$ is the beam longitudinal temperature. v_0 is the beam velocity given by

$$v_0 = \sqrt{\frac{2E_0}{m}}. \tag{1.6}$$

Given the velocity distribution, the particle energy distribution can be calculated from the following relation:

$$f(v)dv = f(E)dE, \tag{1.7}$$

where $E = \dfrac{1}{2}mv^2$ is the beam energy.

From Equation (1.7), we have

$$f(E) = \frac{f(v)}{mv}. \tag{1.8}$$

Substitute Equation (1.5) and (1.6) into Equation (1.8), we have

$$f(E) = \frac{1}{\sqrt{2mE}} f_0 \exp\left(-\frac{m\left(\sqrt{\frac{2E}{m}} - \sqrt{\frac{2E_0}{m}}\right)^2}{2k_B T_{//}}\right) \tag{1.9}$$

$$= \frac{1}{\sqrt{2mE}} f_0 \exp\left(-\frac{\left(\sqrt{E} - \sqrt{E_0}\right)^2}{k_B T_{//}}\right)$$

Set $E = E_0 + x$, where x is a small difference between the particle energy E and the

beam mean energy E_0. Applying Taylor expansion $\sqrt{1+x} \doteq 1 + \frac{1}{2}x$, we have

$$\sqrt{E} - \sqrt{E_0} = \sqrt{E_0 + x} - \sqrt{E_0}$$

$$\approx \sqrt{E_0}\left(1 + \frac{x}{2E_0}\right) - \sqrt{E_0} = \frac{x}{2\sqrt{E_0}} \tag{1.10}$$

According to Equation (1.9), the particle energy density distribution is given by

$$f(E) = \frac{1}{\sqrt{2m(E_0 + x)}} f_0 \exp\left(-\frac{x^2}{4k_B T_{//} E_0}\right). \tag{1.11}$$

When x satisfies $x \ll E_0$, then

$$f(E) = \frac{1}{\sqrt{2mE_0}} f_0 \exp\left(-\frac{(E - E_0)^2}{4k_B T_{//} E_0}\right)$$

$$= \frac{1}{\sqrt{2mE_0}} f_0 \exp\left(-\frac{(E - E_0)^2}{2\Delta E^2}\right) \tag{1.12}$$

Here the rms energy spread is $\Delta E = \sqrt{2k_B T E_0}$.

From Equation (1.12), the beam energy spectrum is a Gaussian distribution for the beams with Maxwellian velocity distribution when the rms energy spread is much less than the beam energy. In this dissertation, we are trying to measure the longitudinal beam energy spread defined here and its evolution in space-charge-dominated beams.

1.3 Organization of the Dissertation

This dissertation consists of three parts. The first part presents the theories of the longitudinal energy spread evolution. Chapter 2 describes the mechanism of the energy spread evolution including the Boersch effect and the longitudinal-longitudinal relaxation. Based on the intrabeam scattering theory, a scaling law estimating the beam energy spread is derived.

In the second part of this dissertation, the development of a novel high-resolution retarding energy analyzer is presented. Chapter 3 describes the design of the analyzer and simulation of particle trajectories. Single particle simulation and beam envelope analysis in the analyzer are presented in this Chapter. Chapter 4 presents the beam test of the analyzer. A fast high-resolution automatic measurement system has been set up, which significantly improves the experimental efficiency. The energy spread of electron beams emitted from an electron gun is measured at different beam energies and the results are compared with the theoretical predictions.

Chapter 5 is the third part of this dissertation describing the design, facility setup and experimental results of a long solenoid transport line with a length of 2.3 m. Experimental results of the beam energy spread after a 2.3 m uniform focusing channel are also compared with the theoretical prediction and scaling law.

Chapter 2 : Source of the Longitudinal Energy Spread in Electron Beams

2.1 Introduction

There are many sources contributing to the longitudinal energy spread in an electron beam emitted from a thermionic cathode. The two dominant sources for the energy spread are the Boersch effect [12] and the longitudinal-longitudinal relaxation effect [15]. The Boersch effect is due to the energy transfer from the transverse direction to the longitudinal direction. The longitudinal-longitudinal effect is due to the fast beam acceleration in the electron gun and therefore the energy transfer from the potential energy to the thermal kinetic energy in several plasma periods.

Three main physical processes are involved as the beam accelerates from the cathode to the measurement position: cooling due to acceleration, longitudinal-longitudinal effects, and the Boersch effect.

2.2 Beam Cooling

The electron distribution in a thermionic emitter is in thermal equilibrium (i.e. the transverse and longitudinal temperatures are equal). The rms beam energy spread due to the cathode temperature is given by

$$\Delta E_{rms} = mv^2_{rms} = k_B T = k_B T_{//i} = k_B T_{\perp i}. \qquad (2.1)$$

Here, v_{rms} is the rms thermal velociy, k_B is the Boltzmann's constant, and $T_{//i}$ and $T_{\perp i}$ are the beam longitudinal and transverse temperature, respectively. For a typical

gun with cathode temperature of 1100° C, the corresponding thermal energy is around 0.1eV. This implies that the energy spread in the transverse direction is the same as that in the longitudinal direction.

When the particles with the energy spread of $k_B T$ are accelerated by the accelerating voltage V_0, every particle gains the same longitudinal kinetic energy. The energy spread of the particles remains constant $k_B T$. However, the longitudinal velocity spread is decreased and hence the longitudinal temperature decreases. Equation (2.2) describes the relation between the initial longitudinal temperature, $T_{//i}$, and the longitudinal temperature immediately after acceleration, $T_{//f}$ [1].

$$k_B T_{\|f} = \frac{(k_B T_{\|i})^2}{2qV_0}.$$
(2.2)

For instance, a beam that comes off the thermionic cathode with a temperature of 0.1eV is accelerated by a 5 kV voltage can be cooled to a temperature of 10^{-6} eV in the longitudinal direction. This is known as the longitudinal cooling effect due to the fast acceleration.

2.3 Beam Relaxation

Note that the transverse temperature is the same as the initial temperature since the acceleration acts only in the longitudinal direction. The longitudinal temperature becomes negligible compared to the transverse temperature. The beam is now in an extremely anisotropic state $(T_{//i} \ll T_{\perp i})$. Coulomb collisions or other effects of a random nature, such as instabilities, will try to redistribute the beam velocity distribution into thermal equilibrium. The resulting beam longitudinal energy spread

will increase while the transverse temperature decreases. This thermal relaxation procedure is referred to as the Boersch Effect [1,12].

The transverse-longitudinal thermal relaxation effect is very complicated in a real beam. A theoretical description of collisional velocity scattering has been the subject of continuing effort over the past 60 years. Small-momentum-transfer collisions are thought to be dominant, a view which has led to a Fokker-Planck approximation to the velocity-scattering process [13]. Fokker-Planck theories of collisional velocity-space transport have been obtained by many people in both the nonmagnetized and magnetized regimes. Ichimaru and Rosenbluth (IR) calculate the rate of isotropic temperature and relaxation in a weakly magnetized electron beam for which the Larmor radius r_L is much larger than the Debye shielding length λ_D [9]. For a simple case in which the beam propagates through a smooth focusing channel and has a constant radius, the temperature relaxation can be described by the following equations [1]

$$\frac{dT_\perp}{dt} = -\frac{T_\perp - T_{//}}{\tau},$$ (2.3)

$$\frac{dT_{//}}{dt} = 2\frac{T_\perp - T_{//}}{\tau}.$$ (2.4)

In the differential equations, $T_{//}$ changes twice as fast as $T_\perp$. The relaxation time τ is given by the relation [1]

$$\frac{1}{\tau} = \frac{8\pi^{1/2}nq^4}{15(4\pi\varepsilon_0)^2 m^{1/2}(k_B T_{eff})^{3/2}}\ln\Lambda,$$ (2.5)

where n is the particle density and $\ln\Lambda$ is the Coulomb logarithm defined from [1] by

$$\ln \Lambda = \ln \left(5.66 \times 10^{21} \frac{\left(k_B T / mc^2 \right)^{3/2}}{n^{1/2}} \right), \text{ (2.6)}$$

which varies very slowly over a wide range of parameters involved. For electrons, $\ln \Lambda$ is between 6 and 30 for densities between 10^3 and 10^{24} m^{-3} and temperatures between 10^2 and 10^8 K. The particle density n is given by

$$n = \frac{I}{qa^2 \pi v}, \qquad\qquad (2.7)$$

where I is the beam current, a is the beam radius and v is the beam velocity. The above expressions are valid as long as the beam radius is much larger than the Debye length. For a 5 keV 135 mA beam with the beam radius of 8 mm and an initial temperature of ~0.1 eV, the Debye length is about 0.1 mm, which is much less than the beam radius. The effective temperature T_{eff} is obtained from the integral [1]

$$\frac{1}{T_{eff}^{3/2}} = \frac{15}{4} \int_{-1}^{1} \frac{\mu^2 (1 - \mu^2) d\mu}{\left[\left(1 - \mu^2 \right) T_\perp + \mu^2 T_\| \right]^{3/2}}. \quad (2.8)$$

Assuming initial temperatures of $T_{//0} = 0$ and $T_{\perp 0} \neq 0$ for an accelerated beam, the initial effective temperature from (2.8) is [1]

$$\frac{1}{T_{eff,0}^{3/2}} = \frac{15\pi}{8 T_{\perp 0}^{3/2}}. \qquad\qquad (2.9)$$

The initial relaxation time from (2.5) and (2.9) is

$$\frac{1}{\tau_0} = \frac{\pi^{3/2} n r_c^2 c}{(k_B T_{\perp 0} / mc^2)^{3/2}} \ln \Lambda, \qquad (2.10)$$

where r_c is the classical particle radius defined by $r_c = q^2 / \left(4\pi\varepsilon_0 mc^2 \right)$ and c is light speed.

When equilibrium is reached, the effective temperature $T_{eff,eq}$ from Equation (2.8) is the same as the equilibrium temperature T_{eq} (i.e., $T_{eff,eq} = T_{eq} = T_{\perp} = T_{//}$). If the total thermal energy in the beam is constant and given by $T_{\perp 0}$, the final equilibrium temperature is $T_{eq} = \frac{2}{3}T_{\perp 0}$ due to the zero initial longitudinal temperature.

With the above initial and final conditions, the relations of temperatures versus time are obtained from the differential equations (2.3-2.4) and are plotted in Figure 2.1. The relaxation time τ in the differential equations is increasing with time. The longitudinal and transverse temperatures are expressed in units of the equilibrium temperature and the time is in units of the relaxation time $\tau_{eq} = 3.2\tau_0$ at equilibrium. The two curves that describe the time evolution of the transverse and longitudinal temperatures can be approximated by exponential functions as [1]

$$T_{\perp} = \frac{2}{3}T_{\perp 0}\left(1 + \frac{1}{2}e^{-3t/\tau_{eff}}\right), \qquad (2.11)$$

$$T_{//} = \frac{2}{3}T_{\perp 0}\left(1 - e^{-3t/\tau_{eff}}\right), \qquad (2.12)$$

where the best fit is obtained when the effective relaxation time τ_{eff} is equal to $1.34\,\tau_0$. From equation (2.10), we can obtain for electrons

$$\frac{1}{\tau_{eff}} = \frac{1}{1.34\tau_0} = \frac{\pi^{3/2}nr_c^2 c}{1.34\left(k_B T_{\perp 0}/mc^2\right)^{3/2}}\ln\Lambda \qquad (2.13)$$
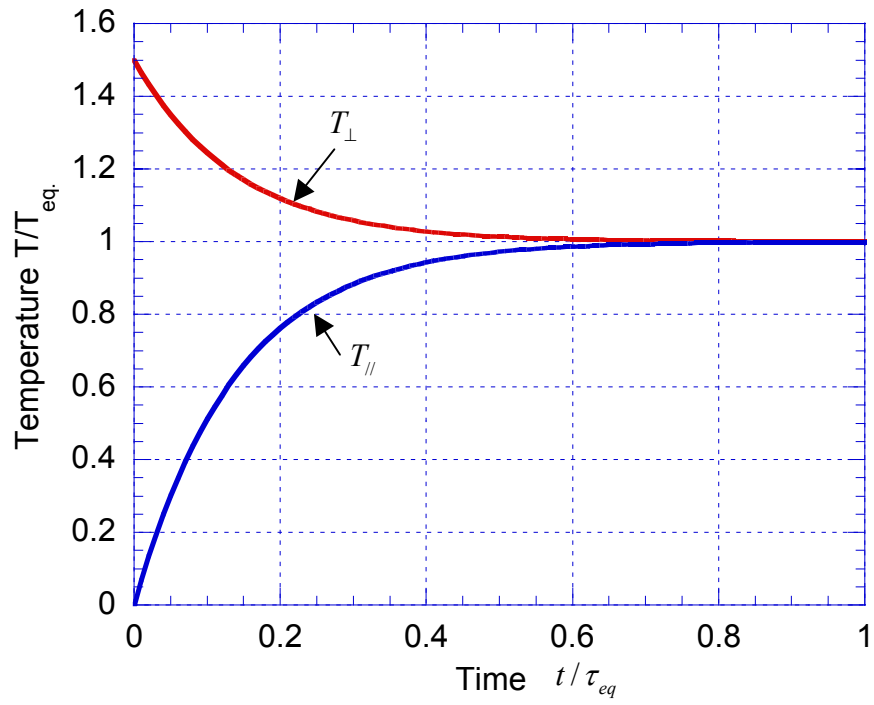
Figure 2.1. Relaxation of transverse and longitudinal beam temperatures in a uniform focusing channel.

The energy transfer from transverse direction to longitudinal direction due to the Boersch effect can be suppressed by applying a strong axial magnetic field. However, even if this energy transfer is suppressed, the final beam energy spread is found to be still larger than what is predicted by the transverse-longitudinal cooling effect. The reason is that in addition to the Boersch effect, there exists another effect called longitudinal-longitudinal relaxation [15]. If the acceleration is fast (non-adiabatic) compared to the period of the electron beam plasma oscillation period, acceleration causes inhomogeneity in the electron density along the longitudinal direction in addition to the longitudinal beam cooling (Equation 5.330b in Ref. [1]). Relaxation between the potential and kinetic energy contributes to make the density homogenerous and result in energy spread increase. The time taken by this relaxation time is the plasma period $\tau_0 = 2\pi/w_0$, where $\omega_0 = \sqrt{4\pi e^2 n/m}$ is the plasma frequency and m is the electron mass.

Combining both the Boserch effect and this longitudinal-longitudinal relaxation effect, the final beam energy spread can be express as [1,16]

$$\Delta \tilde{E}_{\|f} = \left[\frac{1}{\pi \varepsilon_0} q n^{1/3} q V_0 + 2q V_0 k_B T_\| \right]^{1/2} . \qquad (2.14)$$

Here $\Delta \tilde{E}_{\|f}$ is the rms energy spread after acceleration and beam propagation; qV_0 is the beam energy and $T_\|$ is an increasing function of time or distance of beam propagation, which can be calculated from Equation (2.4) (Boersch Effect). All the beam energies are in units of eV; n is the beam density and q is the electron charge. The first term in the bracket corresponds to the longitudinal-longitudinal effect, and the second term is the transverse-longitudinal (Boersch) effect. The longitudinal-

14

longitudinal effect dominates in the initial acceleration and propagation phase when there are micro fluctuations of the beam density distribution. The energy spread due to the Boersch effect, on the other hand, increases monotonically until the longitudinal temperature reaches equilibrium. After a certain time of propagation, the Boersch effect will become the dominant source of the energy spread. According to the theoretical prediction, the rate of evolution of energy spread depends on the current density of the beam. The higher the beam density, the faster the beam energy spread increase in the longitudinal direction. For example, for a 5 keV, 135 mA beam with a initial beam size of 5mm, the contribution of the energy spread from the longitudinal-longitudinal relaxation reaches a constant value of ~1.5 eV within a couple of plasma oscillation periods after the electron gun. On the other hand, the contribution of the energy spread from the Boersch effect increases with the distance until it reaches the equilibrium. For particles coming off the emitting surface with a temperature of 0.1 eV, cooling down through acceleration and subsequently heating up to an equilibrium temperature of 0.067 eV via the Boersch effect with the effective relaxation time $\tau_{eff} \sim 2 \times 10^{-5} s$, the longitudinal energy spread from the Boersch effect contribution will increase from 0.1 eV at the emitter to ~1.5 eV at the distance of 25 cm from the emitter, to ~ 4 eV at the distance of 2 m from the emitter, and to 26 eV at equilibrium about 900 m away from the emitter. So after propagating a distance of 25 cm, the contribution of the energy spread from the Boersch effect is larger than that from the longitudinal-longitudinal effect and is the dominant source of the beam energy spread. The energy spread after long beam propagation can be expressed as

$$\Delta \tilde{E}_{\| f} = \left(2 q V_0 k_B T_{/\!/} \right)^{1/2} . \tag{2.15}$$

2.4 Scaling law

If the beams transport in a uniform focusing channel with a constant beam radius a, and beam propagation time satisfies $t \ll \tau_{eff}$, Equation (2.12) can be expanded by using Taylor series and only the linear term is taken, Taylor expansion of Equation (2.12) will be

$$k_B T_{//} = 2k_B T_{\perp 0} t / \tau_{eff} .$$ (2.16)

Substituting Equation (2.13) in (2.16), we find

$$k_B T_{//} = \frac{2k_B T_{\perp 0} t}{1.34} \frac{\pi^{3/2} n r_c^2 c}{\left(k_B T_{\perp 0} / mc^2\right)^{3/2}} \ln \Lambda .$$ (2.17)

Substituting $t = \frac{L}{v}$ (L is the distance corresponding to the beam propagation time t.) and using Equation (2.7), Equation (2.17) becomes

$$
\begin{aligned}
k_B T_{//} &= \frac{2}{1.34} \frac{\left(mc^2\right)^{3/2} \pi^{3/2} r_c^2 c}{\left(k_B T_{\perp 0}\right)^{1/2}} \frac{I}{qa^2 \pi v} \frac{L}{v} \ln \Lambda \\
&= \frac{\ln \Lambda}{1.34} \frac{\left(mc^2\right)^{5/2} \pi^{1/2} r_c^2 LI}{\left(k_B T_{\perp 0}\right)^{1/2} a^2 qc(mv^2)/2}
\end{aligned}
$$ (2.18)

where

$$\frac{1}{2} mv^2 = qV_0 .$$ (2.19)

V_0 is the acceleration voltage.

Different focusing strengths will change the beam radius a, and therefore the initial transverse temperature $T_{\perp 0}$. If the cathode temperature inside the cathode is T_c and the cathode radius is $r_{cathode}$, the beam initial transverse energy is

$$k_B T_{\perp 0} = k_B T_c \frac{r_{cathode}^2}{a^2} . \tag{2.20}$$

Substituting Equation (2.19) and (2.20) in Equation (2.18), one can obtain

$$k_B T_{//} = \frac{\ln \Lambda}{1.34} \frac{\left(mc^2\right)^{5/2} \pi^{1/2} r_c^2}{qc\left(k_B T_c\right)^{1/2} r_{cathode}} \frac{IL}{aqV_0} . \tag{2.21}$$

Because the Coulomb logarithm $\ln\Lambda$ is not sensitive to the beam density and temperature, we assume $\ln\Lambda \approx \cos nt$. Substitute Equation (2.21) in Equation (2.15), we obtain the scaling law of the Boersch effect as

$$\Delta \tilde{E}_{\|f} = \left(\frac{2\ln\Lambda}{1.34} \frac{\left(mc^2\right)^{5/2} \pi^{1/2} r_c^2}{qc\left(k_B T_c\right)^{1/2} r_{cathode}} \frac{IL}{a} \right)^{1/2} . \tag{2.22}$$

It is surprising that the longitudinal energy spread is not related to the beam energy. The beam longitudinal energy spread is proportional to the square root of the beam current, radius, and propagation length as

$$\Delta \tilde{E}_{\|f} \sim \left(\frac{IL}{a} \right)^{1/2} . \tag{2.23}$$

The logarithm scale of Equation (2.23) is

$$\ln \Delta \tilde{E}_{\|f} \sim \frac{1}{2} \ln \left(\frac{IL}{a} \right), \tag{2.24}$$

where $\ln \Delta \tilde{E}_{\|f}$ is proportional to the $\ln \left(\dfrac{IL}{a} \right)$ with a slope of 0.5. Experimental results will be compared with this scaling law in the next Chapter.

Chapter 3 : Design of a Retarding Field Energy Analyzer with Variable Focusing for Space-Charge-Dominated Electron Beams

3.1 Introduction

The University of Maryland Electron Ring (UMER) [4], currently under construction, is designed as a flexible and well-diagnosed tool for doing experiments on space-charge-dominated beams. To fulfill this requirement, it is necessary to design a compact high-resolution energy analyzer, which is suitable for several keV up to 10 keV space-charge-dominated electron beams used in UMER. A retarding field energy analyzer becomes the natural choice for low-energy electron beams because of its simplicity, compactness, and high signal-to-noise ratio output.

There are different types of retarding field energy analyzers as reviewed in Ref. [17]. Traditional parallel-plate retarding energy analyzers have been widely used in many applications, such as in plasmas [18], electron cloud diagnostics [19,20], ion beams [21], etc with relative resolutions in the range of $10^{-2} \sim 10^{-3}$ ($\Delta E/E$). Other than these traditional parallel-plate analyzers, there are also some other types of energy analyzers that have been built for different applications, such as large angle acceptance retarding-potential analyzer in a magnetic fusion experiment [22], gridless electrostatic retarding analyzer for ion temperature measurement [23], Wien filter

type analyzer for surface microanalyses [24], and cylindrical deflection energy analyzer used in low-energy ion scattering [25]. However, these analyzers either have low resolutions (worse than 10^{-3}) or the sizes are too big to fit into the UMER.

At the University of Maryland, a cylindrical retarding energy analyzer had been designed, which greatly improved the energy-spread measurement compared with a conventional parallel-plate energy analyzer [16]. Based on that design, a variable-focusing retarding field energy analyzer has been developed to further improve the resolution. This analyzer has several unique features compared to other electrostatic retarding field analyzers. (1). A focusing cylinder with a variable voltage is employed to provide optimum focusing of the beams. (2). The device is different from a Faraday cage analyzer. Its electron collector is at low voltage, which makes the measurement easier and more accurate than high-voltage measurement. (3). It has a compact structure. In the following sections, we first discuss the design of the new energy analyzer. Then, we will present the simulation results.

3.2 Design of the Retarding Energy Analyzer

Several generations of energy analyzers have been developed to measure the beam energy spread in a space-charge-dominated beam at the University of Maryland. The simplest parallel-plate retarding energy analyzer was developed and tested in the past [7]. It consists of two parallel plates. The first plate is grounded and the second one is biased to a negative high voltage to retard the electron beams. Only those particles whose longitudinal kinetic energy is higher than the retarding potential can pass this second electrode and reach the collector forming a current signal. Other electrons will be reflected. This structure has good resolution only for a beam with trajectories parallel to the axis of the energy analyzer. In reality, when electrons are emitted from the electron gun, the beam always has a finite divergence angle because of the initial emittance, space-charge effects, misalignment, etc. This divergence diminishes the resolution. The resolution of this analyzer is more than 40 eV for a 5 keV beam, much worse than what the experiments required. An important modification to this structure, in which a cylindrical focusing electrode is mounted on the retarding grid to provide focusing and retarding for the electron beams, has significantly improved the energy resolution to about several eV for a 10 keV beam [16]. This device has one shortcoming. The cylindrical electrode is electrically connected with the retarding electrode and it cannot provide proper focusing for the beams because two electrodes always stay at the same potential.

To further improve the energy analyzer resolution to less than 1 eV, we insulated the mesh electrically from the retarding/focusing cylinder and apply a controllable

small voltage between the two. The associated electric field provides a stronger radial focusing of the beamlet (entering through a small aperture in the upstream plate as shown in Figure 3.1). Essentially, the fields between the main cylindrical lens and the injection plate, on the one hand, and that between the main cylinder and the mesh, on the other hand, form two semi-bipotential electrostatic lenses. The first decelerates and focuses the beamlet, while the second accelerates and focuses it. The addition of the second lens provides an extra handle, which, by varying the voltage, changes the slopes of the trajectories so that the beamlet envelope can be made to pass the lowest potential point before the mesh with no transverse velocity. Single particle simulations using SIMION and beam envelope analysis inside the energy analyzer of this design were completed and compared with the last design, indicating that the resolution of the energy analyzer can be improved significantly to less than 0.2 eV for a 5 keV beam.

Figure 3.1 shows the schematic of the energy analyzer. The electron beam comes from the left. The beam first sees a grounded steel plate with a 1 mm diameter circular aperture through which a small beamlet passes into the high potential region. The high-voltage steel cylinder with a length of 2.5 cm and an inner diameter of 2.5 cm is supported by two machinable ceramic (MACOR) rings and is connected to the external high-voltage source to provide both deceleration and radial focusing of the beamlet. The retarding grid is a molybdenum wire mesh. The wire diameter is 0.05 mm and the mesh consists of 20×20 wires per square centimeter. The transmission rate of the grid, which is defined as the ratio of the open area of the hole to the total area of the surface containing the grid, is 80%. The mesh is soldered to a steel ring

with a thickness of 2.5 mm, which is held in place by a MACOR ring with a thickness of 2 mm and connected to the external high-voltage source to provide a retarding and focusing voltage. Behind the high-voltage mesh is a copper collector plate, from which the current signal is picked up by a 50 Ω BNC connector. With a length of 4.8 cm and a diameter of 5.1 cm, this energy analyzer can be easily inserted at any place in the beam line. Figure 3.1 (b) shows the electrical circuit of the analyzer. When the retarding voltage is at about the same potential as the beam energy, the kinetic energy of the electrons in the beam is too small (almost zero) to generate any secondary emission on the mesh. After electrons pass through the mesh, they will be accelerated to the collector forming a current signal. Possible secondary electrons from the collector will be suppressed by the reverse field on the collector surface. So the secondary electron effect is not a concern in the device.

(a)

High Voltage Input Pins

High Voltage Cylinder

Ground Shielding

Retarding Mesh

Collector

Signal Output

Electron Beam

Steel Washer

Insulating Material

(b)

High Voltage Cylinder   Retarding Mesh

Collector

Oscilloscope

Lab ground

Focusing voltage   Retarding voltage

Battery   High Voltage
power supply
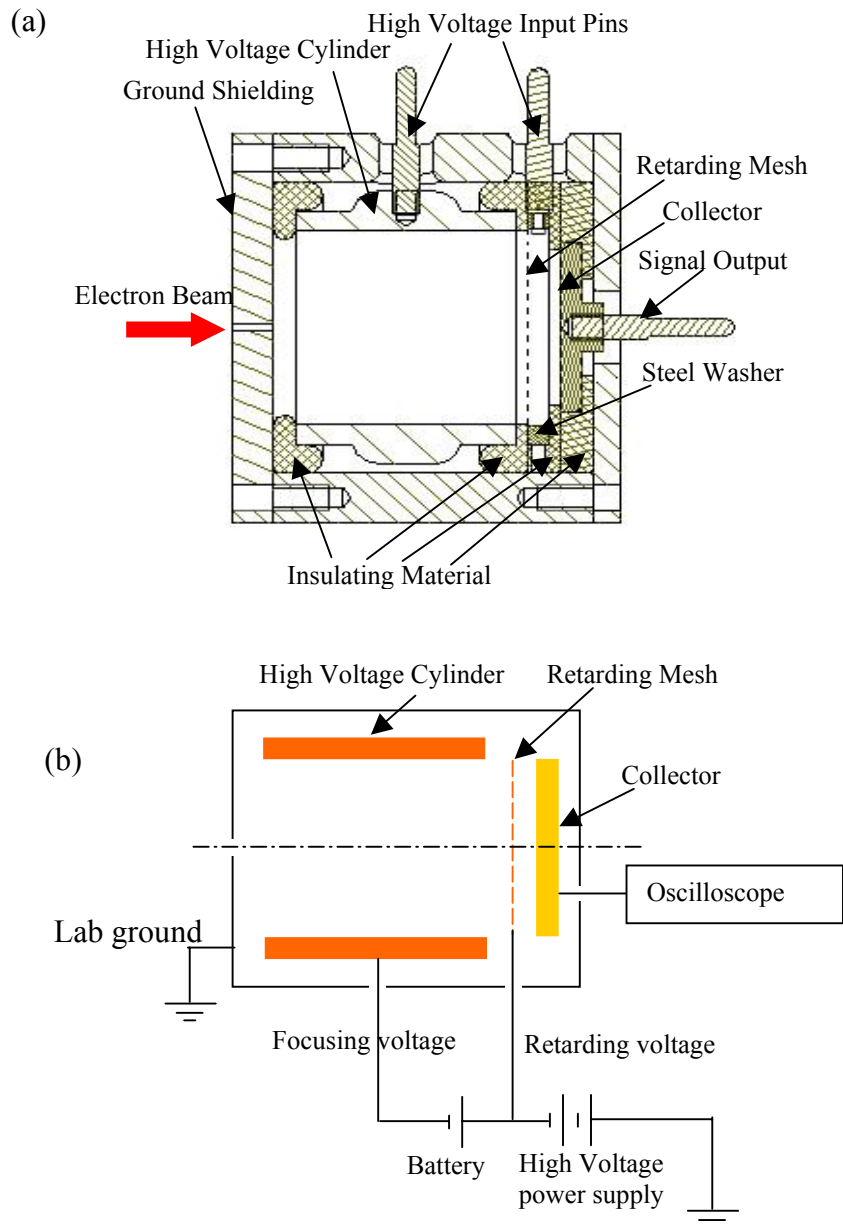
Figure 3.1. Schematic of the energy analyzer with variable-focusing cylindrical electrode. The length is 4.8 cm and the diameter is 5.1 cm. The aperture size is 1 mm in diameter. (a) Structure of the analyzer, (b) Electronic circuit.

3.3 Single Particle Simulation of the Retarding Energy Analyzer

A computer code called SIMION [26] is used to simulate the performance of the energy analyzer. SIMION is a PC-based, single particle, electrostatic code with the capability of handling the wire mesh. Figure 3.2 shows the electron trajectories and equipotential lines from a SIMION simulation for the previous design. Figure 3.3 shows the electron trajectories and equipotential lines from a SIMION simulation for the new design. In both cases, the beam is assumed to be monoenergetic, with kinetic energy of 10 keV and initial angular spread of 1°. The initial beam diameter is 1 mm, which is determined by the aperture size in the front plate. When the magnitude of the retarding voltage is above 10 kV, all the particles are reflected for both designs. For the magnitudes of the retarding potentials smaller than 10 kV, ideally, all particles should pass the mesh. However, due to the tilted beam trajectory, those particles with a smaller longitudinal momentum will be reflected back even though the total kinetic energy is 10 keV, larger than the retarding potential. The advantages of the independently-controlled focusing potential can be seen by comparing Figures 3.2 and 3.3. In both cases, the magnitude of the retarding voltage is 9999.5 V. From Figure 3.2 we see that most particles are reflected back with the previous design, due to the beam divergence at the location close to the mesh. But for the new design, as shown in Figure 3.3, where the magnitude of the focusing voltage is 130 V higher than the retarding voltage, all particles can pass through the mesh, which indicates a better resolution than the previous one. In Figure 3.4, we compare the corresponding simulated performance between the previous design and the new one for a 10 keV

beam with a 1° angular spread. The new design reduces the maximum error from 2 eV to 0.5 eV for a 10 keV monoenergetic beam with a uniform angular spread up to 1° off the longitudinal axis. It is very interesting to note that the resolution of the energy analyzer depends on the beam energy [16]. Table 3.1 shows the maximum errors of the new design for various differences between the focusing voltage and retarding voltage at 3 keV, 5 keV, and 10 keV beam energy.

Beam Energy (E)	3 keV	5 keV	10 keV
Relative Focusing Voltage	40 V	65 V	130 V
Energy Analyzer Maximum Error	0.15 eV	0.25 eV	0.5 eV

Table 3.1. Energy analyzer maximum error for different beam energy from SIMION simulation.
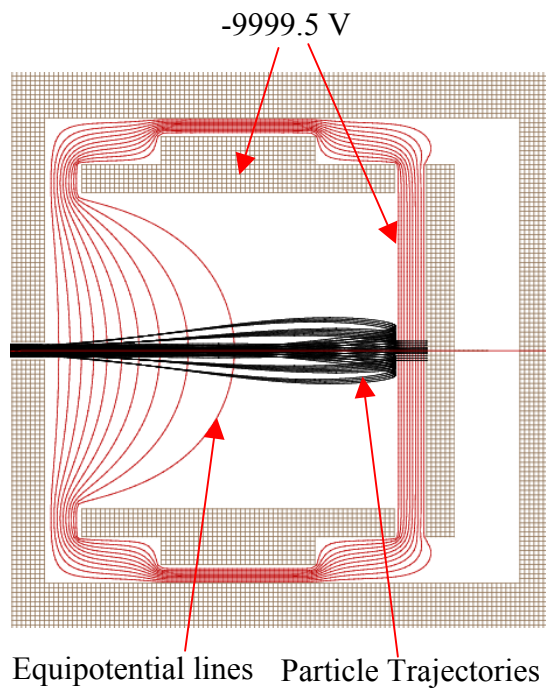
Figure 3.2. Equipotential lines and beam trajectories when the focusing cylinder and retarding mesh have the same potential of 9999.5 V.
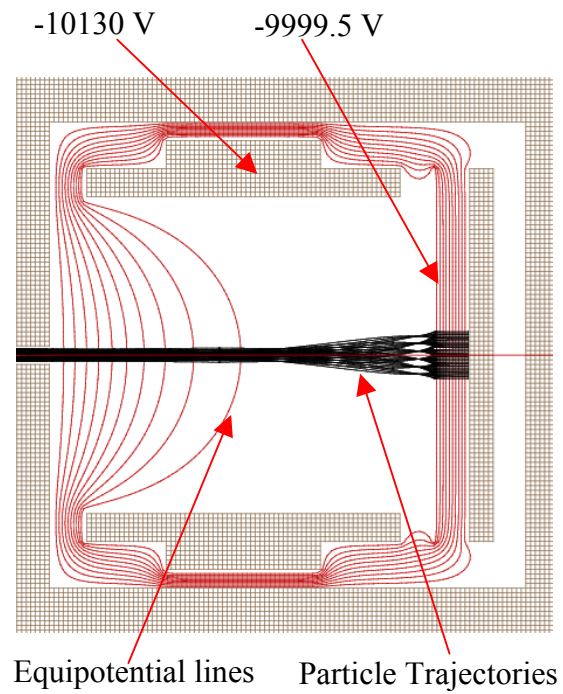
Figure 3.3. Equipotential lines and beam trajectories when the potential magnitude on the focusing cylinder is 130 V greater than the 9999.5 V on the retarding mesh.
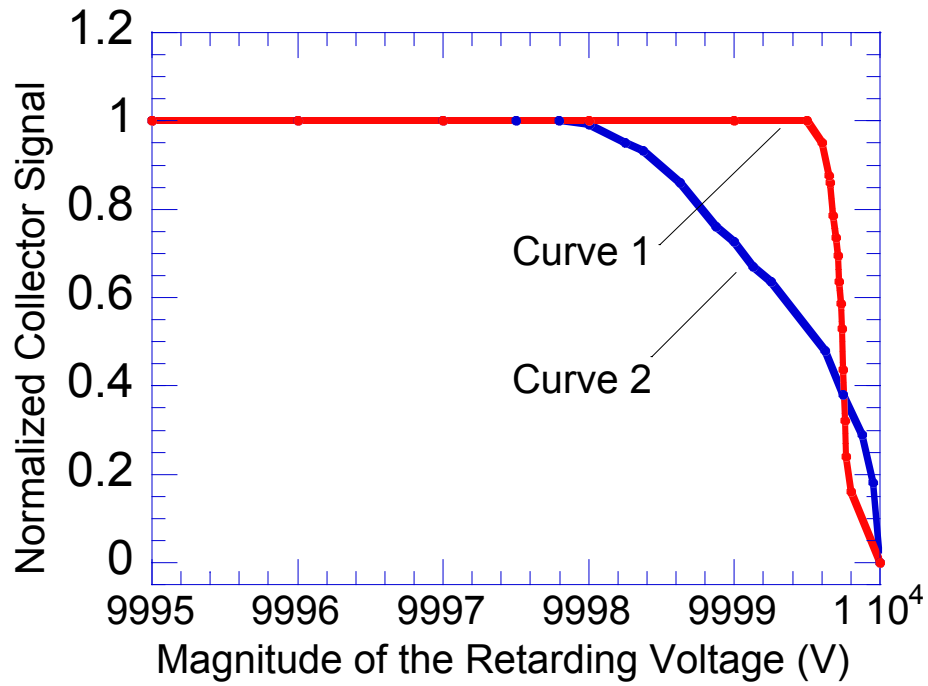
Figure 3.4. Simulation shows that, for the 10 keV beam with divergence angle of 1°, the energy analyzer with the magnitude of 130 V larger focusing voltage has a maximum error of 0.5 eV (Curve 1), while energy analyzer with same focusing voltage has a maximum error of 2 eV (Curve 2).

3.4 Beam Envelope Simulation of the Retarding Energy Analyzer

Single particle simulation using SIMION is not enough to completely explain the beam behavior and the device resolution because it does not take into account the space-charge effects and the beam emittance effects. We may study these effects by solving the beam envelope equation inside the analyzer with the paraxial assumption.

3.4.1 Theoretical electric fields on paraxial conditions

In the assumptions of paraxial motion, the particle trajectories remain close to the axis, the slope of the particle trajectories remain small. The azimuthal velocity must remain very small compared to the axial velocity. With these approximations, only the first-order terms in the expansions of the fields need to be considered, and expanding all quantities in terms of their values on the axis of the system can linearize the equations of motion. In place of the electric potential, we use the "voltage equivalent of the kinetic energy" on the axis, denoted by $V(z)$, as is common in charged particle optics. With this notation, the spatial potential $V(z)$ always has the same value as the beam kinetic energy. $V(z){=}0$ means the beam is fully stopped. The first-order of radial and axial electric-field components with a radius r off axis can be expressed as (see Equation 3.34 in Ref [1])

$$E_z = -V', \ E_r = \frac{1}{2}V''r = -\frac{r}{2}\frac{\partial E_z}{\partial z}. \tag{3.1}$$

To retard an electron beam with initial kinetic energy eV_0, the retarding mesh is set on $-V_0$ and the focusing cylinder on $-(V_0 + \Delta V_0)$, both voltages referenced to the

29

lab ground. Here, ΔV_0 is a difference between the voltages on the focusing cylinder and the retarding mesh. If the potentials in the device are shifted up $V_0 + \Delta V_0$ compared with the actual potentials, we obtain new potential values on the electrodes which are shown in Figure 3.5 (a). The system can be described by two electrostatic lenses. The first lens is defined by the grounding plate with potential $V_0 + \Delta V_0$ and the focusing cylinder with potential zero and provides deceleration and focusing of the beamlet. The second lens is defined by the focusing cylinder and the retarding mesh with potential ΔV_0 and provides acceleration and focusing.

We may regard the first and the second lenses as half-lenses of a bipotential lens, where the upstream and downstream parts are cut off by the injection plate and the retarding mesh, respectively, at the midplanes. Let us define the axial position of the midplane of the first lens by z_1 and that of the second lens by z_2 using two bipotential lenses. For a bipotential lens as shown in Figure 3.5 (b), when two cylinders have the same radii ($b_1 = b_2 = b$) and are separated by an infinitesimally small gap ($d \to 0$), the potential distribution on the axis can be approximated with a good degree of accuracy by (see Equation 3.129 in Ref. [1])

$$V(z) = \frac{V_1 + V_2}{2} + \frac{V_2 - V_1}{2} \tanh\left(\frac{1.138}{b} z\right). \qquad (3.2)$$

From the conditions $z = z_1$, $V(z_1) = V_0 + \Delta V_0$, and $V(z - z_1 \to \infty) = 0$ (our device length is twice the radius, so $V(z - z_1 = 2b)$ is very close to 0), we find that $V_1 = 2(V_0 + \Delta V_0)$ and $V_2 = 0$. So, the potential on the axis for the left lens can be expressed as

$$V_L(z) = (V_0 + \Delta V_0) - (V_0 + \Delta V_0)\tanh\left(\frac{1.138}{b}(z - z_1)\right). \qquad (3.3)$$

The second half-lens at the mesh has to be treated like the first one, except that now only the region $z < z_2$ is of practical interest. From the conditions $z = z_2$, $V(z_2) = \Delta V_0$, and $V(z - z_2 \to -\infty) = 0$, we get the potential on the axis for the second lens as

$$V_R(z) = \Delta V + \Delta V \tanh\left(\frac{1.138}{b}(z - z_2)\right). \qquad (3.4)$$

By superposition of the voltages from the two solutions, and shifting the total potentials ΔV_0 down as shown in Figure 3.5 (c), we find the desired $V(z)$ along the axis between $z_1 < z < z_2$

$$V(z) = V_L(z) + V_R(z) = (V_0 + \Delta V_0) - (V_0 + \Delta V_0)\tanh\left(\frac{1.138}{b}(z - z_1)\right)$$
$$+ \Delta V_0 \tanh\left(\frac{1.138}{b}(z - z_2)\right) \qquad ,(3.5)$$

which is satisfied with $V(z = z_1) = V_0$ and $V(z = z_2) = 0$.
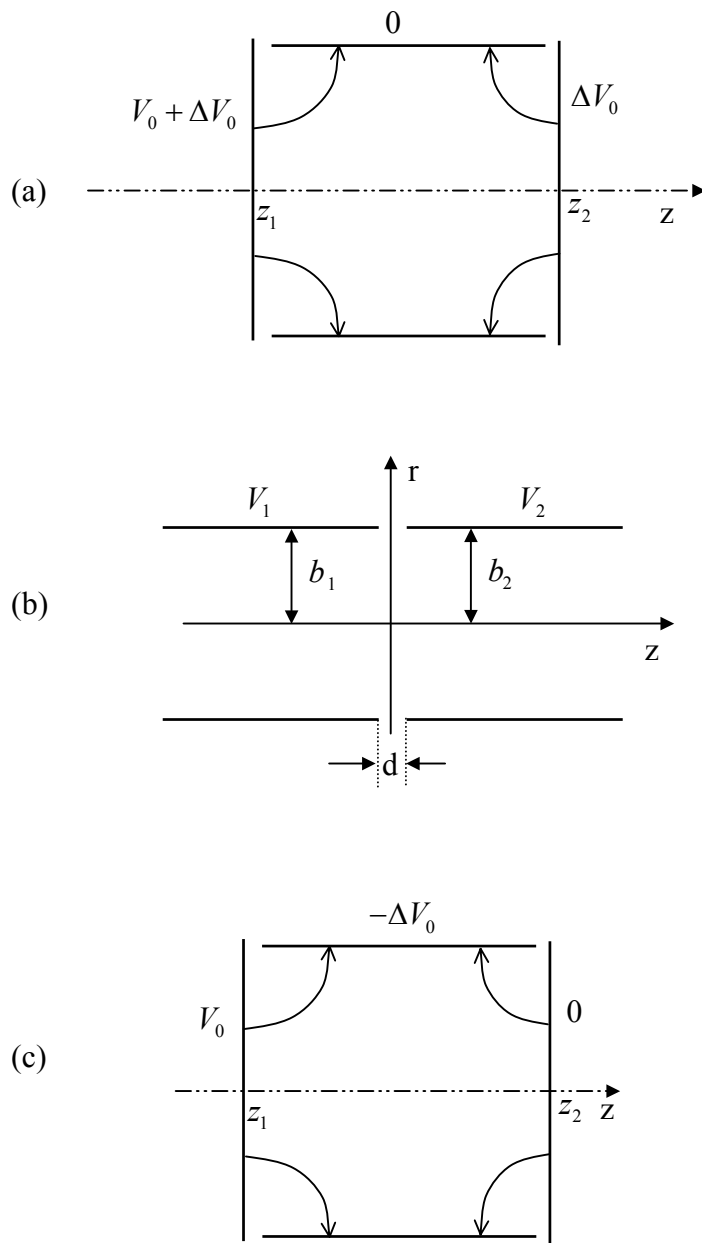
Figure 3.5. (a). Electrodes with different potentials inside the energy analyzer. (b). Bipotential lens formed by two coaxial tubes with the same radius at different potentials. (c). Electrodes with different potentials inside the energy analyzer. (Typical electric field lines are shown for $\Delta V_0 > 0$).

The potential distribution inside the energy analyzer also can be obtained using numerical solution. We used the software SOURCE [27] to solve the potential distribution inside the energy analyzer. This code computes the potential distribution using the second-order finite element method. It is fast and the relative error can be as small as 10^{-8}. The small gap effects between different electrodes are also considered in this numerical calculation. The potential $V(z)$ and the two first derivatives, $V'(z)$ and $V''(z)$ on the axis are shown in Figure 3.6 (a)-3.6(c) in the red solid lines. In this calculation, the beam energy is 5000 V, the focusing voltage is -5120 V, and the retarding voltage is -5000 V (both relative to the lab ground). In terms of the voltage equivalent of the beam energy (referenced to the cathode voltage), the potential at the entrance plate is 5000 V (the lab ground is at 5000 V) and the potentials on the retarding mesh and the focusing cylinder are 0 V and -120 V, respectively. According to Equation (5), theoretical results of the potential $V(z)$ and the two first derivatives, $V'(z)$ and $V''(z)$ on the axis are shown in the same figure in the blue dotted lines. We find that the theoretical approximation agrees with the numerical results very well on the axis. The gap effect can be ignored on the axis in the calculation.

(a)

(b)

(c)
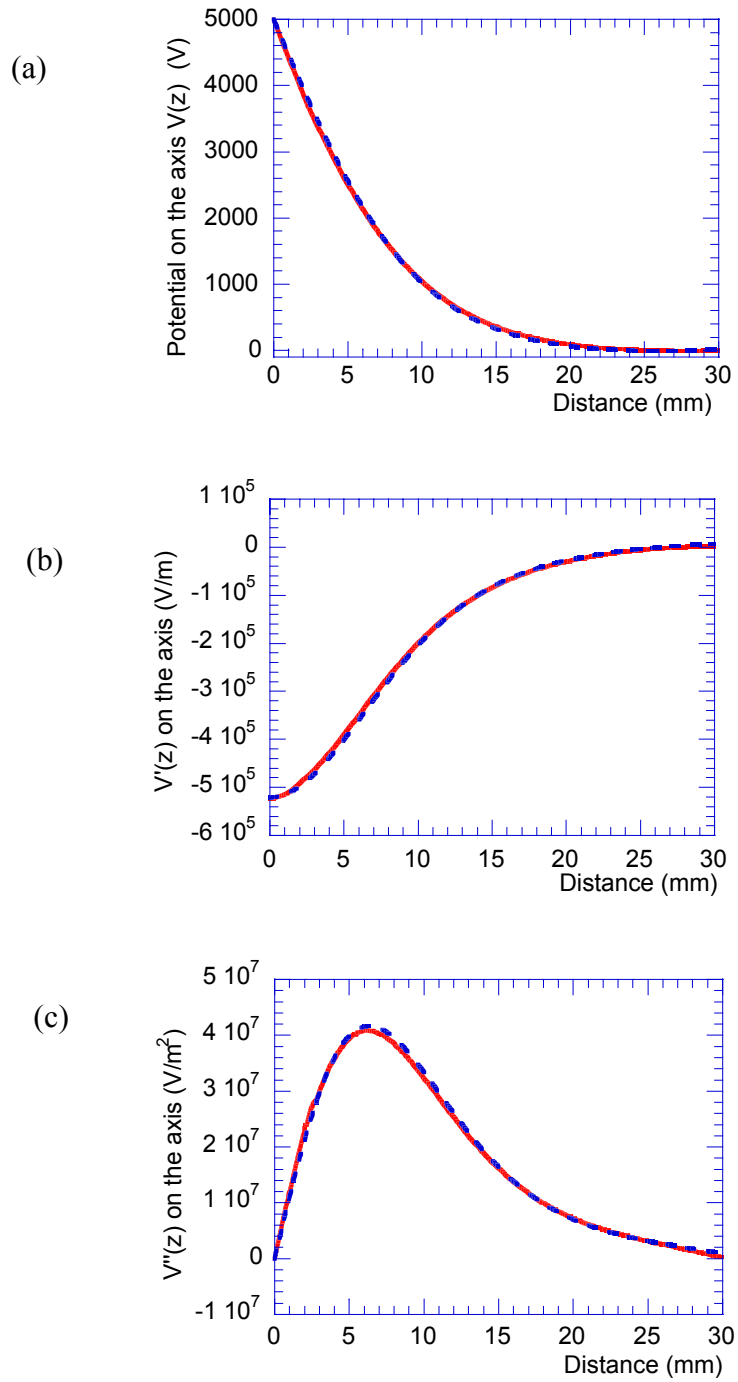
Figure 3.6. Potential equivalent and derivatives on the axis. Beam energy is 5000 eV, the voltage equivalents on the mesh and the focusing cylinder are 0 V and − 120 V respectively. Dotted line (in blue color) is calculated from the theoretical formula. Solid line (in red color) is from numerical calculations.

3.4.2 Aperture effect on the beam

When the beam comes from the left side, it first passes through the aperture, which was not considered when we calculated the electric field above. The aperture size is 1 mm in diameter, which is decided by our previous experimental experience. The small aperture size helps to reduce the space-charge effects and the emittance effect in the measurement. The relation of the beam emittance and the beam size is $\varepsilon_n \propto 1/r$ and the perveance is $K \propto 1/r^2$. Thus, the ratio of the space-charge to the emittance effect decreases with beam size. However, if the aperture size is too small, the signal received by the collector will be too small to be distinguished from the noise. In our experiment, the signal noise level is about 1 mV. The signal we take must be bigger than 10 mV (about 0.2 mA beam current) to reduce the measurement error.

This aperture has a lens effect. It is shown that near the axis in the plane of a circular aperture, between two fields of E_1 and E_2, there exists a lens whose focal power for particles of energy eV_0 is decided by (see Equation 3.134 in Ref. [1])

$$\frac{1}{f} = \frac{(E_2 - E_1)}{4V_0}. \qquad (3.6)$$

A parallel electron beam, after passing through an aperture of radius r_0 and entering a retarding field, will have a divergence of

$$\theta \approx r_0 / f. \qquad (3.7)$$

If we measure a beam with energy of 5 keV, we set the focusing voltage at −5120 V and retarding voltage at −5000 V. Inside the analyzer, the electric field E_2 near the aperture is $\sim -5.2 \times 10^5$ V/m from Figure 3.6 (b), and the electric field E_1 outside the

energy analyzer is almost zero. According to Equation (3.6), $1/f = -26 \ m^{-1}$. The negative sign means a divergent effect. From Equation (3.7), the divergence angle is about ~ 0.01 rad when the aperture size is 1 mm diameter for a parallel beam. This divergence angle will be used as initial beam slope in the following envelope calculation.

3.4.3 Beam envelope in the energy analyzer

In this section, we will study the beam dynamics using the paraxial envelope equation, including both self-fields and emittance effects. If the voltage equivalent of the kinetic energy on the axis is $V(z)$, according to Equation (3.51) and (4.79) in Ref. [1] and if the angular momentum of the electrons is ignored (since the axial magnetic field at the cathode is zero in our case), the envelope equation takes the form

$$r_m{''} + \frac{V'(z)}{2V(z)}r_m{'} + \frac{V''(z)}{4V(z)}r_m - \frac{K}{r_m} - \frac{\varepsilon_n^2}{\beta^2\gamma^2 r_m^3} = 0 \, . \qquad (3.8)$$

In the equation, the second term contains the effect of the axial electric field (acceleration or deceleration), the third term represents that of the radial electric field (focusing or defocusing), the fourth term represents the self-field of the beam (K is the generalized perveance [see Equation 4.23 in Ref. [1]]), and the fifth term represents the defocusing force due to the emittance. Note that ε_n is the normalized emittance, which is a constant during acceleration and related to the un-normalized emittance ε by $\varepsilon_n = \beta\gamma\varepsilon$, where β and γ are the relativisic velocity and energy factors.

For the envelope equation to be valid, the kinetic energy of the beam in the longitudinal direction must always be at least approximately ten times larger than that in the transverse direction. During the calculation, we set the beam energy at 5000 eV

(corresponding to the voltage equivalent $V(0)$ of 5000 V) and the voltage equivalent

of the mesh at 100 V (the beam has kinetic energy of 100 eV at mesh). By doing this,

the beam is not fully stopped at the mesh and we can make sure that $\beta_r \ll \beta_z$ is

always valid inside the device. The initial beam size and its derivative are

$r_m(z=0)$=0.5 mm and $r_m{}'(z=0)$=0.01, respectively. The normalized emittance ε_n is

7 μm and the beam current is 0.2 mA.

Let us first look at the effects of the axial electric field and the transverse

focusing field (the second and third term in Equation (3.8)) in the envelope equation

for different relative focusing voltages. Figure 3.7 (a) and 3.7(b) plot such results,

with Fig. 3.7(a) for the axial field and Fig. 3.7(b) for the transverse focusing field. In

the figure, the solid lines are for a relative focusing voltage ΔV_0 of 0 V and the

dashed line for ΔV_0 of 120 V. $V'(z)/2V(z)$ in Fig. 3.7(a) is negative, hence

defocusing for a divergent beam, except for the 120V case in the last 4 mm, where

this term becomes positive. In this case, the lowest potential on the axis, which is

located at 4 mm before the mesh, is about 7 V below the mesh potential. The term

$V''(z)/4V(z)$ in Fig. 3.7(b) is always focusing over the entire distance along the axis.

We can see that when the relative focusing voltage is a little higher, the device has a

larger focusing strength at the position close to the mesh. As we will see later, this

stronger focusing will help improve the device performance.

(a)

(b)
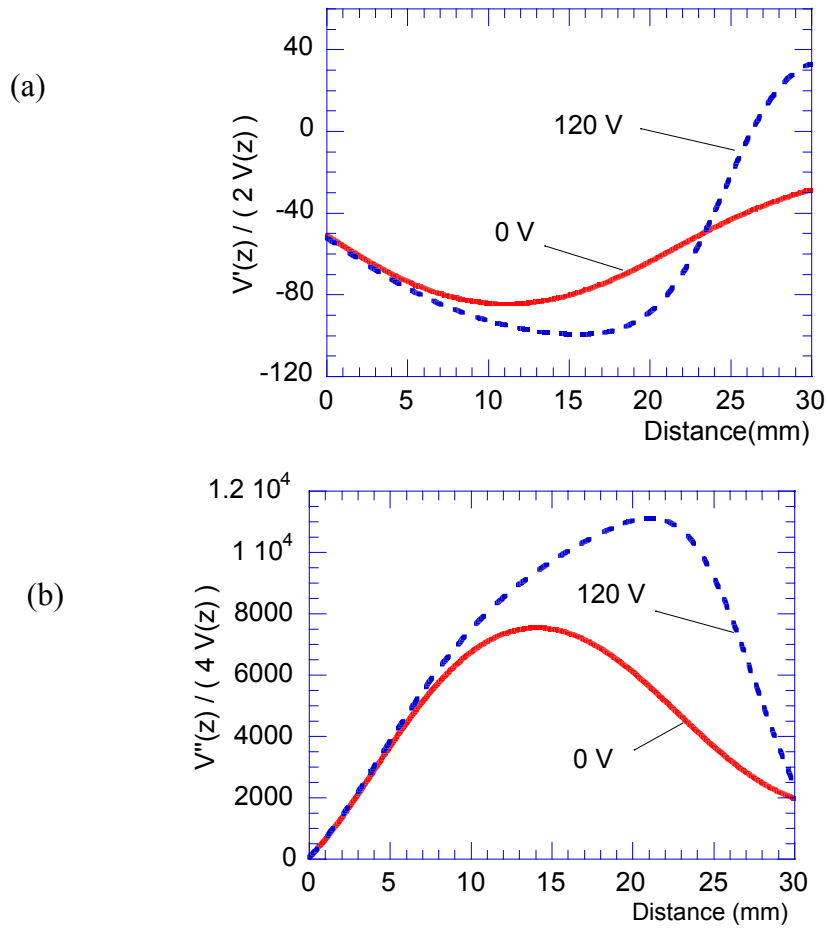
Figure 3.7 (a). Effect of axial electric field (Second term in Eq. (3.8)) for different relative focusing voltages. (b). Effect of focusing field (Third term in Eq. (3.8)) for different relative focusing voltages.

Figure 3.8 plots the beam envelopes at different relative focusing voltages. The beam trjectories at the lowest potential position (we call it the retarding point in the following text) will determine the device performance. With a higher voltage difference ΔV_0, the retarding point is not always on the mesh, but maybe moved to somewhere before the mesh, as shown in Fig. 3.8, where these retarding points are represented by small circles on the beam envelope curves. To optimize the device performance, we need to set the focusing strength such that the beam envelope has a zero slope at the retarding point. Let us look at the different beam envelopes in Fig. 3.8. In the figure, as the relative focusing voltage ΔV_0 increases from 0 V to 100 V, the beam size and the slope θ at the retarding point decreases. From 100 V to 160 V, the beam passes the retarding point almost perpendicularly (the slope of the beam envelope is almost zero). As the relative focusing voltage increases further to 200 V, the beam becomes overfocused, and the magnitude of the beam slope increases again. Since only the axial kinetic energy is effective to overcome the retarding potential, the coherent error of the beam energy caused by this slope inside the device can be calculated as

$$\Delta E = E \sin^2 \theta . \qquad\qquad (3.9)$$

Here, E is the beam energy at the retarding point and θ is the beam slope at the same position. Using Equation (3.9), the device resolution limited by the beam slope can be calculated. Figure 3.9 plots this energy spread errors at different relative focusing voltages. In the figure, the relative focusing voltage varies from 0 V to 200 V. The energy spread error decreases when the relative focusing voltage increases from 0 V
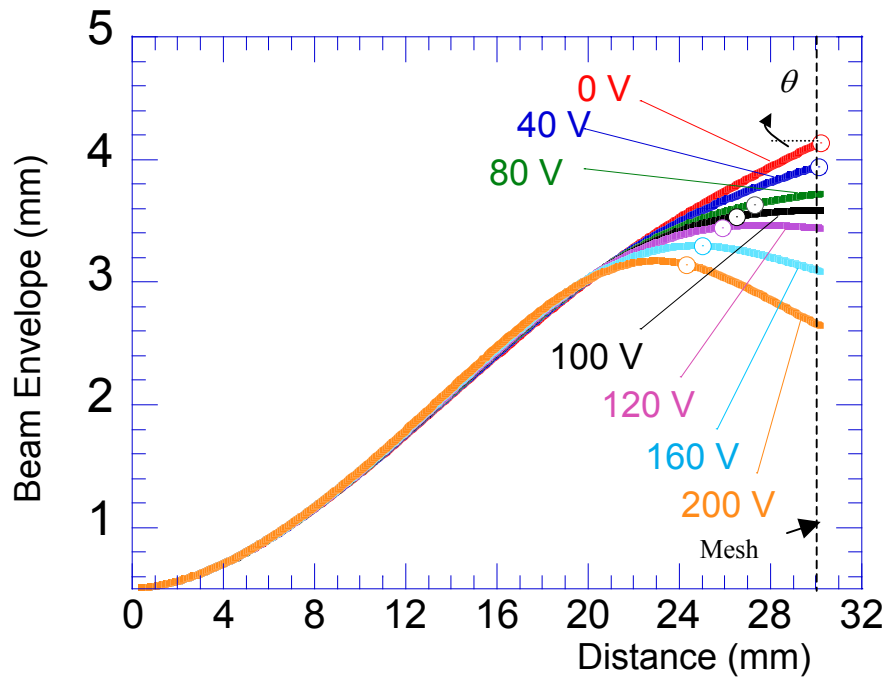
Figure 3.8. Beam envelope inside the device at different relative focusing voltages for a 5 keV beam. The point on the curve shows the position of the lowest potential on the axis at different relative focusing voltages.
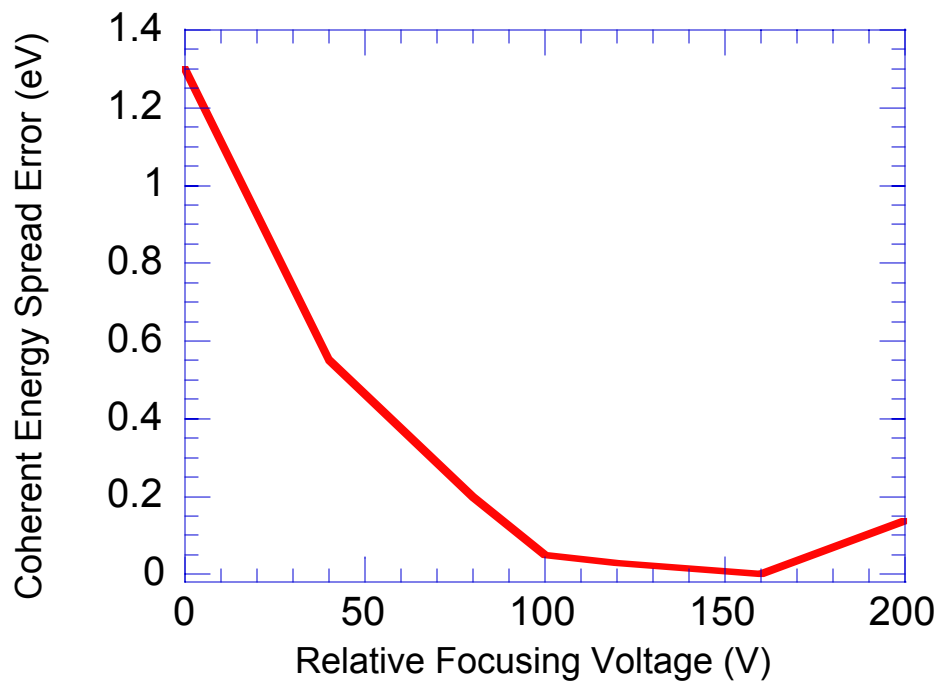
Figure 3.9. Coherent error caused by the beam divergence vs. the relative

focusing voltages.

to 100 V. It reaches a minimum of less than 0.1 eV for the relative focusing voltage between 100 V and 160 V. When the relative focusing voltage gets larger than 160 V, the energy spread error increases again due to the over focusing. This calculation shows the dependence of the energy spread error on the focusing cylinder voltage and demonstrates the advantages of using a variable focusing voltage in the device. In the experiment, we will vary the focusing voltage and find the optimum point empirically.

With the optimized focusing voltage, the contribution to the measured beam energy spread due to the coherent transverse motion is minimized. However, the energy spread associated with the random transverse motion due to the non-zero transverse beam emittance (inside the envelope, the particles still have random transverse motion) cannot be corrected with this focusing scheme. As a matter of fact, this is part of the longitudinal energy spread that we are interested in measuring.

In Figure 3.8, the potential at the retarding point drops from 100 V to 53 V as the relative focusing voltage increases from 100 V to 200 V. Relative to the potential at the retarding mesh, the potential at the retarding point is lower than that at retarding mesh from 0 to 47 V when the focusing voltage increases from 100 V to 200 V as shown in Figure 3.10. When the relative focusing voltage magnitude is 120 V, the voltage at the retarding point is only 6 V lower than the retarding mesh. If we fix the relative focusing voltage magnitude at 120 V, then change retarding voltage from 0 to 50 V, the relative potential at the retarding point changes only 0.5 V. This small difference between the retarding point and the retarding mesh have no big influence

(about 1%) in the energy spread measurement when we take the differential at the retarding mesh, not the retarding point.
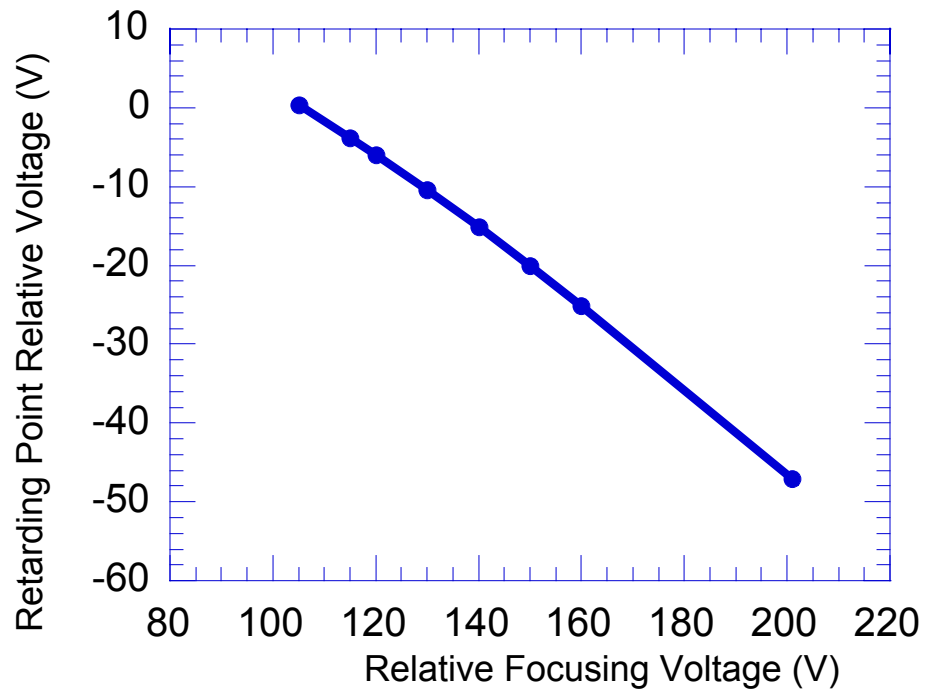
Figure 3.10. Relative voltage of the retarding points to the mesh at the different focusing voltages for 5 keV beam.
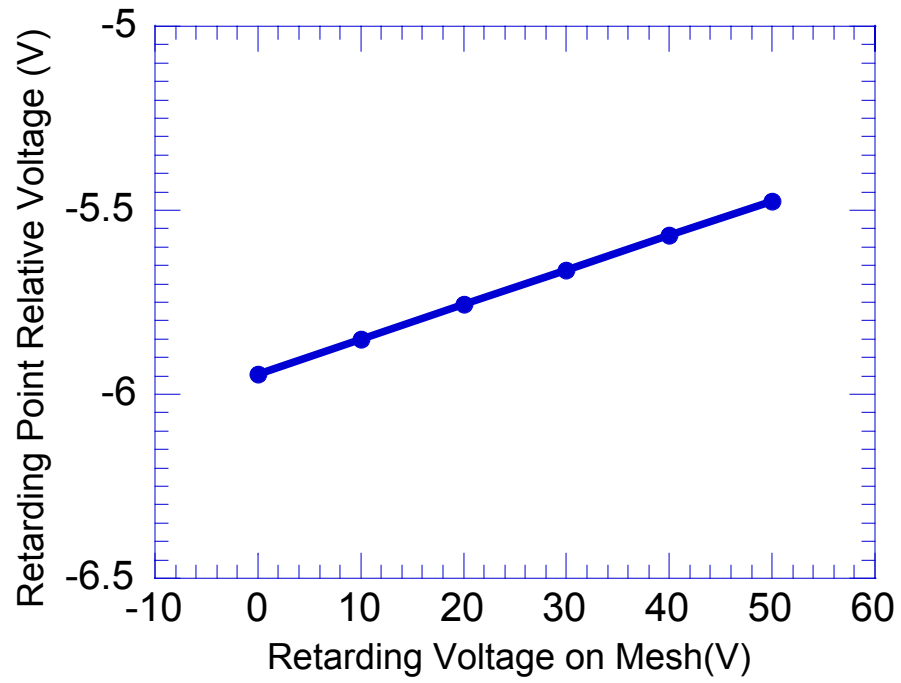
Figure 3.11. Relative voltage of the retarding points to the mesh at the different

retarding voltages for 5 keV beam when the relative focusing voltage is 120 V.

Chapter 4 : Beam Test of the Analyzer in Space-Charge-Dominated Electron Beams

4.1 Introduction

We have designed, built, and tested a high-resolution variable-focusing retarding field energy analyzer for space-charge-dominated electron beams. We tested the analyzer at the distance of 25 cm from the anode of a thermionic triode gun with a variable accelerating potential ranging from 3-5 kV and beam current ranging from 70-135 mA.

From the experiment, we found the longitudinal space-charge effect within the analyzer itself can cause errors in the measurement of the energy spread and the optimum focusing voltage has a wide operating region. Therefore, understanding the operation of the energy analyzer is critical in the measurement. With proper operation, this energy analyzer can achieve a relative resolution of 10^{-4} according to the design and testing.

The response of this energy analyzer is fast. It can be used to measure the beam energy with ns temporal resolution. The measured beam energy spectra are both temporally and spatially resolved. Retarding voltage and focusing voltage can be automatically controlled with a fast high-resolution computer-controlled system, which permits the automatic acquisition and analysis of huge amounts of reliable

data. The use of a computer-automated system greatly improves the experimental efficiency.

In the following sections, we first show the experimental setup. Then we will show the experimental results with the proper operation of the energy analyzer. Two important operation methods (optimum focusing voltage and small current density of the sampling beamlet) are pointed out. Experimental results will be compared with the theoretical prediction and possible sources causing the errors will be analyzed. Finally, we will present a novel method of obtaining the beam impedance between the cathode and the grid of the gun indirectly from the beam mean energy measurement.

4.2 Experimental Setup for the Beam Test of the Analyzer

The experimental setup, as shown in Figure 4.1, consists of a gridded thermionic electron gun, a solenoidal magnetic lens, and a diagnostic chamber. Figure 4.2 shows the picture of the energy analyzer test. The energy analyzer is located in the diagnostic chamber after the solenoid. The distances to the solenoid and energy analyzer from the anode of the gun are 11 cm and 24 cm, respectively. The solenoidal magnetic field extends less than 10 cm from its center, so there is no magnetic field inside the energy analyzer and the electron gun. By varying the solenoid strength, the particle density at the aperture plate and, therefore, the total beam current entering the analyzer can be controlled. The energy analyzer can be moved across the beam by a linear feedthrough. A movable phosphor screen, down the beamline from the diagnostic chamber, is used to measure the beam position and envelope. An automated measurement system is set up to measure the beam energy profiles and analyze, data promptly.

46
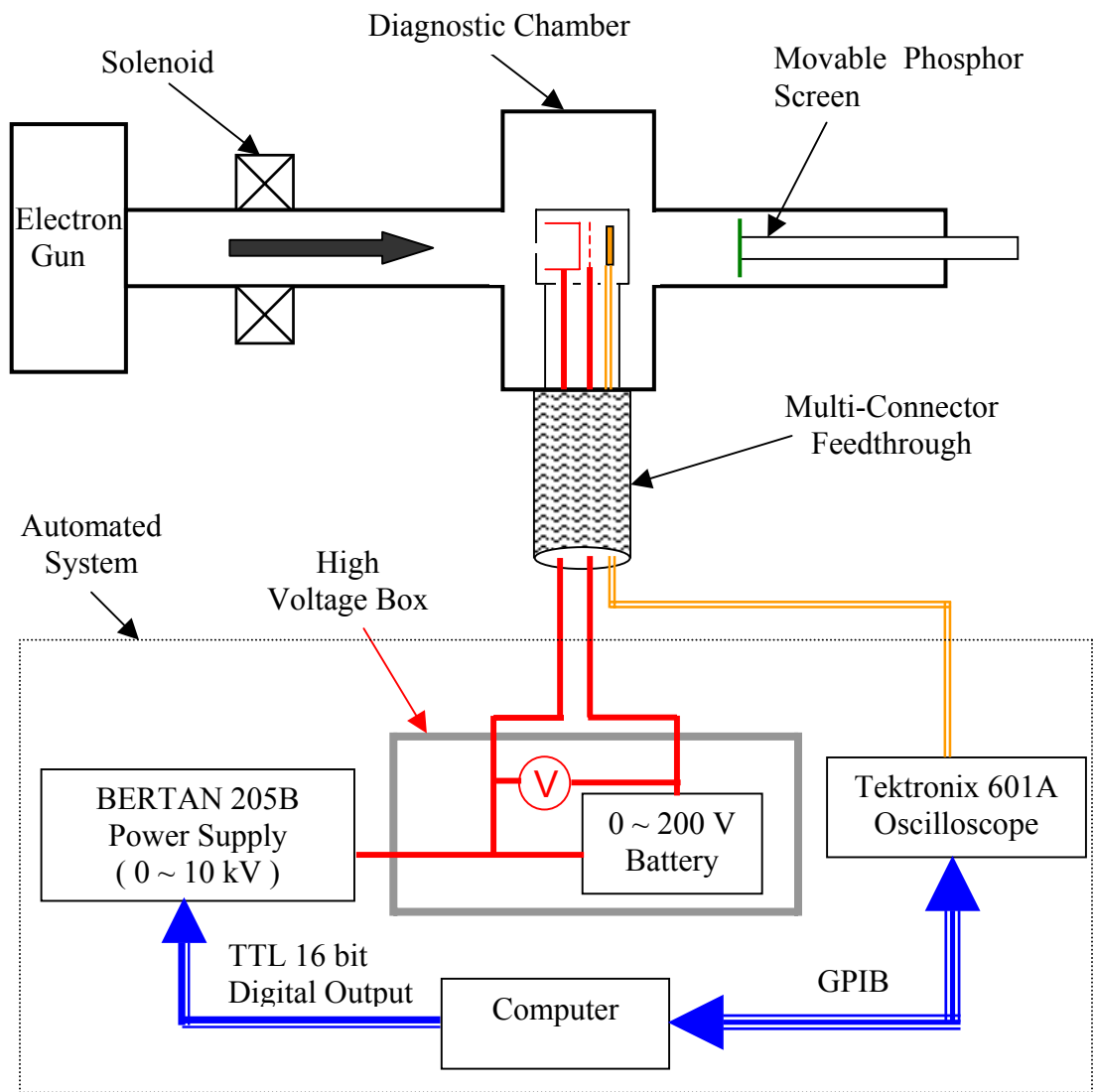
Figure 4.1. Experimental setup for the energy analyzer test.
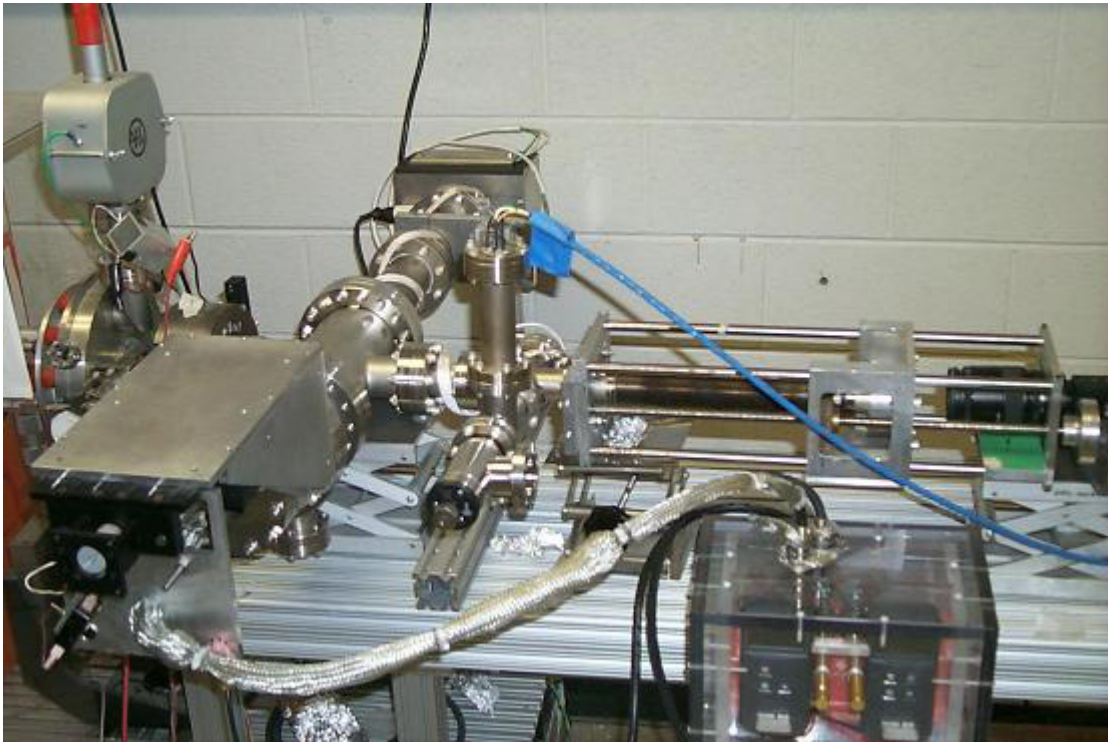
Figure 4.2. Photo of the energy analyzer test stand.

4.2.1 Description of the Electron Gun

Figure 4.3 shows the detailed schematic drawing of the electron gun [28]. The electron cathode assembly has a Pierce-type geometry and a planar configuration consisting of the heater, cathode, and grid. The radius of the cathode is 4mm and the heated area is around 0.5 cm^2 [29]. With such a small heated area, the heating inhomogeneity is not a problem. The grid consists of tungsten wire coated with titanium. The grid-cathode spacing is very small, about 0.11 mm. The whole cathode assembly is mounted to a support through bellows. The focusing electrode is connected to the grid and both are at the same high electrical potential. The anode and the field-shaping electrodes form a Pierce geometry. The distance between the cathode and anode is adjustable by means of micrometers to anywhere between 9.3 mm and 23 mm, allowing us to change the gun perveance. The anode aperture with a diameter of 1 cm is covered with a molybdenum mesh to reduce defocusing effects. The screening factor of the mesh is 14.3 %. An aperture plate is located downstream of the anode hole for the purpose of beam profiling and diagnostics. The distance between the anode wire mesh and the aperture plate is 1cm. The aperture includes eight circular holes with monotonically increasing diameters, one pepperpot, one slit, and two multiple-beamlet configurations. A built-in fast current transformer (Rogowski Coil) is located after the aperture plate to measure the beam current. This gun also has a gate valve to isolate the cathode from the rest of the system. The gate valve is only open during experiments, while at other times or during system installation, the gate valve is closed to protect the cathode.
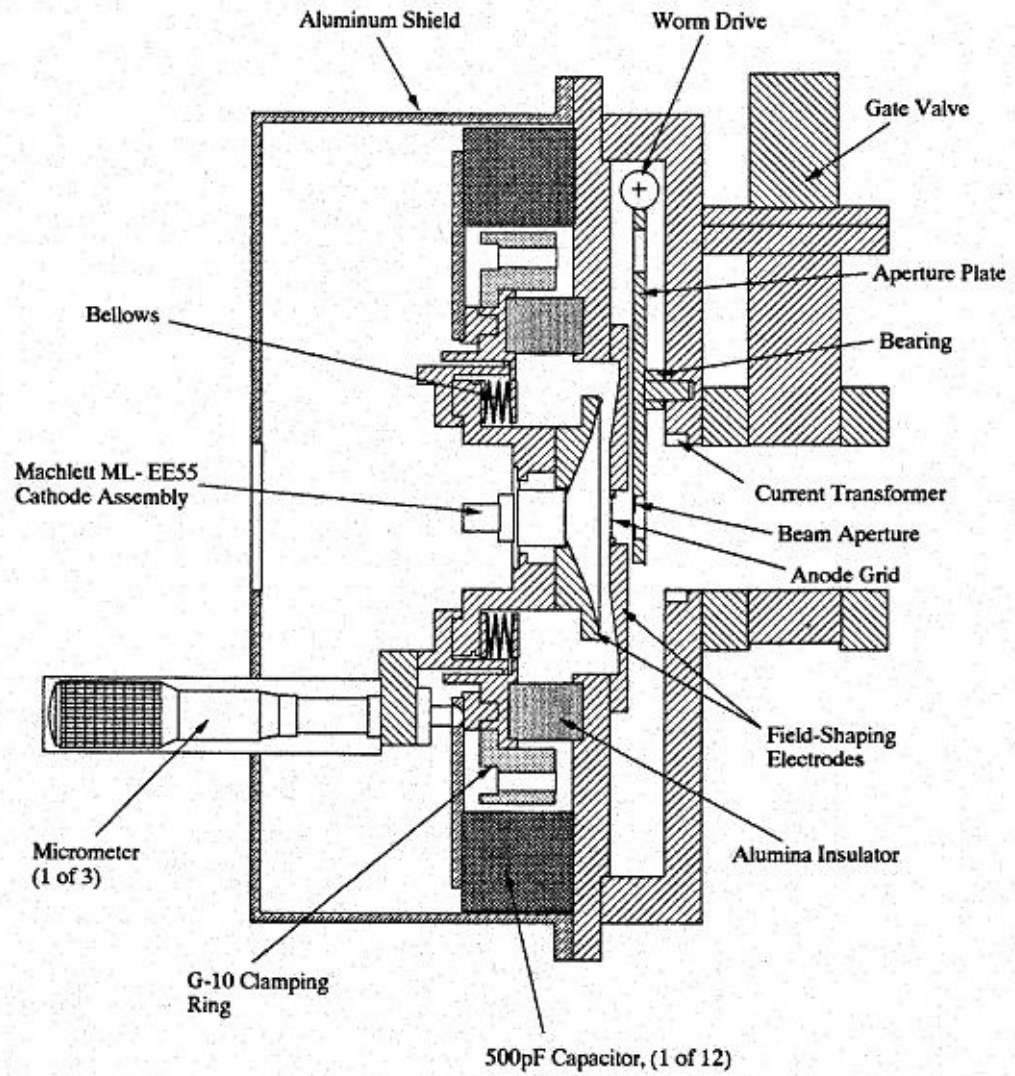
Figure 4.3. Schematics of the gridded electron gun

The gun electronics consist of a high-voltage supply for the anode grid, an AC power supply for the cathode heater, a DC cathode-grid bias supply (30 V to suppress the beam), and a grid-cathode pulser which provides a fast pulse signal between the cathode and grid to create the beam pulse. This pulser is triggered by an external triggering circuit. Figure 4.4 shows the circuit diagram for the electron gun [28]. High voltage is applied to the anode grid through a 1 MΩ resistor, which protects the high-voltage power supply from damage in the event of a large discharge when the power supply turns off. All the electronics are located in a high-voltage deck, which is isolated from the ground and charged up to −10 kV, except for the external triggering circuit, which is at the low voltage and is connected to the high-voltage electronics by fiber optics and an insulated transformer. The cathode is biased by positive DC voltage (30 V) relative to the grid to cut off the beam current. During emission, the grid-cathode pulse generator produces a negative pulse (-60 V) between the cathode and the grid to turn on the beam. The pulser signal is formed with a transmission line and the length of the transmission line, which is variable, determines the beam pulse width. In this experiment, we use a length of the transmission line of about 10 m to produce a 100 ns beam pulse. When the DC charging voltage is above -130 V(in the experiment, it is -160 V), the transistor works in the avalanche state. The avalanche transistor is turned on with the external triggering circuit. A typical grid-cathode pulser signal is shown in Figure 4.5 and the pulser amplitude is above 60 V with a rise time of 2 ns. To save the cathode lifetime, the external trigger is run at 60 Hz. To avoid harmful effect from the magnetic field produced by the heater current,

51

synchronization must be made between the pulse and the AC line voltage such that the beam is emitted when the line voltage is at the zero crossing.
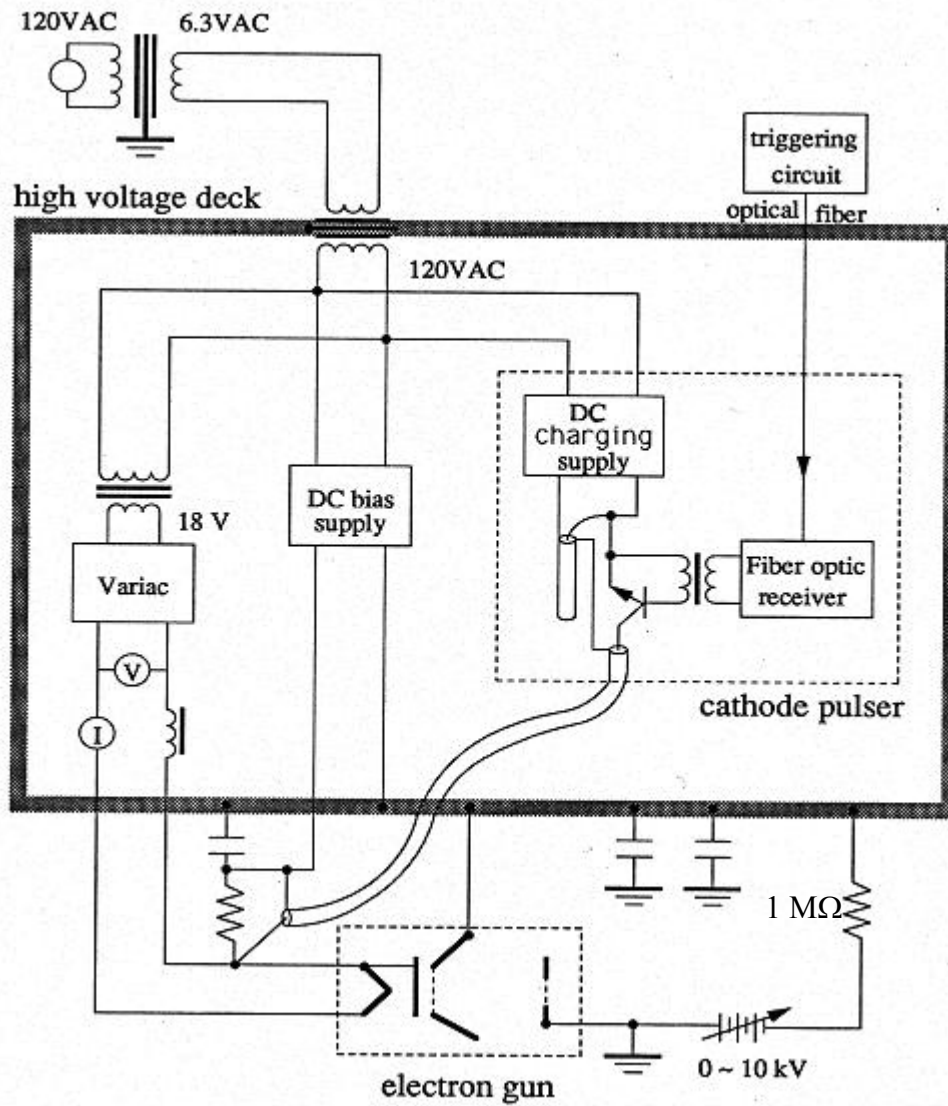
Figure 4.4. Circuit diagram for the electron gun.
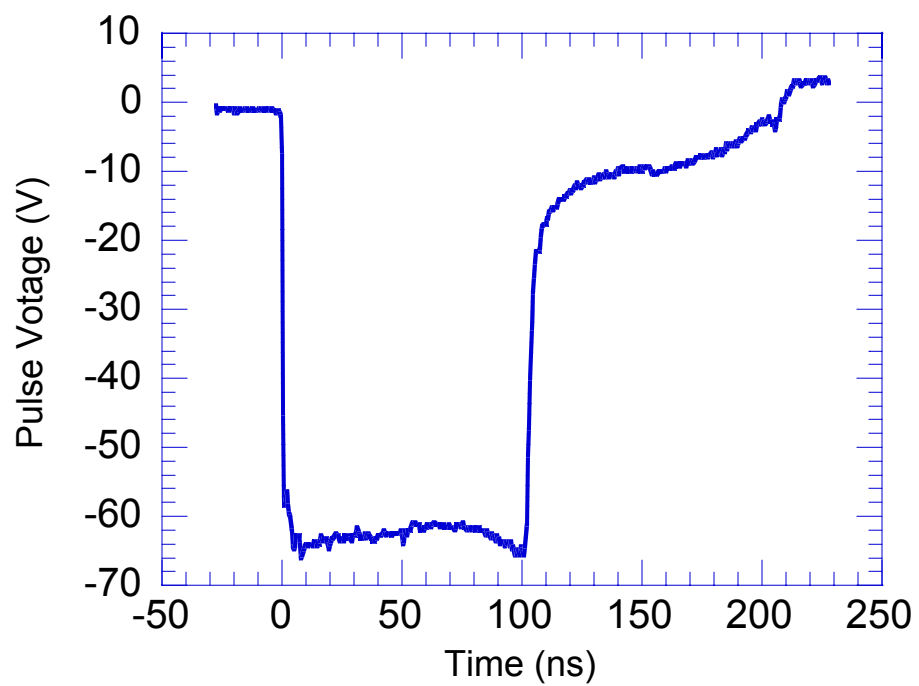
Figure 4.5. Typical grid-cathode pulser signal.

4.2.2 Energy Analyzer

The energy analyzer is located in the diagnostic chamber after the solenoid. Its structure and power supply circuit have been described in great detail in 3.2.

4.2.3 Automated Data Acquisition and Processing System

Another important part in Figure 4.1 is the automated measurement system including a high-voltage power supply, a Tektronix oscilloscope (TEK DSA 601A) and a computer. The high-voltage power supply used to retard the beam is Bertan 205B, which has low noise and high resolution, with maximum output voltage of 10 kV. The output high voltage of the power supply can be controlled locally via a precision front panel or can be remotely programmed by a 16-bit digital signal. A battery provides the voltage on the focusing cylinder of the energy analyzer, which is in series with the high-voltage output from the power supply. The energy analyzer output current signal is sent to the oscilloscope directly.

To improve the experimental efficiency and resolution, we developed a computer-controlled automated data-acquisition system. The entire control program is written in C language for high efficiency and low-level controllability. The power supply is remotely controlled with a TTL-compatible digital signal and the oscilloscope is through a GPIB interface. By automatically controlling the retarding voltage and the oscilloscope, this system can take the energy analyzer data with very fine steps. The smallest step to change the retarding voltage is 0.16 V on top of several kilovolts. A full set of data can be taken within several minutes, which is impossible with manual control as we did before. The interface of the data-acquisition software is shown in Figure 4.6. We can set the scanning retarding voltage region and voltage step,

selecting signal channel from the oscilloscope, setting filter on/off, average number, etc.

The data taken by the computer are then automatically processed by a MATLAB code, which can analyze the data and display detailed information about the beam energy spread within a couple of seconds. The data-processing software can provide time-resolved root-mean-square (rms) energy spread, full width at half maximum (FWHM), peak, and mean energy along the beam pulse. The interface of the data-processing software is shown in Figure 4.7. This software can show us the energy spectrum information in every interested interval along the 100 ns beam bunch. To eliminate the noise effect in the measurement, we can adjust the spectrum threshold. We can also set up interested retarding voltage regions. The range of the retarding voltage is generally 6 times wider than the rms energy spread.

The whole automated system decreases the time needed to conduct an experiment by more than a factor of 10, and most importantly, the quality of the data is much superior than if taken manually.
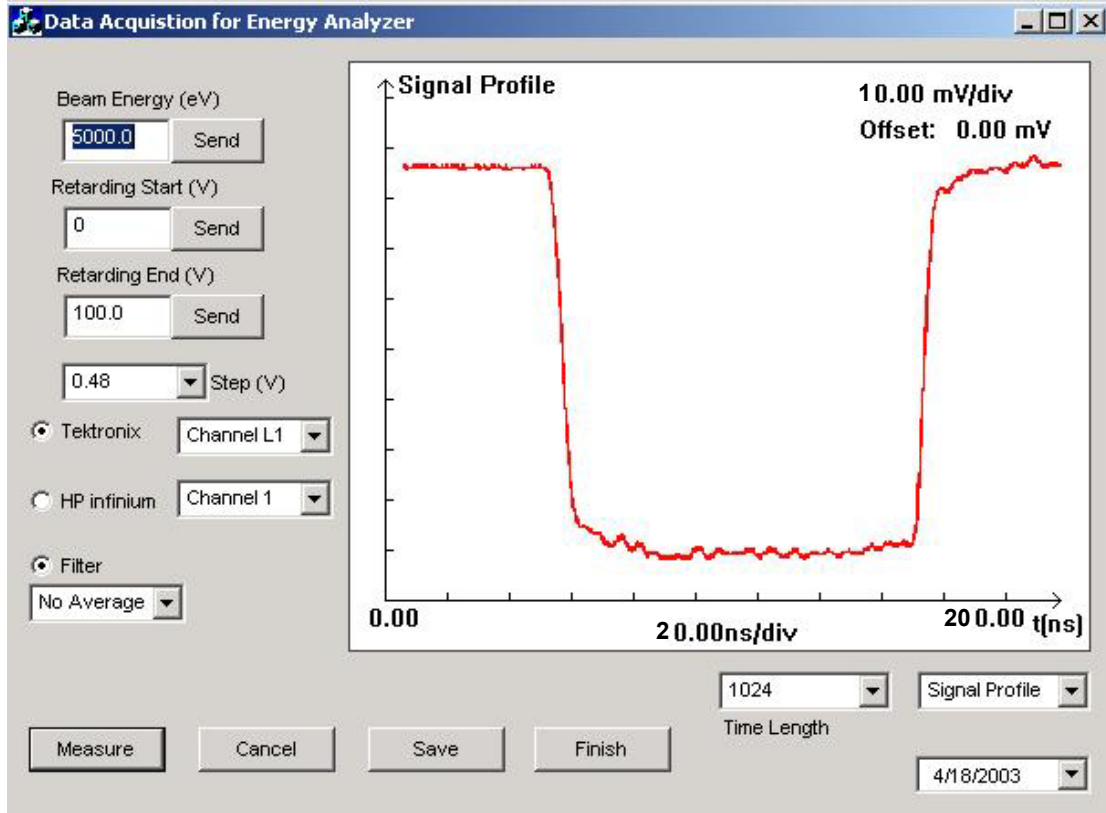
Figure 4.6. Interface of data-acquisition software for the energy analyzer test.
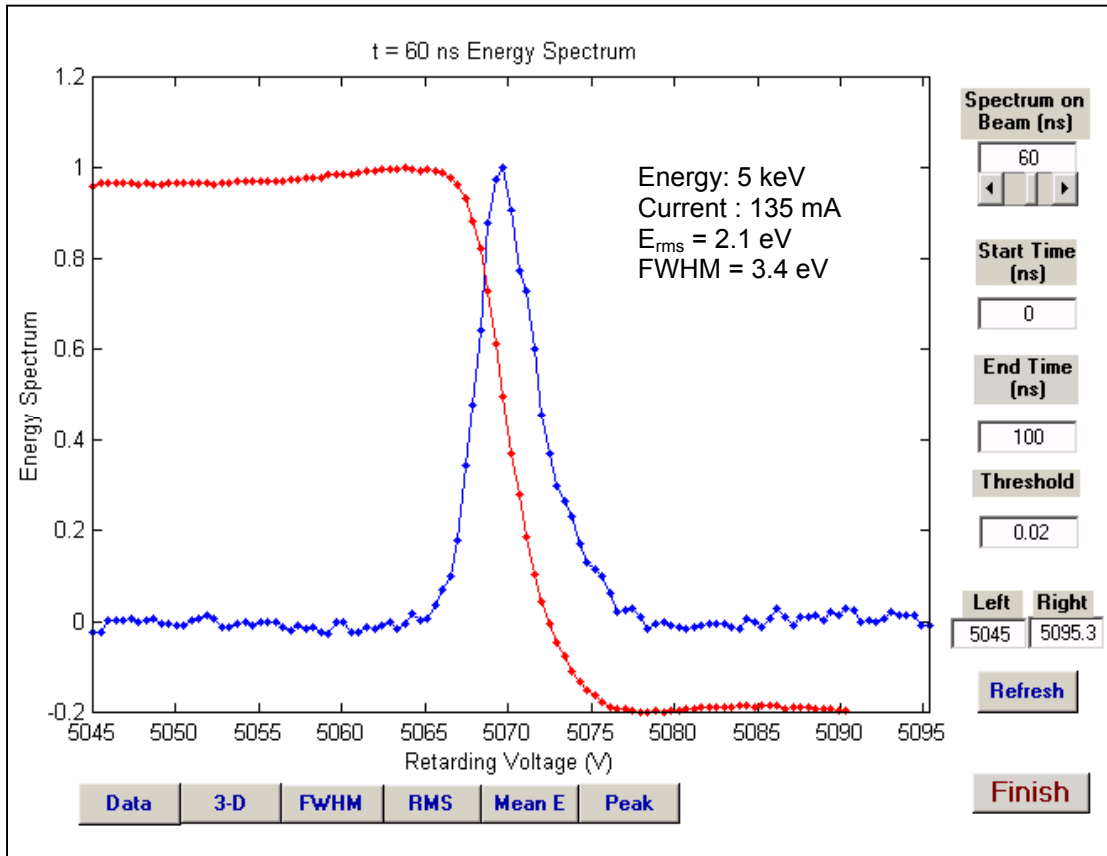
Figure 4.7. Interface of data-processing software for the energy analyzer test.

4.2.4 EMI interference in the measurement

The measurement often meets the problem of the electrical magnetic interference (EMI). Any high frequency interference and radiation from outside will destroy the high-resolution measurements. We were puzzled by the noises in the measurement signals. The noise sometime was about 10 mV, about the same level of the signal amplitude. We found this noise mostly comes from the cross-talk from the electron gun trigger interference. The original design of the measurement system used the same high-voltage power supply to provide acceleration voltage for the electron gun and retarding voltage for the energy analyzer at the same time. Any high frequency interference in the electron gun will go to the energy analyzer through the high-voltage cable. To cut off the interference path to the energy analyzer, we use a different power supply to provide retarding voltage for the energy analyzer. We also use low pass filter to remove any high frequency interference from the high-voltage inputs to the analyzer. The accessories for the analyzer are well shielded by the copper mesh and are also well-grounded. By doing this, we can reduce the noise to less than 1 mV, which is satisfactory for our measurement requirements.

4.3 Experimental Results and Analysis

4.3.1 Beam Envelopes at Different Solenoidal Focusing Strengths

In the experiment, the nominal beam energy is 5 keV and the beam current is 135 mA, with pulse width of 100 ns and rise time of 2 ns, as measured by the Bergoz coil shown in Figure 4.8. The initial beam size and its derivative at the aperture of the electron gun are r_i= 5 mm and r_i'=0.03, respectively. The normalized effective emittance ε_n is 10 μm [30]. Figure 4.9 shows the beam envelope from the electron gun to the energy analyzer for three different focusing strengths of the solenoid. The distance of the solenoid to the aperture of the gun is 11 cm. For a focusing strength of 104 Gauss, the beam envelope is shown with a solid blue line and the blue dots are the beam size from experimental measurement. At this focusing strength, the energy analyzer can get the maximum signal because it is at the beam waist. Figure 4.10 is a typical output pulse signal from the energy analyzer when the energy analyzer is at the position of the beam waist. The signal amplitude is about 120 mV with a rise time of 5 ns and the noise is about ±1 mV. Noise effects can be reduced after averaging samples. From Figure 4.10, we can see that this energy analyzer has a good response, and records the beam signal faithfully compared with the beam current signal from Figure 4.8. But in the experiment, in order to reduce the longitudinal space-charge effect inside the device, we need to limit the signal magnitude to about 10 mV [31]. We can control the solenoidal focusing strength, and therefore the position of the beam waist, to let the lower current beamlet enter the energy analyzer. In Figure 4.9,

the black solid line is for the beam envelope with a weak focusing of 85 Gauss and the red line for a strong focusing of 120 Gauss (the red crosses are the beam size measured from experiment).
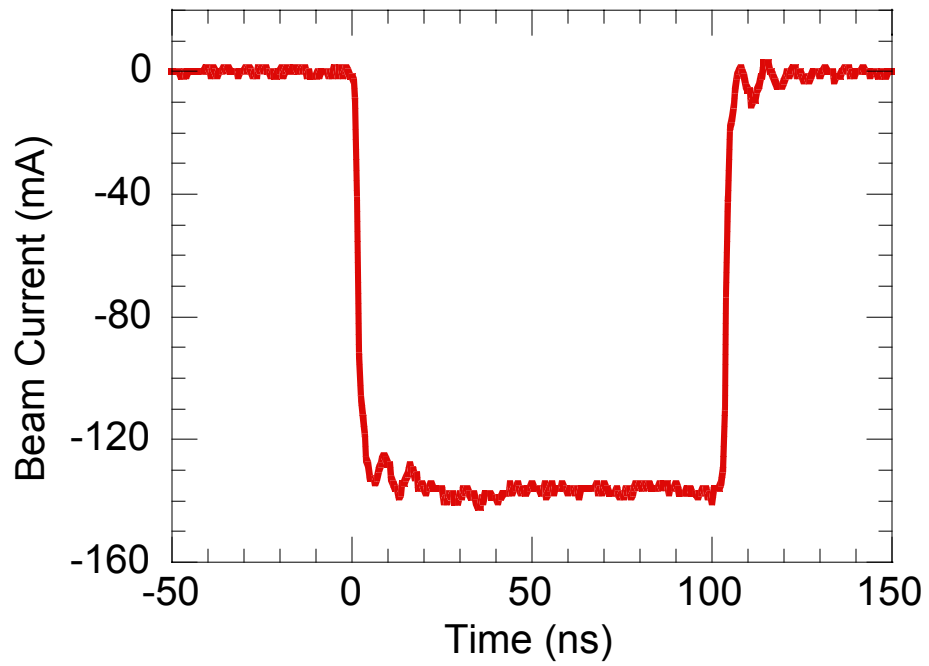
Figure 4.8. Beam Current signal measured by Bergoz coil
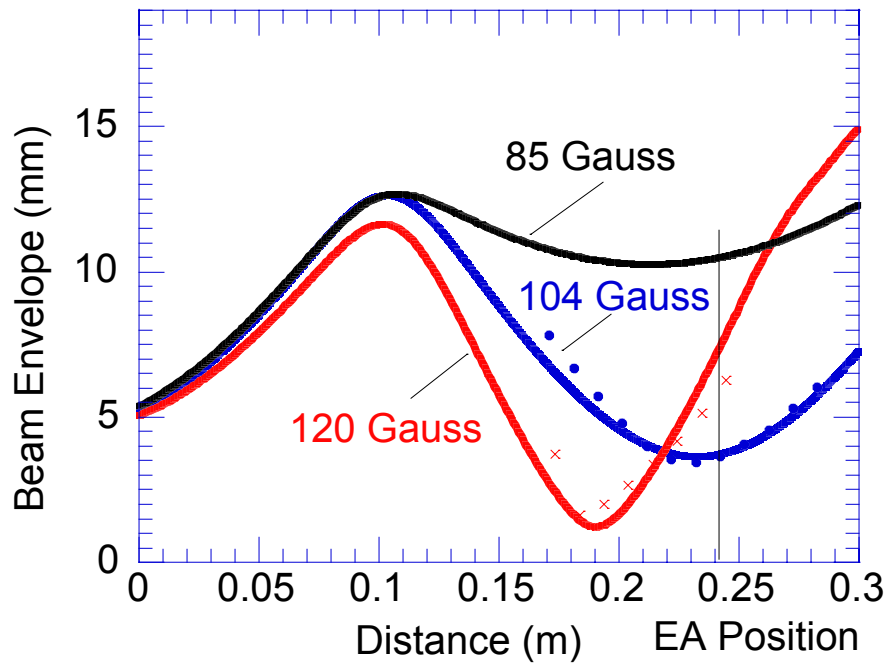
Figure 4.9. Beam envelopes from electron gun to energy analyzer at different focusing strengths of the solenoid.
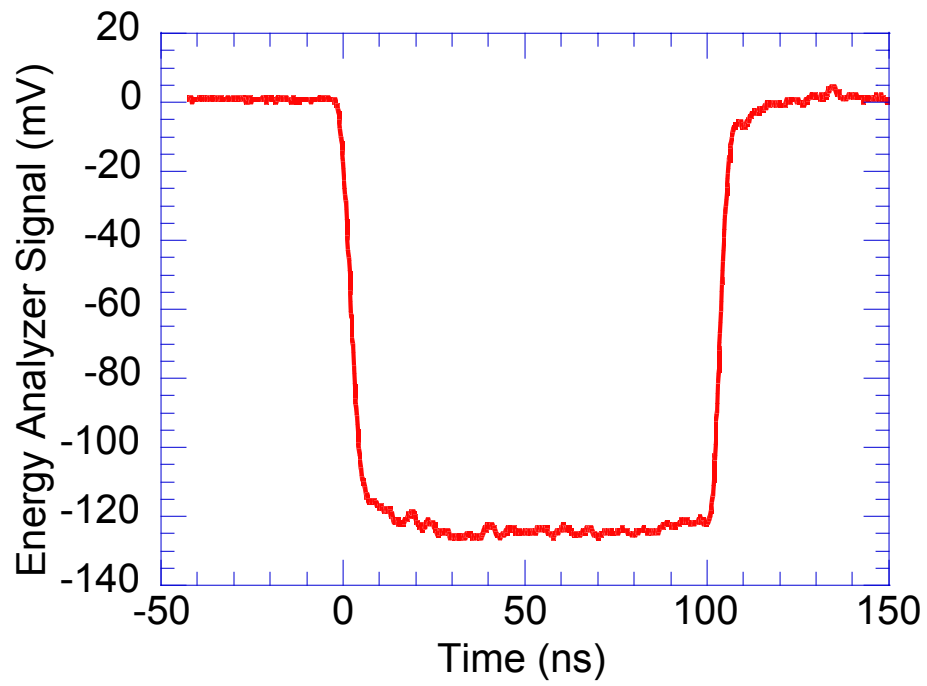
Figure 4.10. Typical energy analyzer output signal at the waist of the beam.

4.3.2 Beam Energy Spectrum Measurement

During the experiment, the focusing voltage inside the energy analyzer is set to 120 V relative to the retarding voltage to optimize the device resolution. The retarding voltage is changed by a step size of 0.5 V, which is adequate for the experiment. For a given retarding voltage, 16 current pulses are sampled and averaged to improve the signal-to-noise ratio. In Figure 4.11, different signal profiles corresponding to different retarding voltages are plotted together when a weak focusing strength is used (the value of the retarding voltage is referenced to the lab ground). In the figure, we can see that the collector signal decreases with increasing retarding voltage. There are two things in the figure worth noting. First, we can see that the signal at the beam head tends to be larger than in the rest of the beam. This is either due to high-energy particles in the head or the time-varying space-charge effect in the device. Second, there are oscillations in the waveform that increase as the retarding voltage increases. This might be due to a virtual cathode oscillation inside the energy analyzer. The exact mechanisms of these transient behaviors (within a couple of nanoseconds) inside the device are not well understood and need to be studied in more detail in the future. At this stage, we are focusing on the beam energy measurement at longer temporal scale (~ 10 ns).

By differentiating the energy analyzer output with respect to the retarding voltage, we can get the beam energy profile for the whole beam. Figure 4.12 shows such an energy spectrum with rms energy spread of 2.2 eV, FWHM of 3.9 eV, mean energy of 5070.5 eV, and spectrum peak of 5069.7 eV. The sampling point is taken at the middle of the beam pulse.
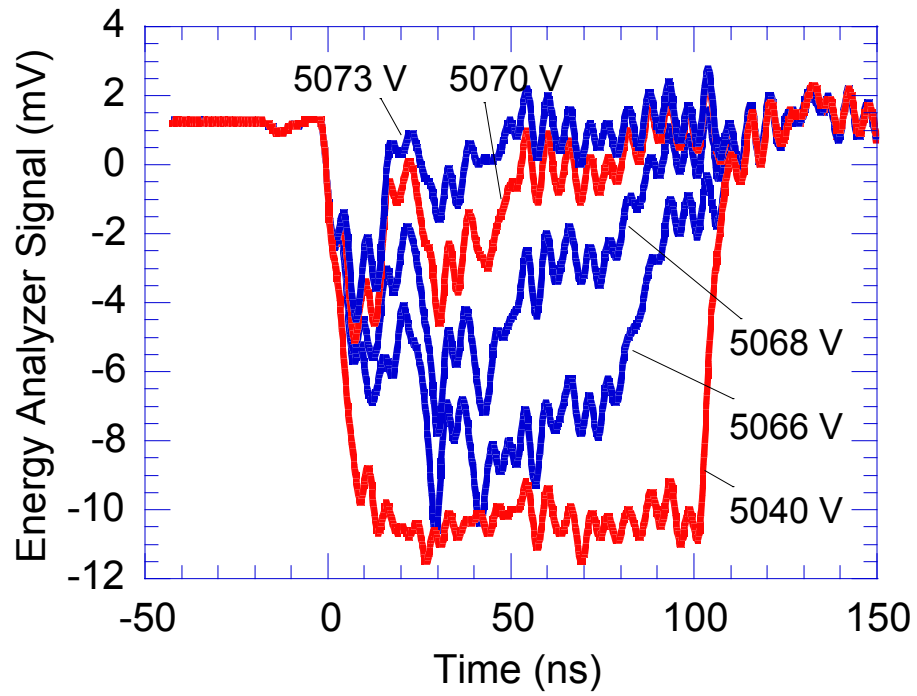
Figure 4.11. Energy analyzer outputs at the different magnitudes of the

retarding voltages.
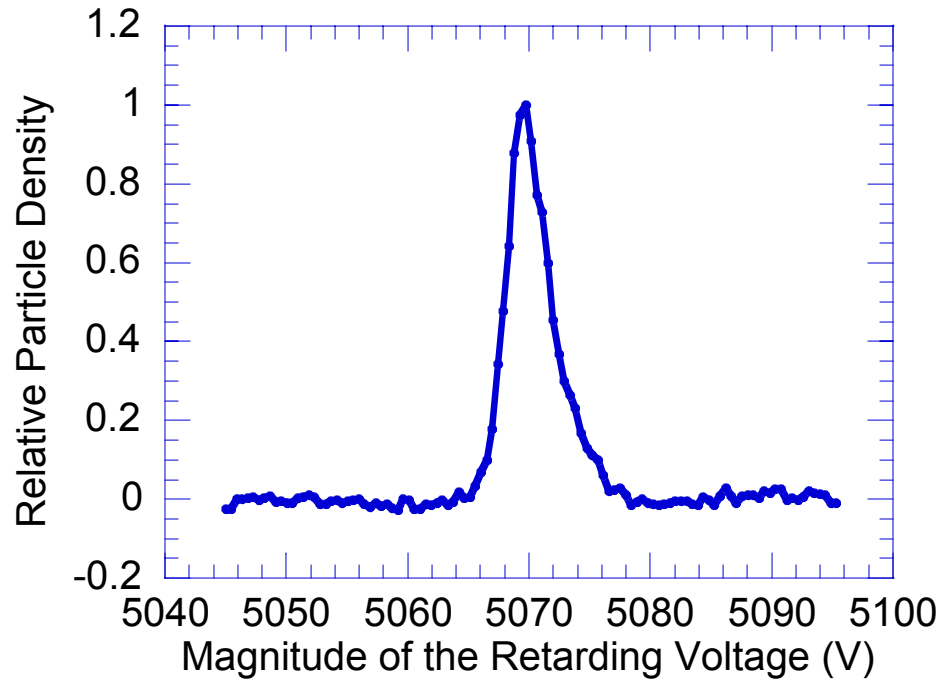
Figure 4.12. Energy spectrum for a beam with energy of 5 keV and current of

135 mA. The rms energy spread is 2.2 eV, FWHM is 3.9 eV and mean energy is

5070.5 eV.

As we said, the energy spectrum is time resolved. Figure 4.13 shows the measured mean energy as a function of time along the beam pulse. The measured mean energy of the main beam is about 5070 eV. The absolute value of the measured energy is about 50 eV higher than the assumed beam energy from the gun. It is believed that this DC energy shift is due to field leakage through the retarding mesh inside the energy analyzer. From the figure, we can see that the head of the beam has a higher mean energy, up to 5200 eV, and the tail of the beam has a lower energy, down to 4940 eV. The length of the head and tail is about 5 ns each. This energy difference at the head and tail is due to the unbalanced collective space-charge force. Beam edge expansion of an initially rectangular bunch beam has been studied in Ref. [32, 33, 34]. According to the calculation, for a 5 keV, 135 mA beam with average radius 7 mm, when the beam is 25 cm away from the cathode, the front edge is ~1500 eV higher than the beam energy with a rise time of ~1 ns and the rear edge is ~1500 eV lower than the beam energy with the same drop time for an ideal rectangular pulse employed on the cathode. The theoretical calculation is based on an ideal rectangular beam, but actual beams have finite rise time. In our experiment, the rise time of the pulse signal employed on the cathode in the gridded gun is measured to be around ~2 ns. The system bandwidth of the measurement instruments such as the energy analyzer and the scope also impose a limit on the measurable rise time. In this measurement, we believe the 5 ns length of the measured beam head/tail is mainly due to the limited system bandwidth. Although the rise time and drop time caused by beam expansion is shadowed by the limited system bandwidth, the energy differences still can be seen in the rise and drop time. It is noticed that the measured beam energy

at the head is 130 eV higher than the main beam, while the theory predicts about 1500 eV higher. The reason is that the number of particles which have the highest energy, is very small in the beam head. It is difficult in the experiment to capture these particles due to the limited signal resolution in the device. Nevertheless, it is the first time that we clearly observed the temporal mean energy information including the head and tail along the beam pulse in the experiment. We plan to do more experiments to improve our results.

Figure 4.14 shows the measured energy spread as a function of time along the aforementioned beam. It is clear that there is higher energy spread at the beam head. The energy spread decreases from ~12 eV at the head to ~ 2.2 eV at the main beam, then goes up at the tail of the beam. The wiggle in the head of the beam may be caused by virtual cathode oscillation with a period of ~ 5 ns. The exact cause of the large energy spread at the head is not clear and more theoretical analysis is needed to understand it.
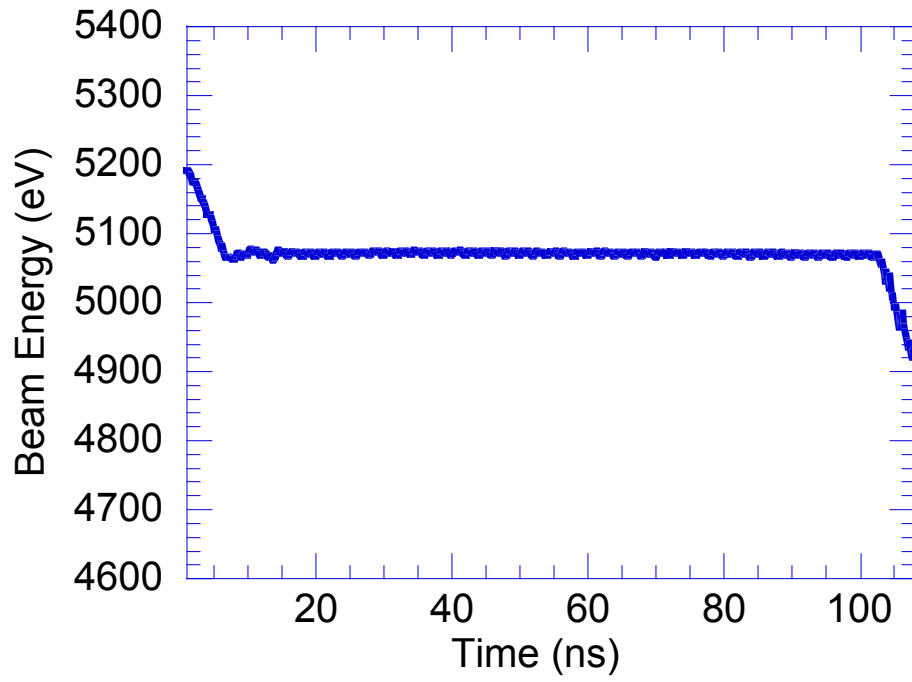
Figure 4.13. Mean energy along the beam pulse for a beam with energy of 5

keV.
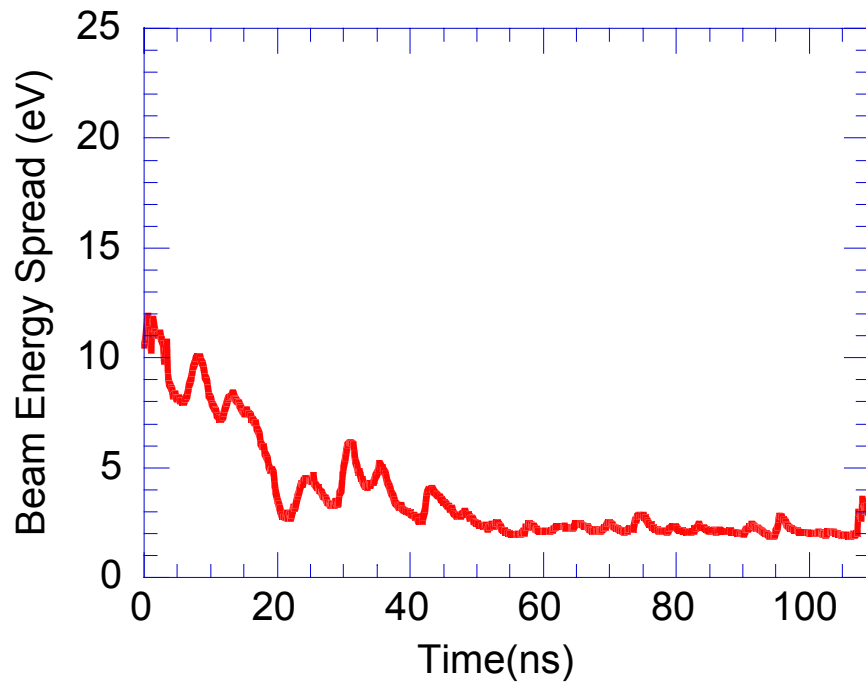
Figure 4.14. Beam Energy Spread Along Beam Pulse for a beam with energy of 5 keV and current of 135 mA. Average energy spread of the main beam is 2.2 eV.

4.3.3 Longitudinal Space-Charge Effect inside the Device

During the study of the retarding field energy analyzer, we found that longitudinal space-charge effects play a significant role in the performance of the device. Ref. [31] gives a theoretical analysis of the longitudinal effect in the analyzer. According to the theory, if the current density inside the device is higher than a critical value, the longitudinal space-charge effect and the formation of a potential minimum similar to the virtual cathode formation in an electron gun will distort the measured energy spectrum. The measured mean energy will be shifted toward the low-energy side and therefore leave a tail at the high-energy side. The resulting rms energy spread and FWHM might also be affected. Figure 4.15 shows such an experimental observation, where the beam energy spectra are measured at two different injected currents inside the device, 0.2 mA and 2.2 mA, forming 10 mV and 110 mV output signals, respectively. The magnitude of the focusing voltage is 120 V larger than the retarding voltage in this experiment. The measured beam energy spreads are 2.2 eV and 3.2 eV for curves I and curve II, respectively. We can see that curve I almost has no high-energy tails and the measured spectrum is close to a Gaussian distribution. For a higher injected beam current, we can see that the energy spectrum is downshifted and the high-energy tail is visible. If we continue to reduce the injected current below 0.2 mA, the energy spectrum does not change compared to the curve I, which indicates that below 0.2 mA, the space-charge effect does not play a role. So in our experiment, we always try to set the injected current below 0.2 mA to avoid the longitudinal space-charge effect. The measured energy spread in curve I is closer to the real energy spread of the beam.
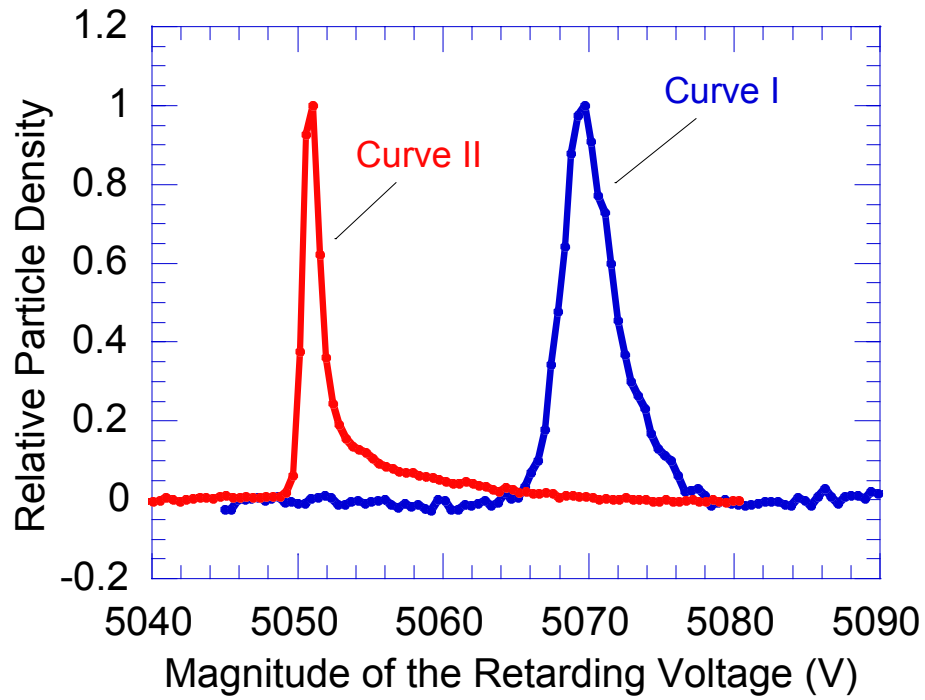
Figure 4.15. Experimental results of beam energy spread for two different injected currents inside the device. Curve I for current of 0.2 mA, rms energy spread of 2.2 eV, FWHM of 3.9 eV. Curve II for current of 2.2 mA, rms energy spread of 3.2 eV, FWHM of 1.5 eV.

4.3.4 Energy Spectrum vs. Focusing Voltage

Variable focusing voltage has the advantage of getting the optimum focusing force to balance the beam expansion due to the space-charge force and other factors inside the energy analyzer. If the focusing force is too weak, it cannot compensate for the defocusing force, and the beam will expand too much, causing poor measurement resolution. However, if the focusing force is too strong, the beam will be overfocused and also cause poor resolution. In our experiment, when the beam input current is fixed, the beam energy spread is measured at different relative focusing voltages. We found that the relative focusing voltage has a relatively wide operating region. Figure 4.16 shows the relation of rms energy spread versus relative focusing voltage of the energy analyzer for a 5 keV, 135 mA beam. The measured rms energy spread stays at 2.2 eV when the relative focusing voltage is between 90 V to 150 V. We choose the relative focusing voltage at the middle point, 120 V. The required focusing voltage value from the experiment is larger by 55 V than that predicted by the SIMION simulation. This is not surprising because SIMION does not consider the space-charge effects. However, this experimental optimum point is in better agreement with the envelope analysis, as can bee seen if one compares Figures 4.16 and Figure 3.9. In Figure 3.9, the theoretical analysis indicates that the analyzer has better resolution (less than 0.1 eV errors) with the relative focusing voltage, ranging from 100 V to 160 V. This result is reflected in Figure 4.16, which shows that, in the experiment, the device can resolve a smaller energy spread within the similar range of the relative focusing voltage.
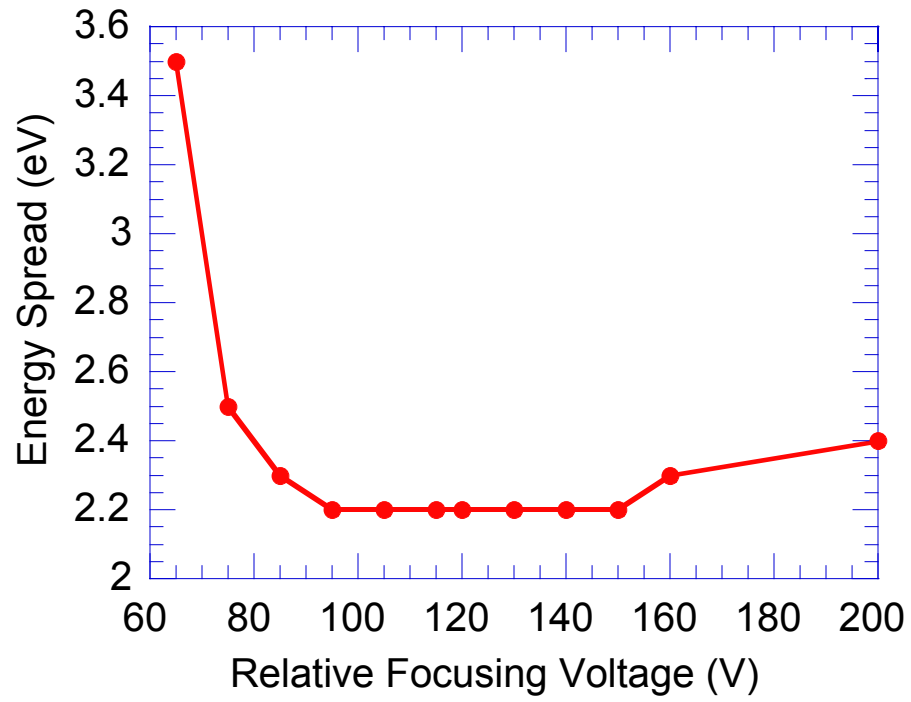
Figure 4.16. Experimental results of beam rms energy spread at different relative focusing voltages when injected current inside the device is 0.2 mA.

In the experiment, we also found that when the beam input current is fixed, the beam mean energy is shifted at different relative focusing voltages. Figure 4.17 shows the relation of mean energy vs. relative focusing voltage of the energy analyzer for a 5 keV, 135 mA beam. The mean energy of measurement is shifted 37 V from 5075 V to 5038 V when the relative focusing voltage magnitude increases from 100 V to 200 V. This experimental result just agrees with our envelope simulation results that the beam retarding point inside the energy analyzer is shifted for different relative focusing voltages. This is shown in Figure 3.10, in which relative voltage of the retarding point drops from 0 V to about - 47 V. It proves that as the magnitudes of the focusing voltage increase, the magnitude and the position of the minimum potential points also change. Beam particles are retarded at the retarding point, not at the retarding mesh. The mean energy shifting still has 10 V difference between the theory calculation (47 V) and the experiment (37 V). It is believe to be caused by the voltage leak on the mesh hole in the energy analyzer. When the focusing voltage amplitude is 120 V, the mean energy shift is about −5 V from the experiment and −6 V from the theoretical calculation.
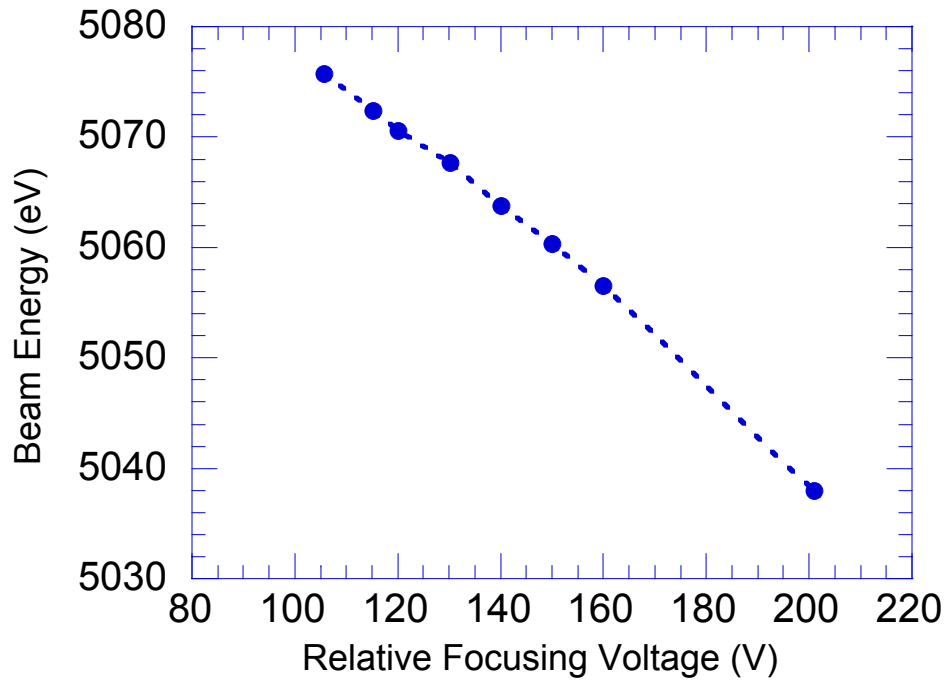
Figure 4.17. Experimental results of beam mean energy at different relative

focusing voltages when injected current inside the device is 0.2 mA.

4.3.5 Error Analysis of Energy Spread

The coherent envelope motion due to the beam expansion is the main error source in the experiment if we use an improper focusing voltage. Of course, there exist other error sources. The first one is due to the device misalignment. But according to the SIMION simulation, when the incident angle of the particle is smaller than 1°, the rms error is only 0.05 eV (we listed the maximum error of 0.25 eV for a 5 keV beam in Table 3.1). In our experiment, the misalignment of the beam angle can be made smaller than 0.2 degree, which is good enough to be corrected by the focusing cylinder. Another possible error source is the fluctuation in the power supplies for the electron gun and the analyzer, which is about 0.1 V according to the manufacturer's specification. This error can be reduced to about 0.03 eV by taking the average of 16 beam signals. These errors, along with others, such as those caused by the background noise, data processing, etc, account for less than 0.2 eV to the measurement. From the above analysis, when the proper focusing voltage is used, the resolution of this analyzer is less than 0.2 eV for a 5 keV beam, which is significantly better than that of any comparable devices.

4.3.6 Experimental Energy Spread Results Compared with the Theories

It is very interesting to compare the measured energy spread with theoretical prediction considering the longitudinal-longitudinal effect and the Boersch effect [1,16]. The theory of the beam energy spread evolution has been reviewed in Chapter 2. The longitudinal-longitudinal effect is dominant in the initial acceleration. The energy spread due to the Boersch effect increases monotonically and at the distance of 25 cm to the emitter, the energy spread due to the longitudinal-longitudinal

relaxation is comparable to that due to the Boersch effect. In our experiment, the beam energy is 5 keV and the beam current is 135 mA. Current density of the beam can be varied by changing the focusing strength of the solenoid. When we use weak focusing, as shown in Figure 4.9 in the black line, the measured energy spread is ~2.2 eV, which is very close to theoretical prediction, ~2.0 eV. However, when we use strong focusing as shown in Figure 4.9 in the red line and get high current density, the measured energy spread increases to ~2.5 eV, also very close to theoretical prediction, ~2.6 eV. We also measured the energy spreads with beam energies of 3 keV and 4 keV. Beam current is 70 mA for the 3 keV beam and 100 mA for the 4 keV beam. Figure 4.18 shows the measured energy spread compared with the theoretical prediction for different beam energies for both weak and strong focusing of the beam. Triangles with solid line are the theoretical values for weak focusing. Diamonds with dotted line are the theoretical values for strong focusing. Circles are the measured energy spreads for weak focusing and squares are for strong focusing. Error bars added on the measured energy spread are determined by the error analysis above. The differences between the experimental energy spreads and the theoretical predictions are listed in Table 4.1. The maximum difference is only 0.2 eV. The relative voltages on the focusing cylinder in the energy analyzer are also listed in the Table.

Beam		3 keV, 70 mA	4keV, 100 mA	5keV, 135 mA
Relative Focusing Voltage		50 V	80 V	120 V
Experimental Energy Spread	Weak Focusing	1.6 eV	1.9 eV	2.2 eV
	Strong Focusing	1.9 eV	2.2 eV	2.5 eV
Theoretical Energy Spread	Weak Focusing	1.5 eV	1.8 eV	2.0 eV
	Strong Focusing	1.8 eV	2.2 eV	2.6 eV
Difference between the experiment and the theory	Weak Focusing	0.1 eV	0.1 eV	0.2 eV
	Strong Focusing	0.1 eV	0	0.1 eV

Table 4.1. Experimental energy spreads compared with the theoretical predictions.
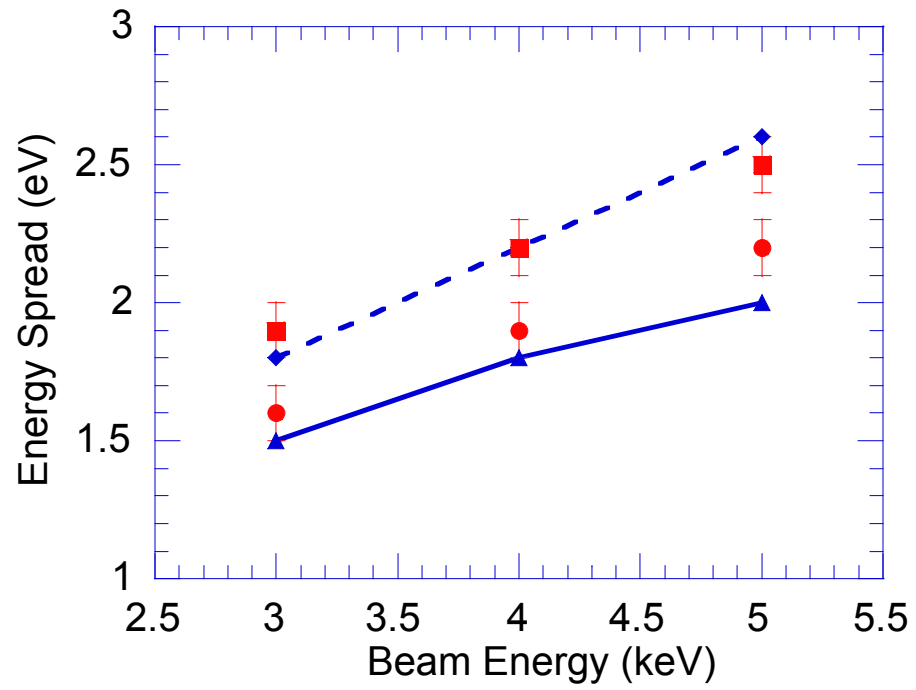
Figure 4.18. Measured beam energy spreads are compared with the theoretical

predictions for different beam energies

4.4 Derivation of Input Impedance of the Electron Gun

Due to the high resolution of the energy analyzer, we are able to infer the input impedance of the gridded thermionic electron gun based on the beam mean energy measurement. The input impedance of the cathode is very important for electron gun performance. The triode electron gun consists of cathode, grid, and anode [28]. A basic electronic circuit of the triode electron gun is shown in Figure 4.19. The gun electronics consist of a high-voltage supply between the anode and the grid, a DC cathode-grid bias voltage V_B (+30 V) to suppress the beam during idle period, and a pulse circuit to provide a ~100 ns pulse signal delivered to the cathode by a transmission line with the characteristic impedance Z_0 of 50 Ohms. The amplitude of the pulser source is $-2V_p$. The source impedance R_s of the pulser is 50 Ohms. There is a 50-Ohm resistor R at the output of the pulser circuit (between A and B) to match the impedance of the other circuits. The output voltage of the pulser (between A and B) is $-V_p$ (-60 V) in the match condition. All the electronics are located in a high-voltage deck, which is isolated from ground and charged to $-V_H$. The cathode is biased by a positive DC voltage relative to the grid to cut off the beam current. During emission, the pulse generator produces a negative pulse on the cathode to turn on the beam. The effect due to the magnetic field generated by the cathode heating current is minimized because the beam is emitted at the moment the ac heater current (60 Hz) crosses zero. A delay generator is employed to provide this synchronization.

In the experiment, when we change the cathode-grid bias voltage, both beam current and beam energy will change. Figure 4.20 shows the measured beam current

80

vs. the cathode-grid bias voltage when the grid high voltage V_H is fixed at 5 kV.

When the cathode-grid bias voltage is in the region of 0-30 V, the beam current is

space-charge limited and is almost a constant. When the bias voltage is larger than 30

V, the beam current reduces dramatically. The beam energy is determined by two

accelerating voltages: the high voltage $-V_H$ between the grid and the anode and the

voltage $-V_{CG}$ between the cathode and the grid. We found that when we reduce the

bias voltage from 30 V to 20 V, the mean energy measured by the energy analyzer

does not increase by 10 eV, but only by 5.8 eV. This, we believe, is caused by the

impedance mismatch between the electronic circuit and the electron gun. Figure 4.19

(b) is a simplified equivalent circuit between the cathode and the grid of the gun. The

pulser circuit between the points A and B is equivalent to a pulser source with

amplitude of $-V_p$ ($-60V$) in series with a resistance R_s in parallel with R, which is

$R/2$. The equivalent impedance of the beam load between the cathode and grid is

represented as R_{beam}, which only exists during beam emission.

　As shown in Figure 4.19 (b), when triggered, the voltage between cathode and

grid is

$$-V_{CG} = \frac{R_{beam}}{R_{beam} + R/2}(-V_p + V_B). \qquad (5.1)$$

$-V_{CG}$ is the actual accelerating voltage between the cathode and the grid. After

passing the grid, electrons are then accelerated by the high voltage $-V_H$, which does

not change with the grid voltage. Figure 4.21 shows the mean energy of the beam at

the different bias voltages. The solid line is a linear fitting to the experimental data,

81
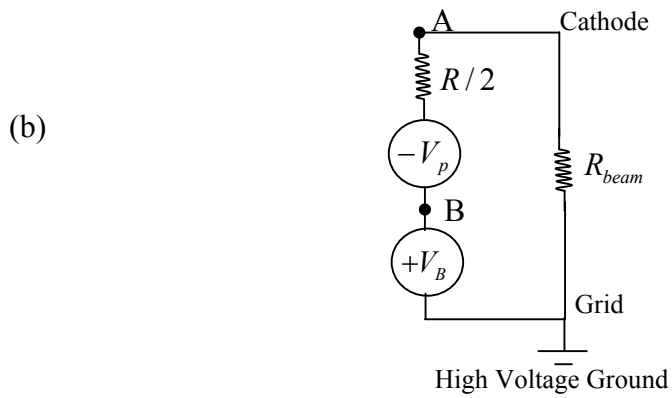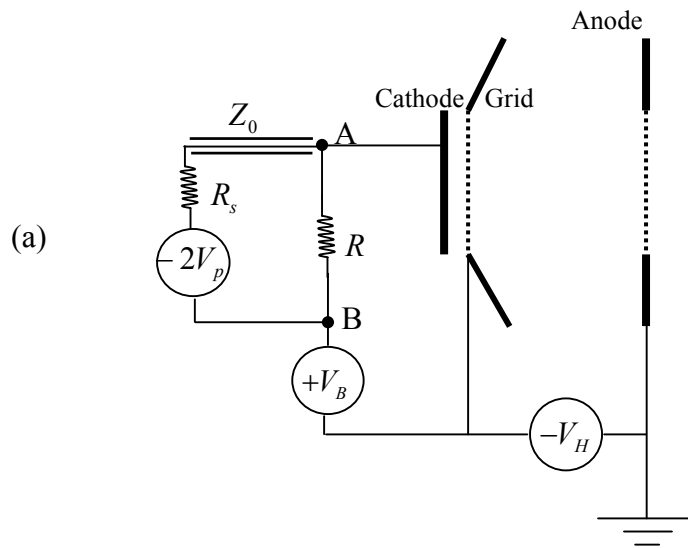
Figure 4.19. Basic electronic circuit of the triode electron gun.
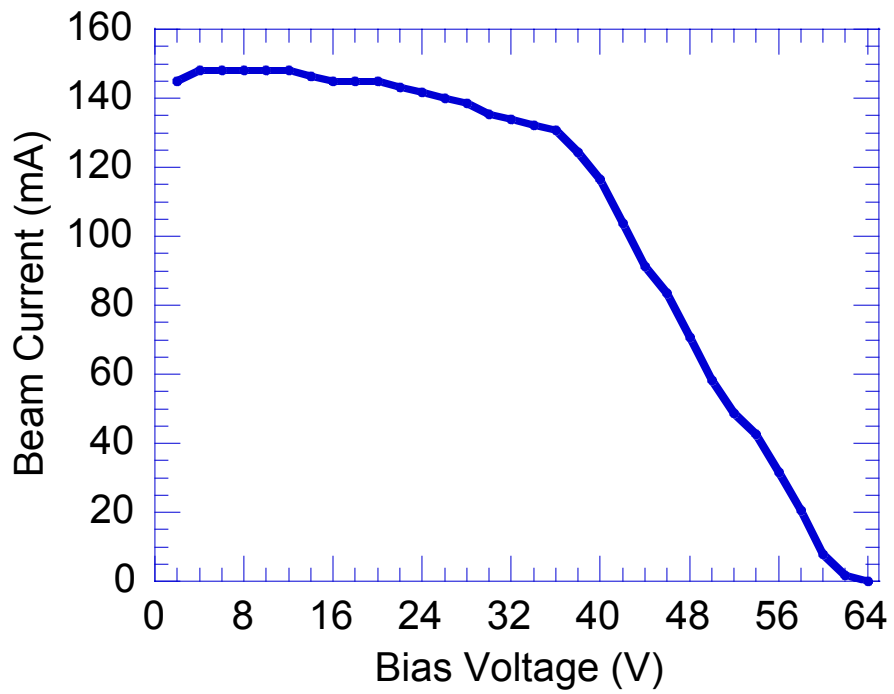
Figure 4.20. Beam current between grid and anode vs. bias voltage of the

electron gun.

which are shown as dots. From the linear fit curve, the beam mean energy E is related to the bias voltage by

$$E = -0.56 \times V_B + 5087. \qquad (5.2)$$

Through the linear extrapolation, we can see that when the bias voltage is 0, the beam energy is at 5087 eV, and when the bias voltage is equal to a pulse voltage of 60 V, the mean beam energy is at 5053 eV. From the information of the mean beam energy at different bias voltages, we can calculate the net voltage between the cathode and the grid as follows. When the bias voltage V_B equals the pulse voltage V_P, we know the cathode-grid voltage V_{CG} is zero according to Equation (5.1). When the bias voltage is at other values, the cathode-grid voltage can be calculated as

$$V_{CG}(V_B) = E(V_B) - E(V_B = 60V). \qquad (5.3)$$

The results of the calculation are shown in Figure 4.22. We can see when bias voltage changes from 0 V to 40 V, the amplitude of the voltage between the cathode and the grid reduces from 34 V to 11 V.

From Equation (5.1), we can get the beam impedance between the cathode and the grid

$$R_{beam} = \frac{V_{CG}}{2(V_P - V_B - V_{CG})} R. \qquad (5.4)$$

Here, R is the 50-Ohm matching resistor.

In the experiments, V_P is fixed at 60 V, V_{CG} and V_B are both known from Figure 4.22. So when we change the grid bias voltage V_B in the gun's saturation region, we can calculate the beam impedance at different voltages, the result of which is shown by the dots in Figure 4.23. It is interesting that the beam impedance is about 30 Ohms

and therefore the V-I characteristic between the cathode and the grid is linear in the gun's saturation region. Triode gun behavior working in the saturation region is very complicated, and there are currently no accurate mathematical models to describe the current and voltage relation in this region. The energy analyzer provides one indirect way to measure the beam impedance on the cathode.
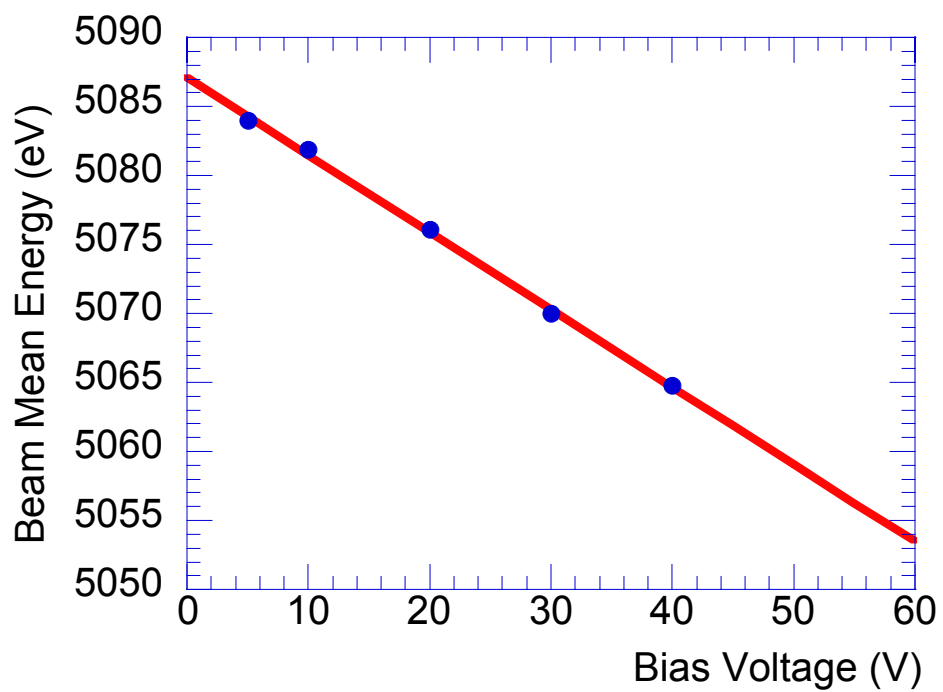
Figure 4.21. Mean energy at different bias voltages (solid line is the fitting

line using experimental data shown as dots).
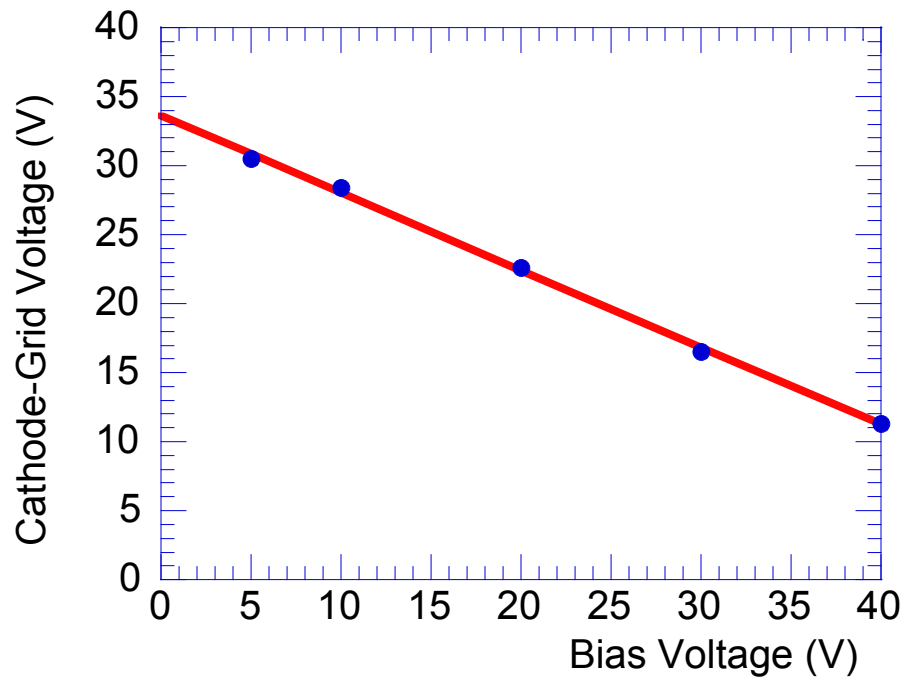
Figure 4.22. Voltage amplitude between the cathode and the grid at different

bias voltages (solid line is the fitting line using experimental data shown as dots).
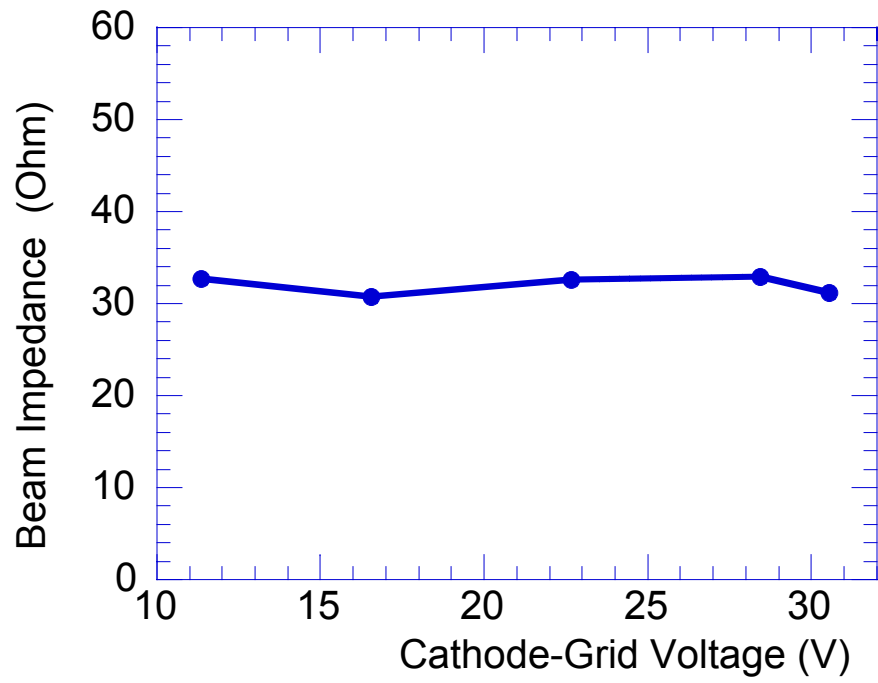
Figure 4.23. Beam impedance vs. the voltage between the cathode and the grid.

Chapter 5 : Measurement of Energy Spread Evolution in a Long Uniform Focusing Channel

5.1 Introduction

According to the theoretical predictions, the Boersch effect will be the dominant cause of longitudinal energy spread due to the intrabeam scattering after the beam has been transported over a long distance, and it will increase with distance. One way to study the initial relaxation process of the beam towards the equilibrium state (which would occur for our case hundreds of meters downstream) is to measure the beam energy spread at different transport distances. The energy spread of the electron beam was previously measured in a 5 m period solenoid transport channel at the University of Maryland Electron Beam Lab many years ago. Due to the limited energy analyzer resolution of about 40 eV, this energy relaxation could not be observed in that experiment. With the new high-resolution energy analyzer (10^{-4} resolution), it is now possible for us to measure the evolution of the energy spread due to this relaxation.

An experiment at the University of Maryland, has been set up to study the energy spread evolution along a 2.3 m transport line to measure the longitudinal energy spread evolution at two points. We already measured the beam energy spread at the distance of 25 cm from the electron gun as we did the energy analyzer testing, as discussed in the last chapter. The experimental results already have good agreement with the theoretical predictions. In this chapter, we report the experimental results at a second point, which is at a distance of 2.3 m from the electron gun. At lower current density, experimental results are in relatively good

agreement with theoretical predictions. However, we also observe some abnormal phenomena at higher beam current density.

5.2 Experimental Setup

5.2.1 System Description

Figure 5.1 shows the schematic of the long beam transport channel experiment. We used the same thermionic triode gun as we did in the experiment described in Chapter 4. One energy analyzer is located in the diagnostic chamber at the end of this transport channel. The distance from the energy analyzer to the anode of the gun is 2.3 m. The long solenoid, M4, with a total length of about 1.4 m, serves as a uniform focusing channel to transport the beam to the analyzer. The advantage of using a long solenoid is that the matched beam envelope in the solenoidal channel is a constant, which makes it easier for theoretical analysis. Before the long solenoid channel, three short solenoids, M1, M2, and M3, are employed for matching the beam into the long solenoid. A pair of steering dipoles is used in front of every solenoid to control the beam incident direction and position to the long solenoid. There are two current monitors in the matching section: one Bergoz coil current monitor, located between the first and the second solenoid, and one resistive current monitor, located between M3 and M4. After the long solenoid, there is another current monitor and a movable phosphor screen for the beam current measurement and imaging. In order to control the amount of current injected into the energy analyzer, a short solenoid, M5, is inserted between the exit of the long solenoid and the energy analyzer. The beam is uniformly focused in the long solenoid and the beam size inside it can be adjusted by changing the focusing strength of the long solenoid. The distances of the solenoids to

90

the anode of the electron gun are decided by the experimental design issues, including beam transport, mechanical sizes of the focusing lenses, and diagnostics (Table 5.1). The focusing strengths of the three short solenoids can be adjusted to match the beam into the long solenoid. Figure 5.2 shows the picture of the experimental setup.

Space of about 20 cm between the second and third solenoid is reserved for another diagnostic chamber to be installed. A new energy analyzer with the same structure as the one currently installed in the system and a phosphor screen will be installed in this chamber for the future study of the relation between longitudinal space-charge perturbations and energy spread in the beam.

Solenoid	M1	M2	M3	M4	M5
Solenoid Center to Aperture of gun	11 cm	27 cm	51.6 cm	133.5 cm	210 cm

Table 5.1. The distances of the solenoids to the anode of the gun.

Ion Pump

Ion Pump

M1 M2   M3   M4   M5

Bergoz Coil

Electron gun

Current Monitor

Energy Analyzer

Movable Phosphor
Screen
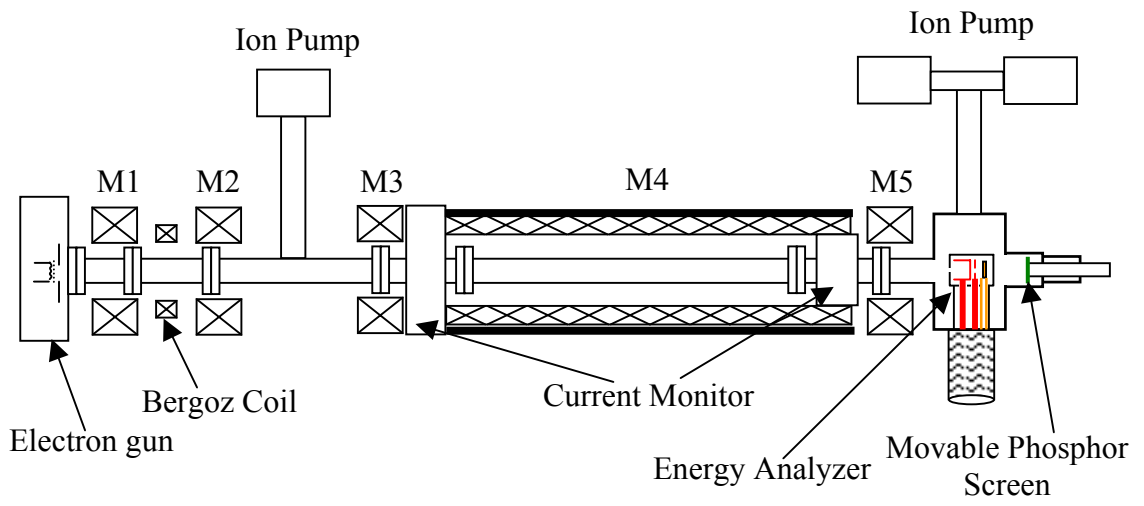
Figure 5.1. Schematic of the long transport line experiment
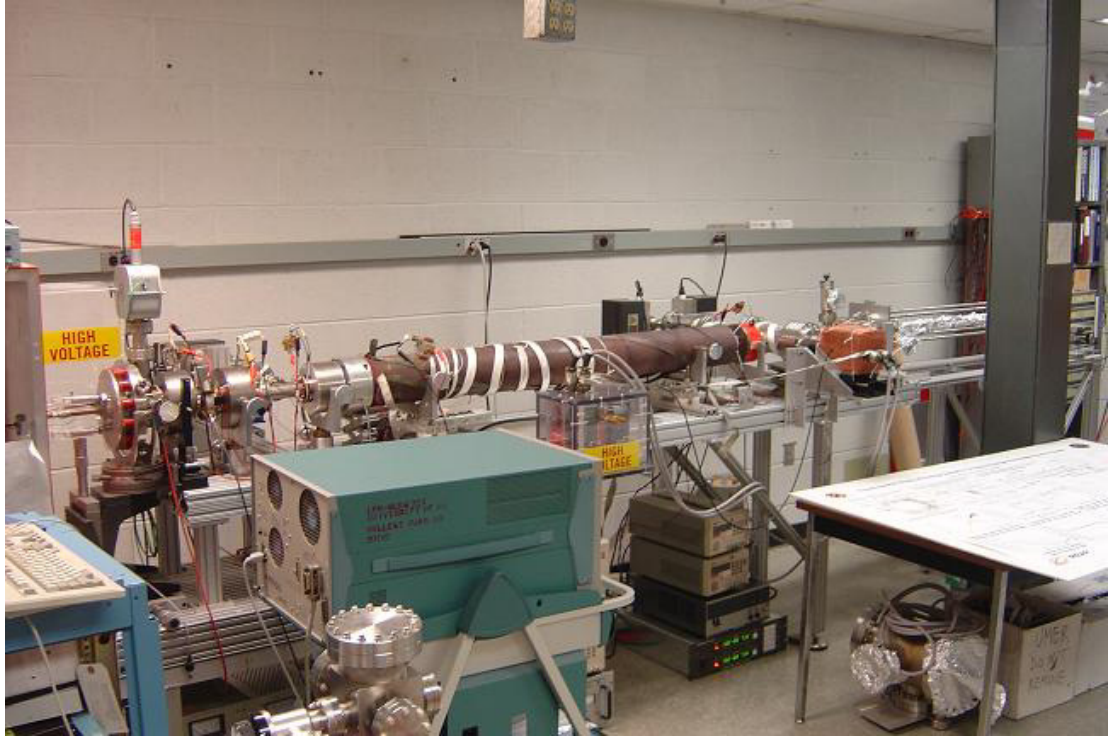
Figure 5.2. Photo of the long transport line experimental setup

5.2.2 Matching Lenses and Long Solenoid Transport

The short solenoids each have the same inner diameters of 7.6 cm. The current in each solenoid can be adjusted individually by different DC power supplies. All the solenoids were re-characterized for this experiment. The fields were measured by a Bell gaussmeter with a longitudinal Hall probe. Figures 5.3-5.7 show the measured axial magnetic field profiles along the z-axis and calibration lines of peak field B_0 versus current inside the solenoids. The circles represent measurement points. The fitting curves are also shown in the figure.

The fitted formula of the field profile for each of the four short solenoids, M1, M2, M3, and M5 is characterized by [35]

$$B_{z0}(z) = B_0 \exp(-\frac{(z-z_0)^2}{d^2}) * \left[\sec h(\frac{z-z_0}{b}) + c \sinh^2(\frac{z-z_0}{b}) \right]. \qquad (5.1)$$

Here, B_0 is the maximum axial magnetic field; z_0 is the center position of the solenoids; and b, c, and d are fitting parameters, and they are different for each solenoid. Table 5.2 shows the fitting parameters of the four short solenoids.

	M1	M2	M3	M5
b	3.4433	3.9366	5.689	4.2547
c	0.032	0.084	0.046	0.028
d	4.415	3.8872	7.2778	4.9058

Table 5.2. Fitting parameters of the four short solenoids

The long solenoid M4 is 138.7 cm long [8]. It is made of copper windings on an aluminum tube with a diameter of 11.5 cm. There is an iron tube on the outside of the

copper windings to restrict the field lines. The axial magnetic field is uniform inside the solenoid. However, at the edges, the fields decay with distance. Figure 5.6 shows the measured axial magnetic field profile along the z-axis and calibration line of peak B_0 versus current I. B_0 corresponds to the uniform field inside the solenoid, and depends on the current and the solenoid winding. The horizontal axis is the distance along the solenoid and the zero position is the physical edge of the solenoid. The fitted formula for the field profile is [8]

$$B_z(z) = B_0 c \left(\frac{z}{(z^2 + a^2)^{1/2}} - \frac{z - d}{((z-d)^2 + a^2)^2} \right) . \qquad (5.2)$$

Here, c, a, and d are empirical parameters for best fitting. Their numbers are c=0.5027, a=5.0408 cm, and d=137.08 cm respectively for this long solenoid. The uniform focusing plateau inside the long solenoid is about 120 cm, and the fringe-field regions on both sides of the plateau are about 30 cm each.

   Mathematically, the effective length l of each of these solenoids can be defined by (see Page 100 in Reference [1])

$$l = \frac{1}{B_0^2} \int_{-\infty}^{\infty} B_z^2(z) dz , \qquad (5.3)$$

where B_0 is the peak magnetic field. Table 5.3 shows the effective lengths of the four short solenoids and the long solenoid.

Solenoid #	M1	M2	M3	M4	M5
Effective Length (cm)	4.34	4.24	7.28	130.8	5.16

Table 5.3. Effective lengths of five solenoids

Short Solenoid M1 B-field
effective length=4.337 (I =5.7 A)

y = 101.85*(exp(-(m0^

	Value	
m1	4.415	
m2	3.4433	
m3	0.032197	(
Chisq	4.1119	
R	0.99998	
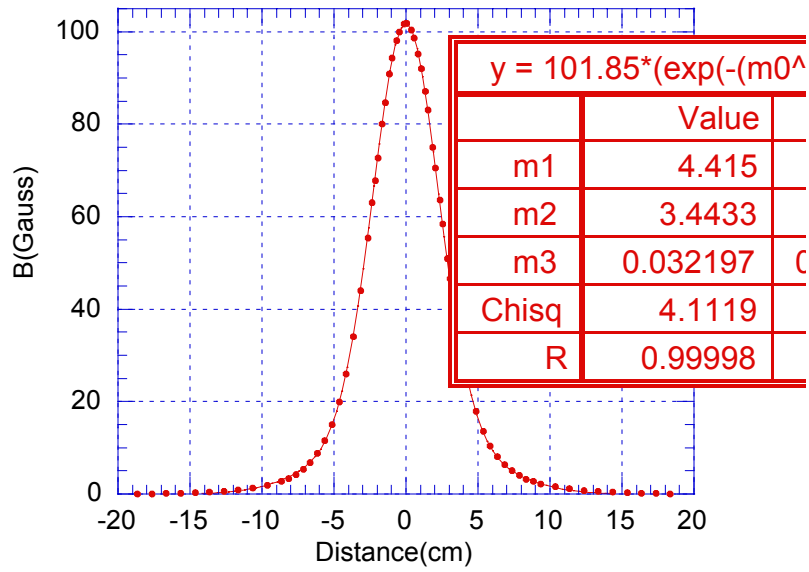
Calibration for M1
B(peak)-I

y = m1 + m2 * I

	Value	
m1	0.85385	
m2	17.632	(
Chisq	1.4429	
R	0.99998	
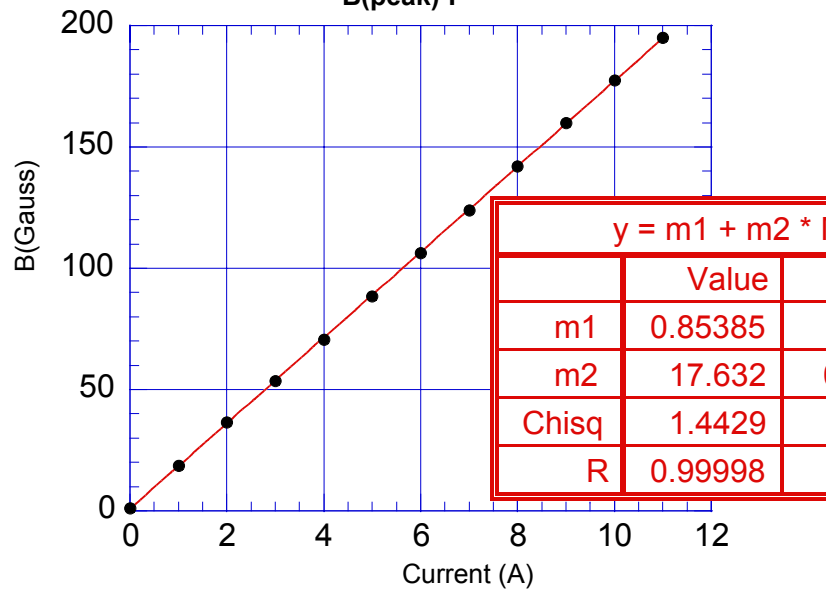
Figure 5.3. Measured axial magnetic field profile along the axis for M1

Short Solenoid M2 B-field
effective length=4.243 (I=5.7A)

y = 105.14*(exp(-(m0^

	Value	
m1	3.8872	
m2	3.9366	
m3	0.08451	0
Chisq	69.382	
R	0.99965	

B(Gauss)

Distance (cm)

Calibration for M2
B(Peak)-I

y = m1 + m2 *

	Value
m1	1.9785
m2	18.13
Chisq	1.6802
R	0.99998

B(Gauss)

Current(A)
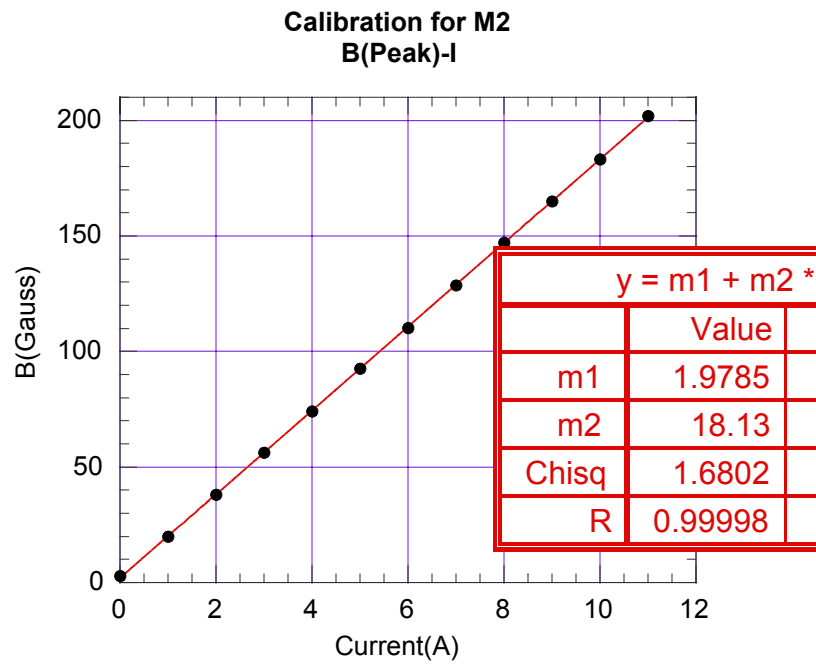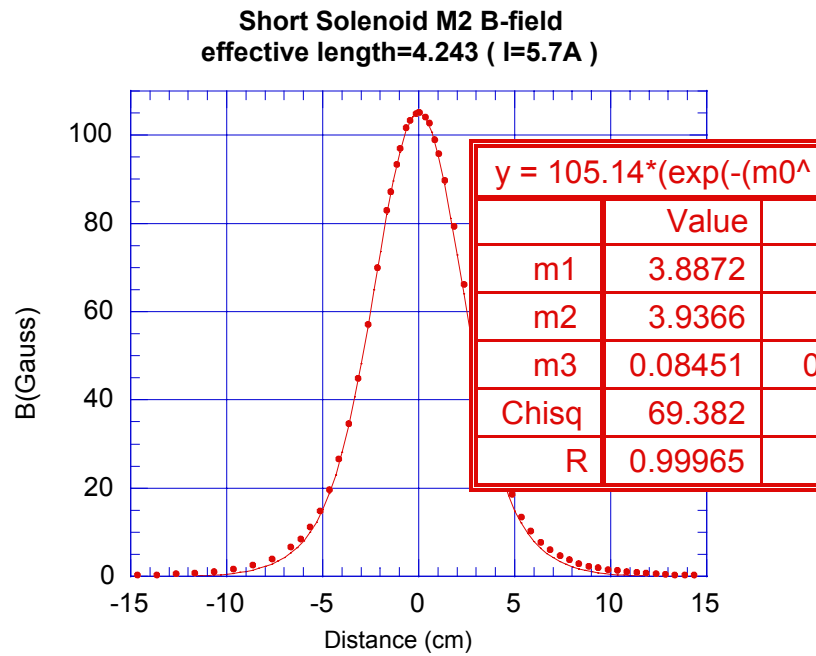
Figure 5.4. Measured axial magnetic field profile along the axis for M2

Short Solenoid M3 B-field
effective length=7.278cm (I=7A)

$y = 39.16*(exp(-(m0^\wedge$

	Value
m1	7.2778
m2	5.689
m3	0.04654
Chisq	16.883
R	0.99937

Calibration for M3
B(peak)-I

$y = m1 + m2 * M$

	Value	
m1	-0.31124	
m2	5.6575	0
Chisq	1.7841	
R	0.99985	
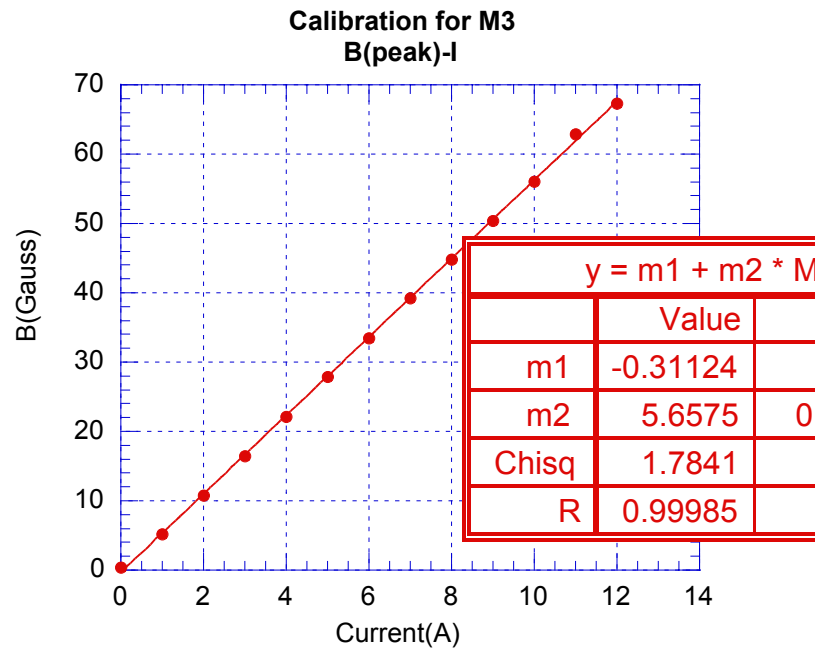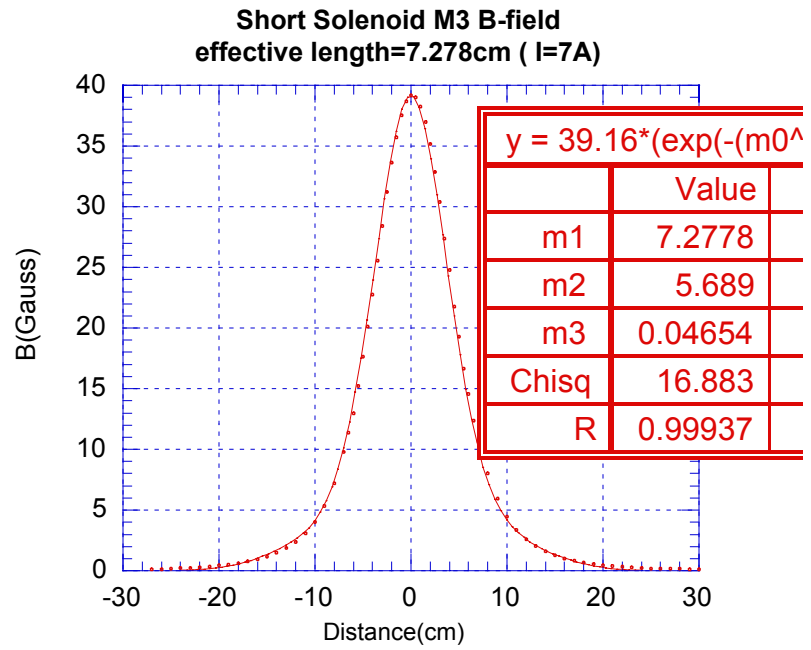
Figure 5.5. Measured axial magnetic field profile along the axis for M3

Long Solenoid M4 B-field
effective length=130cm

y = m1*(m0/(m0^ 2+m3*r		
	Value	
m1	24.128	
m2	137.08	
m3	5.0408	
Chisq	27.239	
R	0.99972	

B (Gauss) vs Distance (cm)

Calibration for M4
B(peak)-I

y = -0.12786 + 7.4153x R= 1

Axial Magnetic Field (Gauss) vs Current (A)
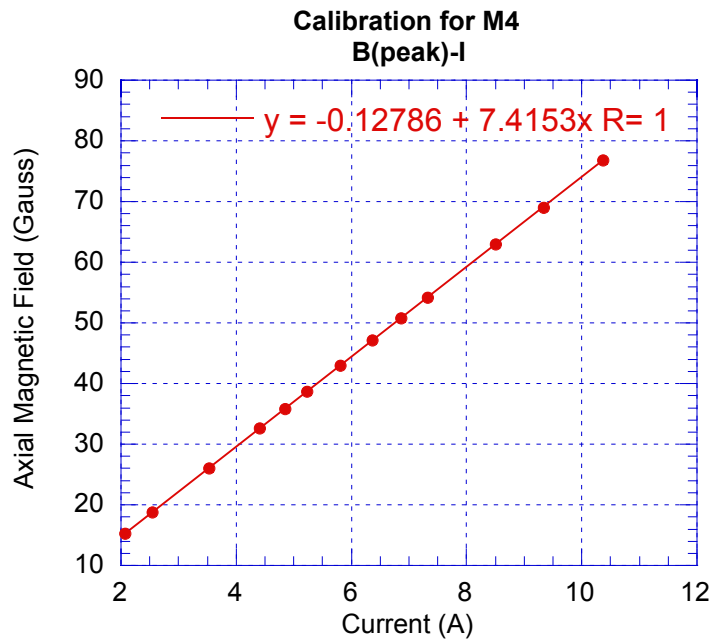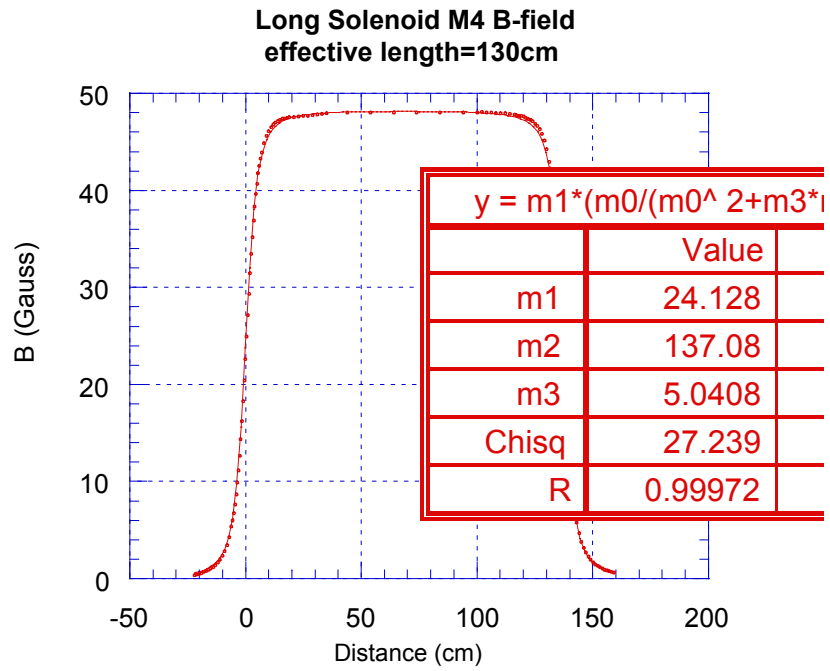
Figure 5.6. Measured axial magnetic field profile along the axis for M4

Short solenoid M5 B-field

y = 66.86*(exp(-(m0

	Value
m1	4.9058
m2	4.2547
m3	0.028149
Chisq	42.382
R	0.99929

B (Gauss)

Distance (cm)

Calibration for M5
B(peak)-I

y = 0.30902 + 9.4425x R= 0.99994

B (Gauss)
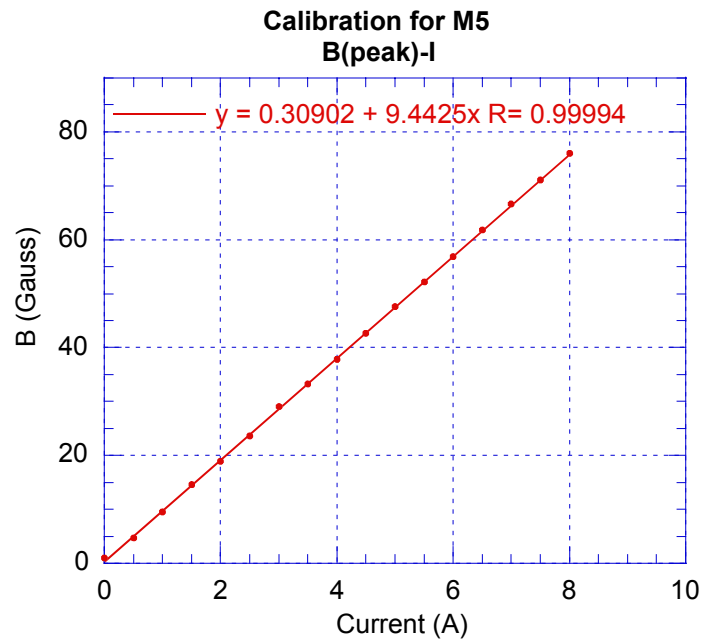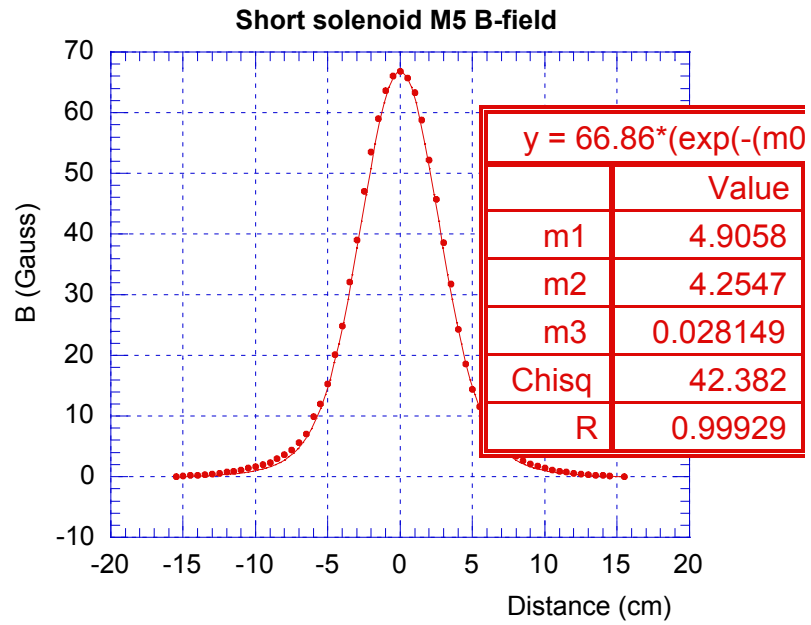
Current (A)

Figure 5.7. Measured axial magnetic field profile along the axis for M5

### 5.2.3 Diagnostics

To monitor beam transport, three current monitors are used in the experimental setup. The first current monitor is a Bergoz coil, which is located between the first and second short solenoid, about 20 cm from the anode of the electron gun. The Bergoz coil is a high-resolution current monitor with rise time of 0.2 ns and a sensitivity of 1.2 V/A. The other two current monitors are resistive current monitors with a sensitivity of 1.1 V/A. One is located at the entrance of the long focusing transport channel, and the other is located at the exit of the transport channel. The distance between the two current monitors is 1.48 m. Signals from the three current monitors are measured with an oscilloscope (Tektronix DSA 602A). At the exit of the transport line, there is an axially movable phosphor screen system used for alignment purposes.

5.2.4 Vacuum system

The phosphor screen system is movable in a differential pumping system. The differential pumping system has two different vacuum regions. As shown in Figure 5.8, the high vacuum in the transport line is isolated from the low vacuum by two spring-loaded teflon rings, which have super-low friction. The inner diameter of the ring is 1.25 inch and the outer diameter is 1.5 inch. The phosphor screen in the front always stays in the high vacuum region. One stainless steel tube, which has a diameter of 1.25 inch and holds the phosphor, is movable through the regions of air, low vacuum and high vacuum. Pressure in the low vacuum region is kept at about 10^{-4} Torr with a roughing pump. Pressure in the high vacuum region is maintained by four ion pumps, with a very high vacuum at low 10^{-8} to high 10^{-9} Torr. The first ion

pump is located at the electron gun with a capacity of 8 l/s. The other three ion pumps have capacities of 40 l/s, one located between the second and third solenoid and two located at the diagnostic chamber. Electron beam emission at the gun is very sensitive to the pressure at the cathode region. The dispenser cathode has been used for a few years and its emission is gradually deteriorating. When the gridded electron gun was used for the energy spread evolution experiment, the emission was insufficient in the low 10^{-8} Torr region. To obtain an ultra-high vacuum, the system is baked with heating tapes. The temperature of the heating tapes is about $220°C$ and metal parts are heated to about $160°C$. Gas adhering to the wall of the metal tube will be evaporated and ionized. After one week of pumping and baking, all the heating tapes are turned off and the system is cooled down. In this way, a much lower vacuum pressure in the range of low 10^{-9} Torr was obtained. The emission of the cathode becomes normal in the ultra-high vacuum when the heating voltage of the cathode is operating at 7.5 V.
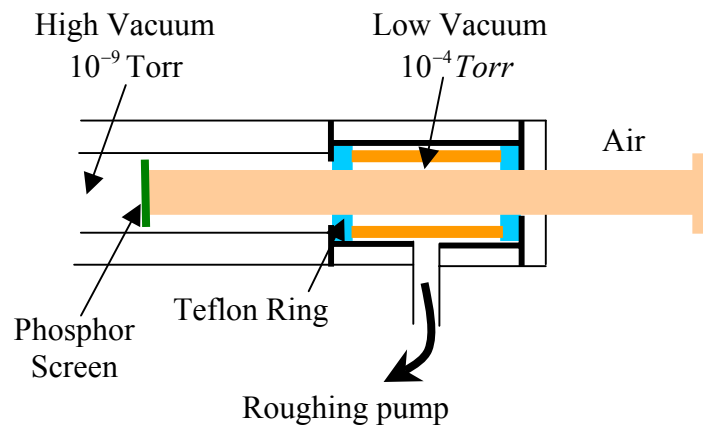
Figure 5.8. Schematic of differential pump system

5.3 Beam Transport in a Uniform Focusing Channel

The beam propagates in the long solenoid, which provides uniform focusing for the electrons. For a matched beam in the uniform channel, the beam radius is a constant and the slope is 0, that is $R(z) = a$, $R''(z) = 0$. The matched beam equation is (see Equation 4.88a in Ref. [1])

$$k_0^2 a - \frac{K}{a} - \frac{\varepsilon^2}{a^3} = 0. \quad (5.4)$$

The term $k_0^2 a$ represents the linear external focusing force. The parameter k_0 is the wave number, defined as $k_0 = \frac{\omega_0}{v} = \frac{|qB|}{2mc\beta\gamma}$. ω_0 is the betatron oscillation frequency of the particles due to the applied focusing force alone and v is beam velocity. B is the external focusing magnetic field. In Equation (5.4), K is the generalized perveance and ε is the unnormalized beam emittance. These two terms generate defocusing forces.

To obtain the solution $R(z) = a$, the beam must be properly matched into the focusing channel. In the long solenoid case, the beam injection conditions at the entrance of the long solenoid must be chosen such that $R = a$ and $R' = 0$ when the beam reaches the uniform-focusing plateau inside the channel after passing through the fringe-field region. There are several possibilities for satisfying the matching requirements, each of which involves at least two parameters, such as lens strength and position, to control both radius and slope of the beam envelope. We use three short matching lenses (M1, M2, and M3) at the fixed positions and vary the focusing strengths of the three lenses to control the beam radius and slope for proper matching.

The extra focusing variable can give us more flexibility in the beam matching. Theoretically, these three matching lenses can achieve an infinite number of solutions for beam matching into the long solenoid with matched beam radius a. However, in practice we choose the matching solution that can match the beam into to the long solenoid smoothly and avoid beam over-expanding or over-focusing in the matching lenses.

When we designed this experiment, we used the particle-in-cell code WARP [36] and SPOT [37] to simulate the beam matching to decide the positions and strengths of the matching lenses. It was time-consuming using WARP to do beam matching because we need to try the different parameters of positions and strengths of the matching lenses manually to get a matching solution. SPOT can automatically get the matching solution, but it uses effective length of the focusing lenses, not the real field of the solenoid. SPOT does not have a user-friendly interface for the parameter set-up and it also has some problems running in Windows 2000.

To overcome these limitations, we have developed a MATLAB code "Match", specifically for this experimental setup, to determine the optimal lens strengths to match a beam from a given initial state to a prescribed final expectation state. It is very easy to set up the parameters including beam energy, beam current, initial beam size and slope, location of the initial beam and beam emittance, positions and strengths of 5 lenses, currents of the power supplies for the lenses, expected beam size, energy analyzer position, etc., using its friendly interface. "Match" obtains beam envelopes by numerically solving the differential beam envelope equation from Equation (4.85a) in Ref. [1],

$$R''+ k_0^2 R - \frac{K}{R} - \frac{\varepsilon^2}{R^3} = 0 . \qquad (5.5)$$

The term $k_0^2 R$ represents the linear external focusing force. In this code, we use the real magnetic fields of the solenoids. The interface of this code with a mismatched beam envelope is shown in Figure 5.9.
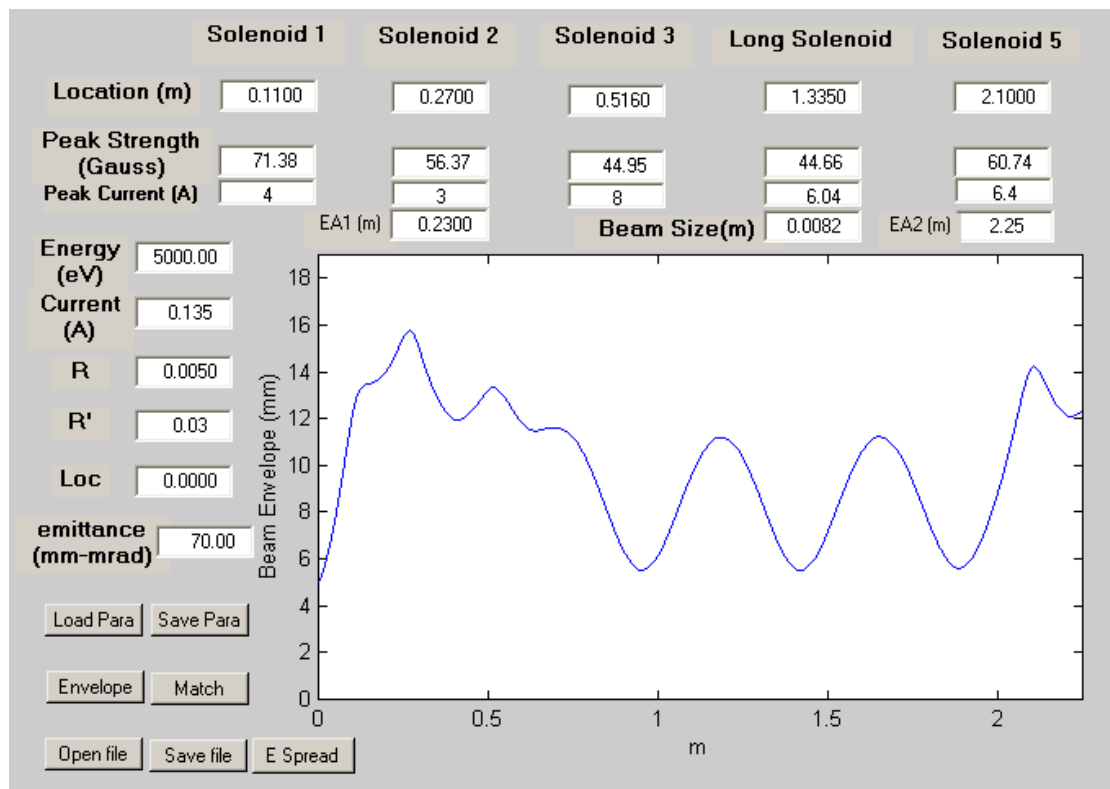
Figure 5.9. Interface with a mismatched beam envelope

By adjusting the focusing strengths of two matching solenoids, this code can automatically find the right strengths and find the matched beam envelope in the uniform focusing channel by solving the beam response matrix. We define the strengths of two matching solenoids as a variable vector $S = \begin{bmatrix} s_1 \\ s_2 \end{bmatrix}$. The initial value of S is S_0, and the corresponding beam envelope at the focusing channel is $\gamma_0 = \begin{bmatrix} r_0 \\ r_0' \end{bmatrix}$.

Adding small perturbations on the matching strengths of two lenses, the beam envelope at the focusing channel is $\gamma = \begin{bmatrix} r \\ r' \end{bmatrix}$, which can be written as

$$\gamma \simeq \gamma_0 + \frac{\partial \gamma}{\partial S}(S - S_0), \qquad (5.6a)$$

or

$$\begin{bmatrix} r \\ r' \end{bmatrix} = \begin{bmatrix} r_0 \\ r_0' \end{bmatrix} + M \begin{bmatrix} \Delta s_1 \\ \Delta s_2 \end{bmatrix}. \qquad (5.6b)$$

Equation (5.6b) can be written as

$$\begin{bmatrix} \Delta r \\ \Delta r' \end{bmatrix} = M \begin{bmatrix} \Delta s_1 \\ \Delta s_2 \end{bmatrix}, \qquad (5.7a)$$

or

$$\Delta \gamma = M \Delta S. \qquad (5.7b)$$

Here $\Delta \gamma = \begin{bmatrix} \Delta r \\ \Delta r' \end{bmatrix} = \begin{bmatrix} r - r_0 \\ r' - r_0' \end{bmatrix}$.

To solve the above matrix, we try two small perturbations on two matching solenoid independently so that we get two equations,

$$\begin{cases} \begin{bmatrix} r_1 \\ r_1{'} \end{bmatrix} = \begin{bmatrix} r_0 \\ r_0{'} \end{bmatrix} + M \begin{bmatrix} \Delta s_1 \\ 0 \end{bmatrix} \\ \begin{bmatrix} r_2 \\ r_2{'} \end{bmatrix} = \begin{bmatrix} r_0 \\ r_0{'} \end{bmatrix} + M \begin{bmatrix} 0 \\ \Delta s_2 \end{bmatrix} \end{cases} \qquad (5.8a)$$

or

$$\begin{cases} \begin{bmatrix} \Delta r_1 \\ \Delta r_1{'} \end{bmatrix} = M \begin{bmatrix} \Delta s_1 \\ 0 \end{bmatrix} \\ \begin{bmatrix} \Delta r_2 \\ \Delta r_2{'} \end{bmatrix} = M \begin{bmatrix} 0 \\ \Delta s_2 \end{bmatrix} \end{cases} . \qquad (5.8b)$$

From this equation, the beam response matrix is

$$M = \begin{bmatrix} \dfrac{\Delta r_1}{\Delta s_1} & \dfrac{\Delta r_2}{\Delta s_2} \\ \dfrac{\Delta r_1{'}}{\Delta s_1} & \dfrac{\Delta r_2{'}}{\Delta s_2} \end{bmatrix} \qquad (5.9)$$

when the matching strength is S_0. Beam envelope changes (Δr and $\Delta r{'}$) at the uniform focusing channel could be found by solving the beam envelope equation.

The expected matching solution at the entrance of the long solenoid channel is $\begin{bmatrix} a \\ 0 \end{bmatrix}$. The difference between the matching solution and beam envelope γ_0 is $\Delta \gamma = \begin{bmatrix} a - r_0 \\ 0 - r_0{'} \end{bmatrix}$, the matching strength change can be obtained from Equation (5.7b)

$$\Delta S = \begin{bmatrix} \Delta s_1 \\ \Delta s_2 \end{bmatrix} = M^{-1} \Delta \gamma . \qquad (5.10)$$

The new matching strength vector is then found as

$$S = S_0 + \Delta S = S_0 + \begin{bmatrix} \Delta s_1 \\ \Delta s_2 \end{bmatrix} . \qquad (5.11)$$

107

Setting the beam envelope change $\Delta\gamma$ as a solution and iterating the above processes, we can find the matched beam in the uniform focusing channel. In the code, given the first solenoid focusing strength and the condition at the entrance, a matched beam envelope can be calculated by automatically changing the strength of the second and third matching solenoids. For a 5 keV, 135 mA beam, beam initial radius, slope, and normalized effective emittance are 5 mm, 0.03 rad, and 10 μm. The matched beam envelope equation relates the four quantities a, k_0, K, and ε and can be solved for any quantity if the other three are given. So a beam passes through the long solenoid with radius of about 8 mm, the focusing strength of the long solenoid is 44.7 Gauss obtained in the code "Match" according to Equation (5.4). At the beginning, we set the focusing strengths of M1, M2, and M3 at 71.4, 56.4, and 45 Gauss respectively. The beam envelope is mismatched in the uniform focusing channel as shown in Figure 5.9. In the automatic matching process, the code adjusts the focusing strength of M2 and M3 and finds the optimal focusing strength of 54.4 Gauss and 50 Gauss, respectively. The matched beam envelope is shown in Figure 5.10. The whole automatic matching process is accomplished in less than one second, which greatly improves efficiency.
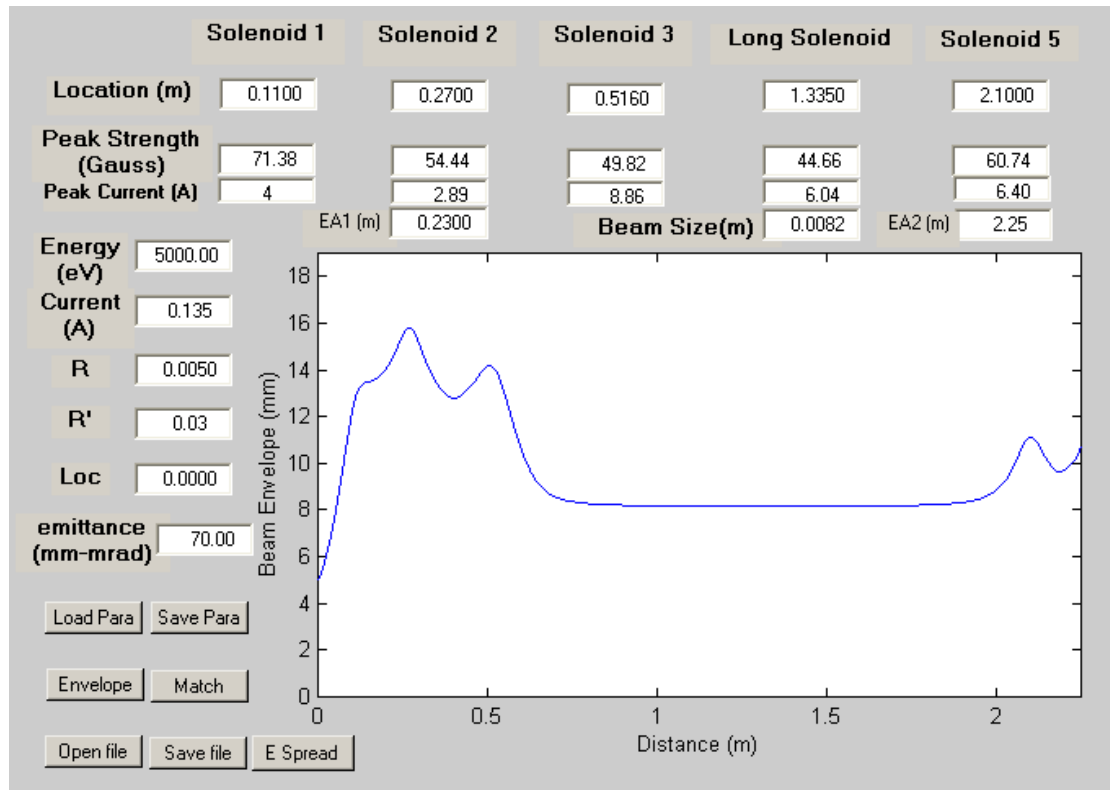
Figure 5.10. Interface with a matched beam envelope

In the beam envelope Equation (5.5), the term $k_0^2 R$ represents the linear external focusing force. The parameter k_0 is the wave number, defined as $k_0 = \dfrac{\omega_0}{v}$. ω_0 is the betatron oscillation frequency of the transverse particle oscillations due to the applied focusing force alone and v is the beam velocity. The wave number is given by (see equation 4.85a in Ref. [1])

$$k_0 = \frac{|qB|}{2mc\beta\gamma},\qquad(5.12)$$

here B is the external focusing magnetic field.

The generalized perveance K is

$$K = \frac{I}{I_0}\frac{2}{\beta^3\gamma^3}.\qquad(5.13)$$

The oscillation wave number k of the particles due to the action of both the external focusing force and the space-charge force is defined as

$$k^2 = k_0^2 - \frac{K}{a^2}\qquad(5.14)$$

here, a is matched beam size. This equation can be expressed as

$$\frac{k}{k_0} = \sqrt{1 - \frac{K}{k_0^2 a^2}}\qquad(5.15)$$

The ratio of $\dfrac{k}{k_0}$ is known as the tune depression due to the space charge. In this equation, $\chi = \dfrac{K}{k_0^2 a^2}$ is the beam intensity parameter, defined by Martin Reiser [38].

Equation (5.15) can be expressed as $\dfrac{k}{k_0} = \sqrt{1 - \chi}$. When χ is larger than 0.5, then

beam is space-charge-dominated. When χ is less than 0.5, the beam is emittance dominated.

The plasma frequency ω_p is defined by $\omega_p^2 = \dfrac{2Kv^2}{a^2}$. The Equation (5.14) can be expressed in terms of the plasma wave constant $k_p = \omega_p / v$ as

$$k^2 = k_0^2 - \frac{k_p^2}{2}, \qquad (5.16)$$

or in terms of the frequencies as

$$\omega^2 = \omega_0^2 - \frac{\omega_p^2}{2}. \qquad (5.17)$$

When the beam is not matched, the beam envelope radius becomes a periodically varying function of distance z in the uniform focusing channel. For small amplitude oscillations, we can linearize Equation (5.5) and find the approximate wavelength of the oscillated envelope. Let

$$R = a + x \qquad (5.18)$$

where $|x| \ll a$ and a is the matched beam radius while x is the oscillation amplitude in the linear approximation. Substituting Equation (5.18) into Equation (5.5), we get

$$x'' + \left(k_0^2 + \frac{K}{a^2} + 3\frac{\varepsilon^2}{a^4} \right) x = 0, \quad (5.19)$$

which can be expressed in the equivalent form $x'' + k_e^2 x = 0$. The parameter $k_e = \dfrac{2\pi}{\lambda_e}$ is the wave number, and $\omega_e = k_e v$ is the angular frequency of the envelope oscillations. By eliminating ε in Equation (5.19) with the aid of Equation (5.4), k_e

and ω_e can be obtained in the following forms (see Equation (4.105a) and (4.105b) in Ref. [1])

$$k_e = \left[2k_0^2 + 2k^2 \right]^{1/2} = \sqrt{2}k_0 \left[1 + \left(\frac{k}{k_0} \right)^2 \right]^{1/2} \qquad (5.20)$$

$$\omega_e = \left[2\omega_0^2 + 2\omega^2 \right]^{1/2} = \sqrt{2}\omega_0 \left[1 + \left(\frac{\omega}{\omega_0} \right)^2 \right]^{1/2} \qquad (5.21)$$

The wavelength λ_e of the beam envelope oscillation is given by

$$\lambda_e = \frac{2\pi}{k_e} = \frac{2\pi v}{\omega_e} \qquad (5.22)$$

The frequency ω_e of the beam envelope oscillation differs from the frequency ω of the particle oscillations within the beam. In the limit of zero intensity ($K = 0$), we have $\omega = \omega_0$ and $\omega_e = 2\omega_0$. In the long solenoid, individual particles oscillate with the Larmor frequency, $\omega_0 = \omega_L$, while the envelope of the mismatched beam oscillates with the cyclotron frequency, $\omega_e = 2\omega_0 = 2\omega_L = \omega_c$. For ideal Brillouin flow ($\varepsilon = 0$), we have $\omega = 0$ and $\omega_e = \sqrt{2}\omega_0 = \omega_p$. Table 5.4 shows the beam parameters for a 5 keV, 135 mA beam when beam size is 8.2 mm in the long solenoid. Normalized effective emittance is 10 μm. We can see in this space-charge-dominated beam that the tune depression is $\frac{\omega}{\omega_0} = 0.12$. The oscillation wavelength is 0.47 m as shown in Figure 5.9 when the beam envelope has a small mismatch oscillation in the long solenoid.

β	v (m/s)	a (mm)	ω_0 (rad/s)	ω_p (rad/s)	ω_e (rad/s)	ω (rad/s)	λ_e (m)
0.14	4.16×10^7	8.2	3.9×10^8	5.47×10^8	5.55×10^8	4.7×10^7	0.47

Table 5.4. Beam Parameters for a 5 keV, 135 mA beam

In the "Match" program, the envelope $\gamma = \begin{bmatrix} r \\ r' \end{bmatrix}$ is not sampled at one single point in the uniform focusing channel, but as an average beam size and average slope of the envelopes with length of $\lambda_e / 4$. By doing this, we can avoid the situation that the envelope value at one special point is satisfied with the target point requirements while the envelope still oscillates in the uniform focusing channel. For example, in Figure 5.9, the beam is mismatched. We choose the average envelope in the length of 0.12 m starting from the point that the envelope crosses over average size "a" in the uniform focusing channel.

The matched beam envelope in the Figure 5.10 is shown in Figure 5.11 and the magnetic field of the focusing channel is shown in Figure 5.12.
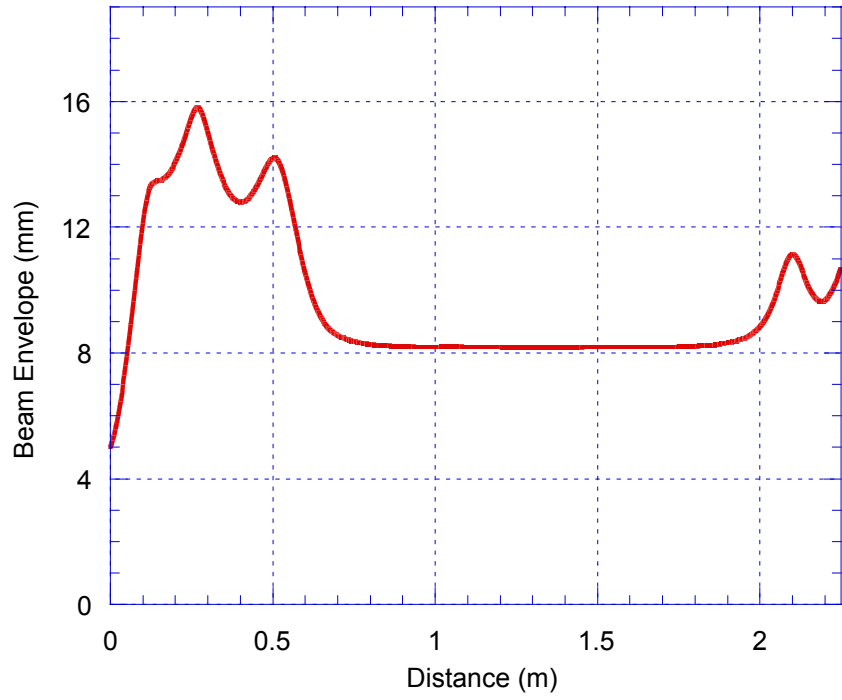
Figure 5.11. The matched beam envelope for a 5 keV, 135 mA beam
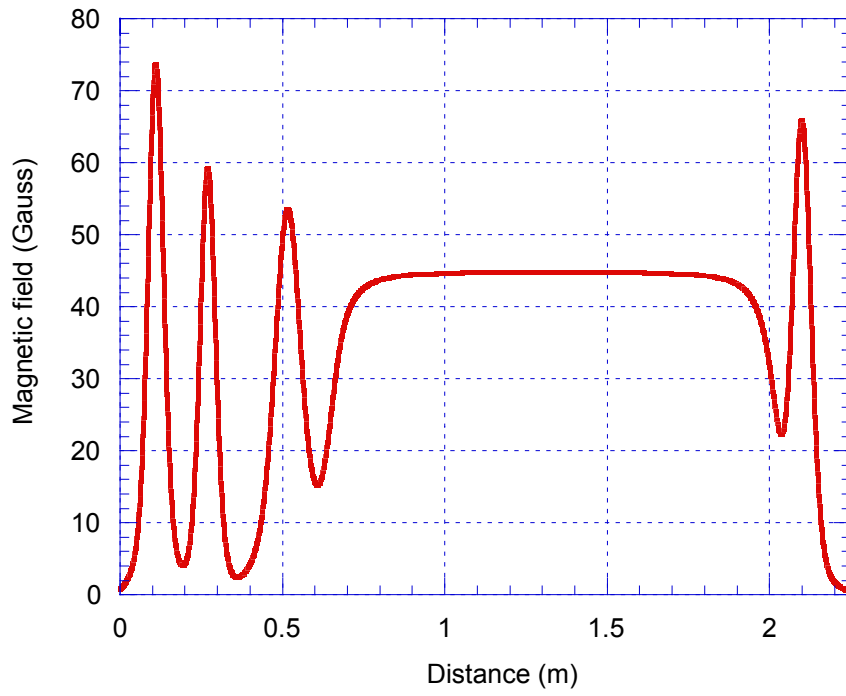
Figure 5.12. The magnetic field of the focusing channel

5.4 Calculation of Energy Spread Evolution

The code "Match" has another function, namely calculating the energy spread along the focusing channel. The energy spread evolution theories have been reviewed in Chapter 2. We numerically calculate the beam energy spread increase as the beam envelope changes. The longitudinal energy spread is obtained at various points along the z-axis. There are three things to be noted in this calculation.

1. The longitudinal-longitudinal relaxation is a fast process and the relaxation is finished within a couple of plasma periods. It is easy to calculate the longitudinal-longitudinal effect because it only depends on the particle density n (see Equation 6.159 in Reference [1]) and beam energy V_0.

$$n = \frac{I}{ea^2 \pi v}, \qquad (5.23)$$

   where a is the beam radius and changes along the z-axis, I is the beam current, and v is the beam velocity.

2. Intrabeam scattering (Boersch effect) is a slow process and gradually it will become dominant after the beam travels about 25 cm. The calculation in the code considered both the intrabeam scattering and the longitudinal-longitudinal effects.

3. If the beam size is compressed or expanded by a factor of R_{i-1}/R_i (R_i and R_{i-1} are beam sizes at adjacent steps in the transport direction), the transverse temperature will be $k_B T_{\perp i} = k_B T_{\perp i-1} \left(R_{i-1}/R_i \right)^2$.

116

4. Relaxation time of the intrabeam scattering is related to the beam density. Beam energy spread increase is related to the travel time, beam density, and beam size from the scaling law discussed in Chapter 2.

Figure 5.13 is a calculation result of beam energy spread evolution for a 5 keV, 135 mA beam transported through the focusing channel with an average beam size of 8 mm. The average particle density is about $9.6 \times 10^{13} / m^3$. The beam acceleration time from the cathode to the anode in the electron gun is about 0.8 ns and the plasma period is about 11.5 ns. Compared with the plasma period, the beam acceleration is a fast procession. The travel time of the beam is about 54 ns from the anode to the measurement position at 2.3 m. The beam energy spread starts from 1.5 eV at the anode of the electron gun, which is caused by the longitudinal-longitudinal effect, and increases to about 4 eV at the 2.3 m from the anode of the electron gun.
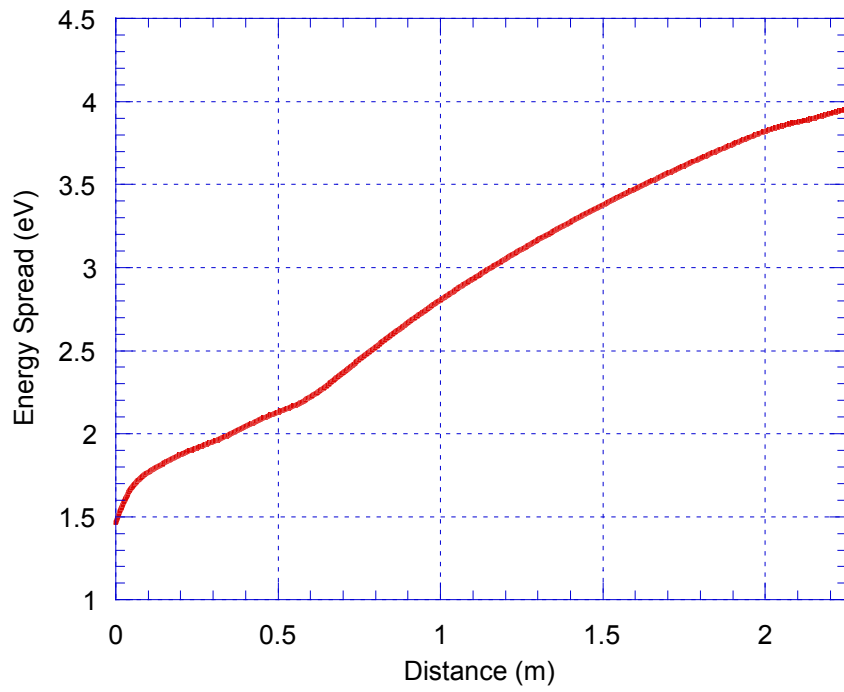
Figure 5.13. Beam energy spread evolution along the transport line

5.5 Experimental results and Comparison with theoretical predictions

The energy spread measurement of the beam after long distance transport has been done and the energy analyzer is located at 2.3 m away from the electron gun. The beam densities in the uniform focusing channel are adjustable by changing the focusing strength of the long solenoid. The "Match" code gives us guidance to adjust the matching strengths of three short solenoids to get the beam matched in the uniform channel and passing through the long solenoid without loss. The experimental matching strengths of the solenoids are compared with those in the "Match" solution in Table 5.5 when the average beam size in the uniform channel is about 8 mm and the focusing strength of the long solenoid is 44 Gauss. The reading errors of the focusing current of the solenoids are about 0.2 A. The error bars of the experimental magnetic field are listed in Table 5.5.

Solenoids strength	M1	M2	M3	M4
Theoretical value (Gauss)	71.4	61.0	49.1	44.7
Experimental Value (Gauss)	71 ± 4	55 ± 3.5	53 ± 1	44 ± 1

Table 5.5. Comparison of the experimental and theoretical strengths of matching and focusing solenoids

The signals from three current monitors are used to judge beam loss during transport. The positions of these current monitors are listed in Table 5.6. For a 5 keV beam, the travel time of the beam to the positions of the current monitors are also listed in this Table. Figure 5.14 shows the beam current signals measured by three current monitors along the transport line when the beam average size is 8 mm in the uniform channel. The particles have about 5% loss in the uniform focusing channel. This loss is so small that the error caused by this beam loss is negligible in the measurement of the energy spread. Compared with the signal of the first current monitor, the time delays of the second and third current monitors are ~6 ns and ~47 ns. The calculated signal delays from Table 5.6 are about ~ 8 ns and ~44 ns. We believe the measurement error is about several ns due to different cable length. In Figure 5.14, the second and third current monitor signals have 3 ns and 10 ns rise time due to the beam longitudinal expansion. From the theoretical calculation, the rise time is about 2.5 ns and 15 ns, respectively.

Current Monitor	#1	#2	#3
Distance to the Anode	21cm	58 cm	205 cm
Calculated travel time	~ 5 ns	~ 13 ns	~ 49 ns

Table 5.6. Positions of current monitors and travel time for a 5 keV beam.
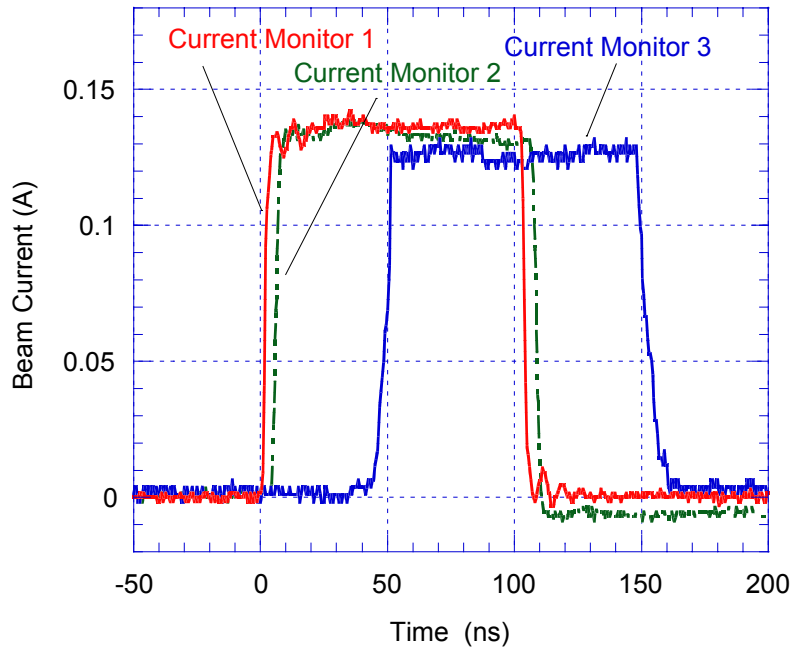
Figure 5.14. Beam current measured in the different positions along the

transport line.

We adjust the focusing strength of the last short solenoid M5 to control the amount of current injected into the energy analyzer. This current signal forms a 10 mV signal on the collector of the analyzer. Setting the focusing voltage of the energy analyzer at 120 V in the amplitude higher than the retarding voltage, we measured the beam energy spread at the distance of 2.23 m from the anode of the electron gun.

Figure 5.15 is a measured energy spectrum for a beam with energy of 5 keV and current of 135 mA when the average beam size is about 8 mm in the uniform focusing channel. The rms energy spread is 4.0 eV, FWHM is 8.3 eV, and the mean energy is 5068.5 eV. The energy spread measurement result has excellent agreement with the theoretical agreement of 4.0 eV shown in Figure at the position of 2.3 m. Figure 5.16 shows the beam energy spread along the beam pulse. Average energy spread of the main beam is 4.0 eV. The energy spread drops from 10 eV to 4 eV in 20 ns of the beam pulse. It is still under investigation why there is a large energy spread at the beam head.
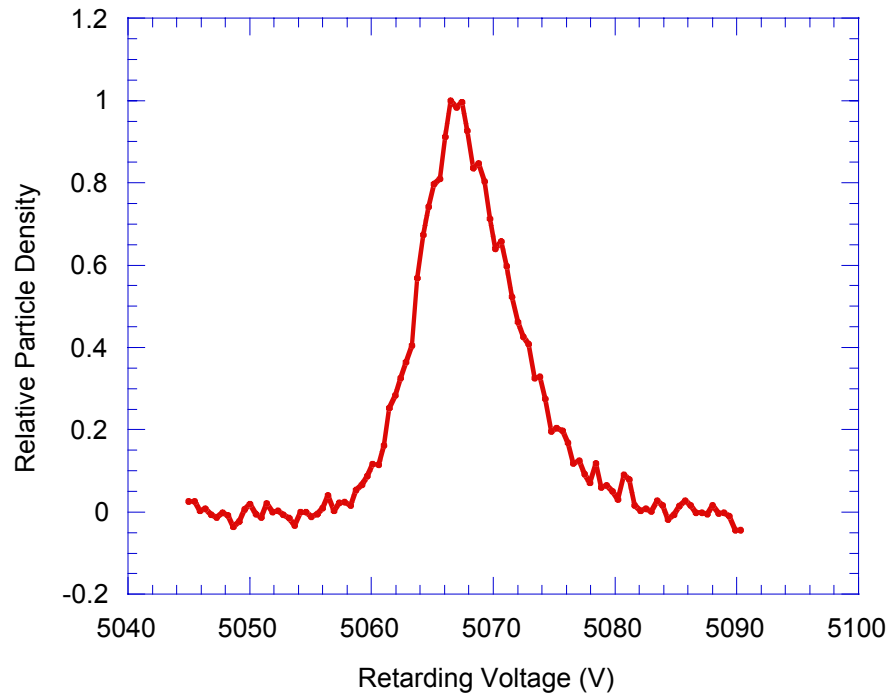
Figure 5.15. Energy spectrum for a beam with energy of 5 keV and current of 135 mA. The rms energy spread is 4 eV, FWHM is 8.3 eV, and mean energy is 5068.5 eV.
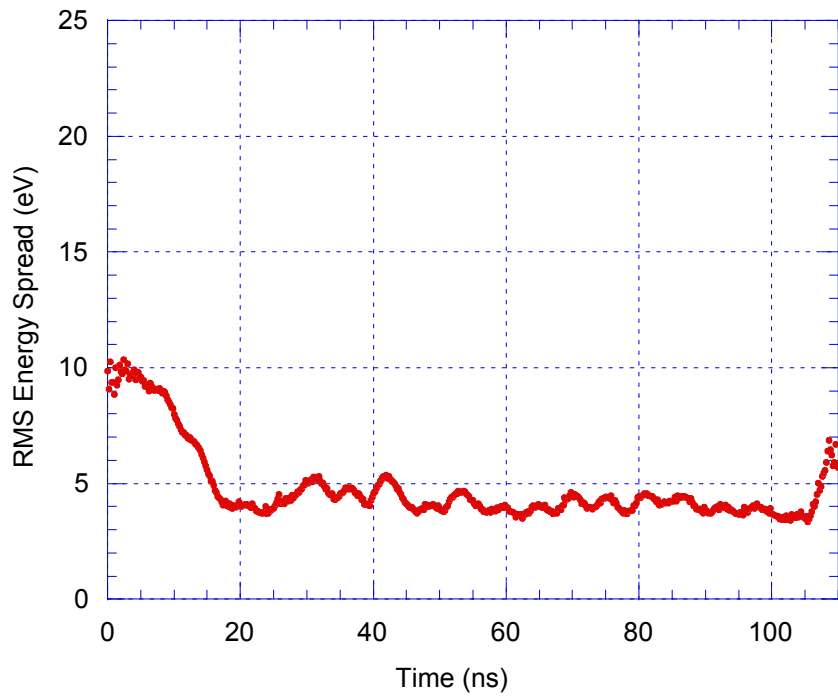
Figure 5.16. Beam energy spread along beam pulse for a beam with energy of

5 keV and current of 135 mA. Average energy spread of the main beam is 4.0 eV

5.6 Scaling Law

In chapter 2, we derived the scaling law to describe the relation of the beam energy spread evolution. According to this scaling law, after the beam travels a long distance, intrabeam collisions will be dominant and the beam energy spread is only related to the beam radius, beam current, and beam relaxation time (or distance traveled).

The beam energy spread is measured at different beam densities. This is achieved by changing the focusing strength of the long solenoid and with the beam current fixed at 135 mA for a 5 keV beam. For each condition, the solenoids in the matching section are also adjusted to match the beam into the long solenoid.

The beam energy spread is also measured at the different beam currents. This is achieved by changing the acceleration voltages in the electron gun.

Figure 5.17 - 5.19 depict the experimental results at different beam sizes for different beam energy. In the figures the beam energy spread is plotted against the ratio of I/a, and a is the matched beam radius inside the solenoid channel. In the Figure 5.17- 5.19, circles with solid line are the theoretical predictions according to theory and dots with dotted line are the experimental results when the beam current is 135 mA for a 5 keV beam, 100 mA for a 4 keV beam and 70 mA for a 3 keV beam, respectively. Error bars added on the measured energy spread are determined by the resolution of the energy analyzer and the measurement errors in the experiment.

From the figures, we can see that the measured beam energy spread is higher at higher beam densities (radius is smaller), as expected. The comparison shows that the

agreement between the experiment and the theory is remarkably good, especially at relatively large beam radii, or low beam densities given the same total beam current. At higher beam densities, however, it appears that the experimental results starts to deviate from the theory, showing higher energy spread.
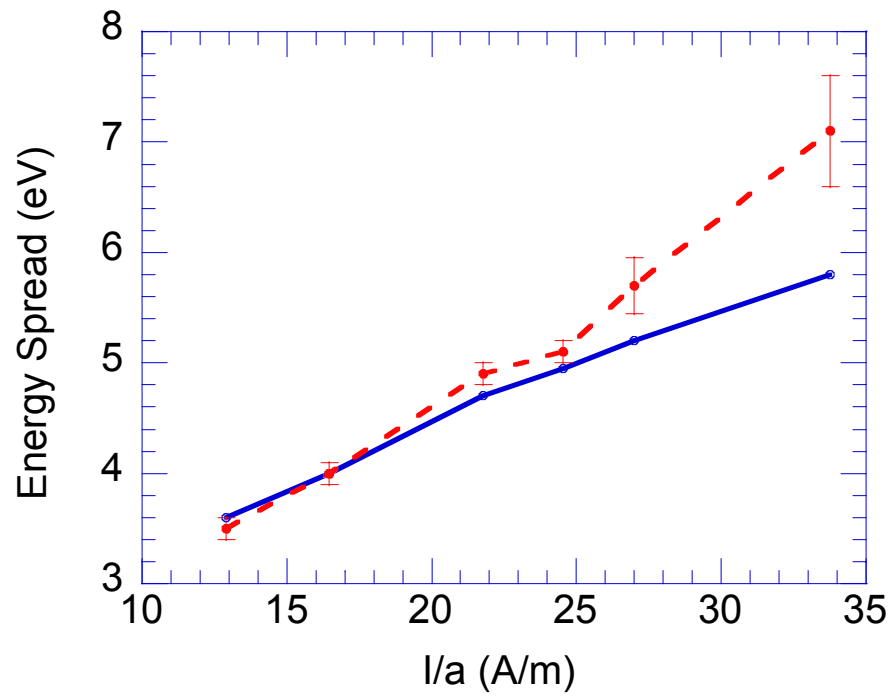
Figure 5.17. Beam energy spread when the beam current is 135 mA for a 5

keV beam with different beam sizes.
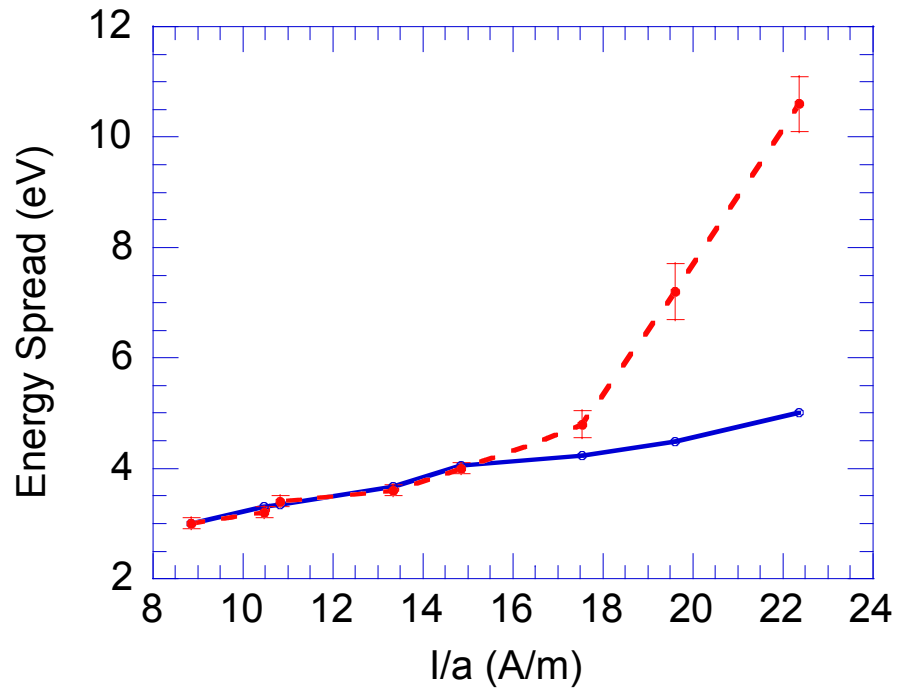
Figure 5.18. Beam energy spread when the beam current is 100 mA for a 4

keV beam with different beam sizes.
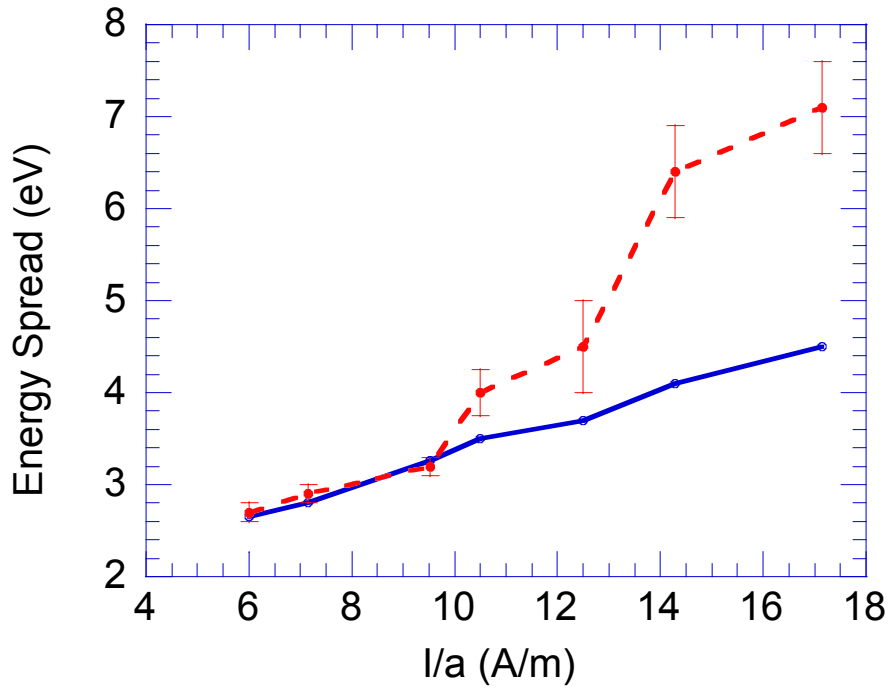
Figure 5.19. Beam energy spread when the beam current is 70 mA for a 3 keV

beam with different beam sizes.

Figure 5.20 depicts the logarithm of the measured beam energy spread ΔE against the logarithm of the ratio of current to radius for different beam energies. Dots with dotted line are the experimental data for a 5 keV beam. Triangles with dotted line are the experimental data for a 4 keV beam. Crosses with dotted line are the experimental data for a 3 keV beam. We can find that in the low current density region, experimental data points at different beam energies are lying around a common linear base line. The linear fit of these data points has a slope of 0.46, which is in good agreement to the predications of 0.5 from the scaling law discussed in Chapter 2. There are erratic experimental points, which deviate from the linear fit. These points are taken when the beam radius is very small or the beam current density is very high. It appears that under this condition, the beam energy spread follows a different law. The threshold of $\log(\Delta E)$ for larger energy spread depends on the beam energy. From the figure, the threshold is lower for lower beam energy. This might be related to the faster equipartitioning of the beam temperature due to collective forces and effects other than Coulomb collisions. The exact mechanisms causing this abnormal energy spread at high density will be a subject for future study.
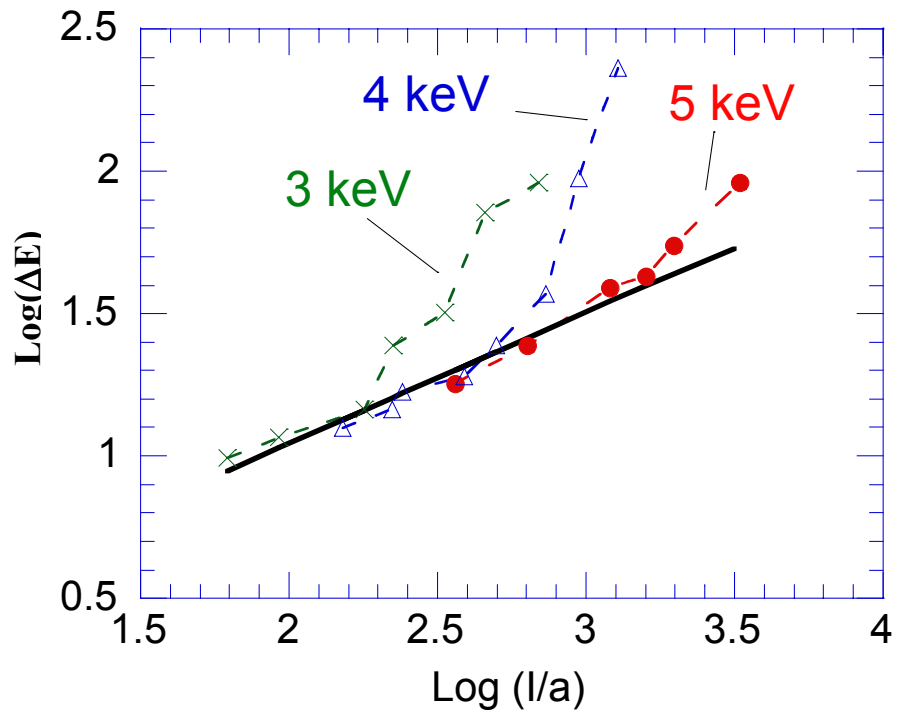
Figure 5.20. Scaling law: $\ln \Delta \tilde{E}$ vs. $\ln\left(\dfrac{I}{a}\right)$. Dots are for a 5 keV beam,

triangles for a 4 keV beam, and crosses for a 3 keV beam.

Chapter 6 : Conclusion

A novel cylindrical retarding electrostatic field energy analyzer for low-energy beams has been designed, simulated, and tested with electron beams of several keV, in which space-charge effects play an important role. The resolution of the energy spread, as determined by simulation studies and experiments, was found to be less than 0.2 eV, which is significantly better than that of any comparable devices that we know about. This was made possible by separating the mesh electrically from the retarding/focusing cylinder and applying a controllable small voltage between the two. The associated electric field provides a stronger radial focusing of the beamlet (entering through a small aperture in the upstream plate). The speed and efficiency of the data collection process has been improved significantly with the aid of a computer-controlled system designed and built in-house.

Systematic and valuable experimental work has been performed to study the longitudinal energy spread growth with the high-resolution energy analyzer in the space-charge-dominated beam at two different locations (0.25 m and 2.3 m from the electron gun) and under different beam conditions.

Beam energy spread has been measured at the distance of 25 cm from the gridded electron gun. The measured beam energy spreads, are in remarkably good agreement with the intrinsic limits set by the effects of non-adiabatic acceleration in the electron gun and that of Coulomb collisions, as predicted by theory. The absolute mean energy is believed to have a DC offset from the real beam energy due to the field leakage at the retarding mesh. The offset is about 1% of the beam energy. However, the measurement of the relative beam energy and the energy spread has very high

resolution, better than 0.2 eV. By accurately measuring the beam energy change with the grid bias voltage, we are able to calculate the input impedance between the cathode and grid due to beam loading.

A long uniform focusing channel with a length of 2.3 m has been built to study the evolution of the beam energy spread over this distance. We studied the relation of the evolution of beam energy spread with beam current and beam density. At the lower beam current density, the evolution of the beam energy spread has no relation with the beam energy and the experimental results have very good agreement with the theoretical predictions. However, the measured beam energy spreads are always larger than the theoretical predictions for higher density beams, which maybe be caused by the instabilities. A simple scaling law of beam energy spread is derived and agrees with the calculation results and experimental results at the lower current density.

With proper scaling, the physics obtained here is applicable to other beams too, like high-energy ion beams. After the experiment on the linear channel, we plan to do the experiment on the University of Maryland Electron (UMER), which will let the beam travel over a much longer distance. We also would like to investigate if the apparently larger measured energy spread at high beam densities is due to collective effects or instabilities associated with the collective space-charge forces.

For the future work, another diagnostic chamber with energy analyzer and phosphor screen in it will be inserted in the linear channel. We already left room for the diagnostic chamber when we designed this linear channel. More experiments could be done to study the temporal energy spectrums and space-charge waves with

different modulations, such as density modulation or energy modulation, in this linear channel set-up. We can introduce density modulation in the beam using laser excited cathode emission. We also can add voltage modulation on the grid-cathode to generate energy and density modulations. Some preliminary simulation work on the energy analyzer trying to understand its operation, resolution, and transient responses has been done in the past two years using WARP. More studies are needed to understand the transient behavior of the energy analyzer.

In conclusion, a large number of experimental achievements on the longitudinal beam physics have been presented in this dissertation. However, more valuable and challenging work can be done in this area with facilities (including hardware and software) already developed in the linear channel and UMER.

References:

[1] M. Reiser, Theory and Design of Charged Particle Beams (John Wiley & Sons, Inc, New York, 1994).

[2] E. P. Lee, Nuovo Cimento, **106A** (1993).

[3] T. C. Marshall, Free Electron Lasers (Macmillan Pub. Co., New York, 1985).

[4] P.G. O'Shea, M. Reiser, R.A. Kishek, S. Bernal, H. Li, M. Pruessner, V. Yun, Y. Cui, W. Zhang, Y. Zou, T. Godlove, D. Kehne, P. Haldemann, and I. Haber, Nucl. Instr. and Meth. A 464, 2001, p. 646-652.

[5] D. Kehne, Ph.D. Dissertation, Dept. of Electrical Engineering, University of Maryland, College Park, 1992.

[6] D. X. Wang, Ph.D. Dissertation, Dept. of Electrical Engineering, University of Maryland, College Park, 1993.

[7] H. Suk, Ph.D. Dissertation, Dept. of Electrical Engineering, University of Maryland, College Park, 1996.

[8] Y. Zou, Ph.D. Dissertation, Dept. of Electrical Engineering, University of Maryland, College Park, 2000.

[9] S. Ichimaru and M. N. Rosenbluth, Phys. Fluids **13**, 2778 (1970).

[10] T.M. O'Neil and P.G. Hjorth, Phys. Fluids **28**, 3241(1985).

[11] I. Haber, A. Friedman, D.P. Grote, and S.M. Lund, Phys. of Plasma **6**, 1999, p. 2254.

[12] H. Boersch, Z. Phys. **139**, 115 (1954).

[13] A. W. Hyatt, C. F. Driscoll, and J. H. Malmberg, Phys. Rev. Lett. **59**, 2975 (1987).

[14] B.R. Beck, J. Fajans, and J.H. Malmberg, Phys. Rev. Lett. **68**, 1992, p. 317.

[15] A.V. Aleksandrov, N.S. Dikansky, N.Cl. Kot, V.I. Kudelainen, V.A. Lebedev, P.V. Logachov, R. Calabrese, V. Guidi, G. Ciullo, G. Lamanna and L. Tecchio, Phys. Rev. A **46**, 6628 (1992).

[16] Y. Zou, Y. Cui, V. Yun, A. Valfells, R.A. Kishek, S. Bernal, I. Haber, M. Reiser, P.G. O'Shea, and J.G. Wang, Phys. Rev. ST Accel. Beams **5**, 072801 (2002).

[17] J.A. Simpson, Rev. Sci. Instrum. **32**, 1283 (1961).

[18] R.A. Pitts, R. Chavan, S.J. Davies, S.K. Erents, G. Kaveney, G.F. Matthews, G. Neill, J.E. Vince, JET-EFDA workprogramme contributors and I. Duran, Rev. Sci. Instrum. **74**, 4644 (2003).

[19] R.J. Macek, A. Browman, M. Borden, D. Fitzgerald, T.S. Wang, T. Zaugg, K. Harkay, R. Rosenberg, in Proceedings of the 2003 Particle Accelerator Conference, Portland, OR, 2003 (IEEE, New York, 2003), pp. 508-510.

[20] R.A. Rosenberg and K.C.Harkay, *Nucl. Instrum. Meth. A*, **453**, 507 (Oct. 2000).

[21] H.Ch. Paulini and U. Littmark, *Nucl. Instrum. Meth. B* **58**, 260-265 (1991).

[22] Arthur W. Molvik, Rev. Sci. Instrum. **52**, 704 (1981).

[23] S. Falabella and A. W. Molvik, Rev. Sci. Instrum. **61**, 1892 (1990).

[24] Y. SAKAI, M. KATO, S. MASUDA, Y. HARADA and T. ICHINOKAWA, Surface Review and Letters, **5**, 1199-1211(1998).

[25] N. Bundaleski , *Nucl. Instrum. Meth. B* **198**, 208-219 (2002).

[26] David A. Dahl, SIMION 3D Version 6.0 User's Manual, Idaho national engineering laboratory, et al., 1995.

[27] Software for Modeling Electron and Ion Sources, Munro's Electron Beam Software Ltd, 1996.

[28] J. G. Wang, E. Boggasch, P. Haldemann, D. Kehne, M. Reiser, T. Shea, and D. X. Wang, IEEE Transactions on Electron Devices. **37**, 2622 (1990).

[29] S. Bernal, Private communication, 2000.

[30] Y. Cui, M.S. Thesis, Dept. of Electrical Engineering, University of Maryland, College Park, 2001.

[31] Y. Zou, Y. Cui, I. Haber, M. Reiser and P.G. O'Shea, Phys. Rev. ST Accel. Beams **6**, 112801 (2003).

[32] A. Faltens, E.P. Lee, and S.S. Rosenblum, J. Appl. Phys. **61**, 5219 (1987).

[33] J.G. Wang, H. Suk, D.X. Wang and M. Reiser, Phys. Rev. Lett. **72**, 2029 (1994).

[34] J. Harris, A. Valfells, B. Beaudoin, S. Bernal, A. Diep, I. Haber, Y. Huo, B. Quinn, M.Reiser, M. Walter, P.G. O'Shea, in Proceedings of the 2003 Particle Accelerator Conference, Portland, OR, 2003 (IEEE, New York, 2003), pp. 2312-2314.

[35] R. Kishek, New empirical formula for IPR solenoids, code: E-RING-97-53.

[36] D.P. Grote, A. Friedman, I. Haber, S. Yu, "Three-dimensional simulations of high current beams in induction accelerators with WARP3D", Fus. Eng. & Des. 32-33, 193-200 (1996).

[37] C.K. Allen, S. K. Guharay, M. Reiser, "Optimal Transport of Low Energy Particle Beams", Proc. 1995 IEEE PAC, p. 2324 (1996).

[38] M. Reiser et al. "The Maryland Electron Ring for Investigating Space-Charge Dominated Beams in a Circular FODO System", Proc. IEEE 1999 PAC, New York, p. 234 (1999).